SERA
Seismology and Earthquake Engineering
Research Infrastructure Alliance for Europe

DELIVERABLE

D27.1 Enhanced HDS due to order reduction, reduced epistemic uncertainties and complementary use of offline dynamic substructuring methods

Work package	WP27/JRA5 - Innovative testing methodologies for component/system resilience
Lead	UNITN
Authors	Oreste S. Bursi, UNITN Patrick Covi, UNITN Francisco J. Molina, JRC Rocco Di Filippo, UNITN António A. Correia, LNEC Alexandra Carvalho, LNEC
Reviewers	ETHZ
Approval	Management Board
Status	Final
Dissemination level	Public
Delivery deadline	16.01.2019
Submission date	08.01.2019
Intranet path	DOCUMENTS/DELIVERABLES/SERA_D27.1_Enhanced_HDS

This project has received funding from the European Union's Horizon 2020 research and innovation programme under grant agreement No 730900.

Table of Contents

Summary

Along with the drive to follow and exploit the developments both in the area of numerical modelling of non-linear systems and the area of advanced testing of components/systems using hybrid (numerical/physical) dynamic substructuring simulations, the content of Deliverable D27.1 pursues the following objectives:

- ✓ Develop control system strategies aiming at a high accuracy of hydraulic actuators when they face relatively high testing speed, stiff modes and a large number of degrees of freedom (DoFs).
- ✓ Compare the performance of online, i.e. the hybrid dynamic simulation (HDS) method, and offline methods like the impulse-based substructuring (IBS) and the Lagrange multiplier frequency-based substructuring (LM-FBS). Also a combined method that relies on the previous methods and adopts the localized version of the method of Lagrange multipliers is developed.
- ✓ Develop a framework for a thermomechanical coupled analysis for HDS. It is shown that to obtain compatibility and equilibrium at the interface DoFs, the partitioned algorithm LLM-GC based on the FETI algorithm class is suitable to couple a PS with a NS. Moreover, the partition of the domains is conceived with the idea to be actually replicated in the laboratory by retaining the most significant DoFs at the interface between NS and PS.
- ✓ Reduce epistemic uncertainties in HDS. In this respect, a stochastic ground motion model is calibrated according the seismic hazard of a specific site. Relevant model's parameters are evaluated and reduced by means of a global sensitivity analysis (GSA) upon the seismic response of realistic tank-piping system. With the entailing seismic input, some hybrid simulations are carried out and a relevant FEM was tuned with a good level of accuracy.
- ✓ Study the propagation of uncertainty and the sensitivity of a stochastic finite-fault model for ground motion generation, considering the earthquake source spectrum, path effects and site conditions.

1 Mixed control techniques for accuracy improvements

1.1 Improvement of testing accuracy by introduction of mixed control

The accumulated experience over more than twenty years of performed experiments at the European Laboratory for Structural Assessment (ELSA) of JRC and the developed control system currently used allow for applying reliable control strategies for a wide range of structural testing setups by using hydraulic actuators. However, difficulties may still typically arise when testing structures at relatively high testing speed, with stiff modes, with a large number of DoFs, with a very high requested accuracy or a combination of several of these conditions.

Within the SERIES project and with the collaboration of ELSA, a number of advanced techniques for the improvement of the control hardware and algorithms were studied. SERIES Deliverables D12.2 (2012) and Deliverable D12.3 (2013), and particularly Bosi et al. (2012), describe that research. Interesting models were used there to show the potential advantage of the introduction of velocity feedforward, acceleration, force or pressure-difference direct feedback and full-state oriented control by using displacement, velocity and acceleration feedback within the control loop and for the hybrid testing method.

For the case of testing setups that include stiff modes and present difficulties with the traditional displacement control approach, Bousias (2014) reviews several available control strategies. This problem has also appeared in ELSA for some of the setups and ingenious solutions have been created ‘ad hoc’ in order to get a control of acceptable quality. However, some of those solutions and many more can now be covered within a general approach that is called mixed control modes. Each mixed control mode is controlled with its feedback defined either in displacement or force and produces a control command that requires a coordinate transformation before being sent to the actuator servo-valves of all the actuators.

Testing setups for research and for the industry are designed with specifications in displacement, forces and other magnitudes as well as possible constraints. The obtained solutions use several actuators that are required in a number equal to or larger than the total specified DoFs. Regarding the specimen, such setups can be always interpreted as a coupled Multiple-Input Multiple-Output (MIMO) system. However, in most of the cases, the control of every actuator is still a Single-Input Single-Output (SISO) loop, without combining feedback sensors from several DoFs to produce the servo-valve command. Alternatively, in the industry, there are examples of use of really coupled MIMO controllers, as it is the case of some multi-directional shaking tables, with different specific formulations, that often are heuristically derived, and work reasonably well but are difficult to export to other setups as a general approach.

According to our knowledge, a consistently formulated MIMO general approach for structural testing setups is proposed by Plummer et al. (2010, 2013). They propose a number of steps for the formulation of the rigid-body (and of the deformable) control modes, the definition of their control loops in displacement (and in force respectively) and the transformation of their control commands for the servo-valves of the hydraulic actuators. We have realised that some of the particular strategies that we had applied as coupled MIMO controller formulation for specific setups with redundant actuators, can be rationalised by applying the guided procedure proposed by Plummer and leading to partially

equivalent formulations (see Molina et al, 2016). Plummer's methodology is indicated for systems with the following characteristics:

- The range of motion is limited so that the geometric relationships remain constant and linear.
- The number of actuators is larger than the number of rigid-body displacement DoFs.
- The actuators are servo-hydraulic or electric.
- The displacements and forces are measured at the actuator coordinates.

Redundant actuators are added in some setups in order to have improved or safer performance by having a controlled distribution of the internal forces.

An expected advantage of a full implementation of Plummer's approach, or the use of control modes that are not coincident with the actuator coordinates in general, is the possibility to have completely independent control algorithm (PID or others) for the different control modes. For example, in our previous formulations, we used different P parameter for displacement or force controlled modes, but the available software did not allow for having different I parameter for each mode. In the following subsections, we will present the case of one of the SLA4F4E setups at ELSA in which the applied strategy has been rationalised by following Plummer's approach.

1.1.1 SLA4F4E two-actuator shear setup: Applied formulae as heuristically derived

Fusion for Energy (F4E) is the European Union's Joint Undertaking for ITER. The ITER nuclear fusion facility is being constructed in southern France. Within the SLA4F4E project at ELSA, in collaboration with F4E, some models of embedded plates for the ITER Tokamak building have been tested in order to assess their loading capacity under different conditions. The specimen for these tests consists of a steel plate with welded studs that are embedded in a concrete block. Setups for pure normal loading on the plate as well as for pure shear loading and some combined actions have been used. The most challenging setup from the control point of view was the one for shear load using two aligned actuators.

The shear setup for the SLA4F4E with two aligned actuators applied the force on the specimen embedded plate by means of a connecting beam between the actuators and rigidly bolted to the plate (Figure A.1 and Figure A.2). Previous shear tests had been performed by pulling in only one direction with one actuator working always in tension. This new setup was designed to allow for pulling in both directions in alternated manner. For this reason, we decided to use two actuators instead of one in order to have a better control of the transversal stability by means of introducing a pre-stablished pre-tension in the loading beam and avoid or reduce the compression force in any actuator.

Having two actuators in this setup, two controlled DoFs or modes were necessary to be defined. In order to avoid uncontrolled force in the loading beam, we decided to use one DoF as displacement mode and another one as force mode. The displacement mode was chosen as the mean displacement between both actuators, i.e. equivalently, the 'rigid-body' displacement of the beam

$$\boldsymbol{y_c = Py} \tag{A.1}$$

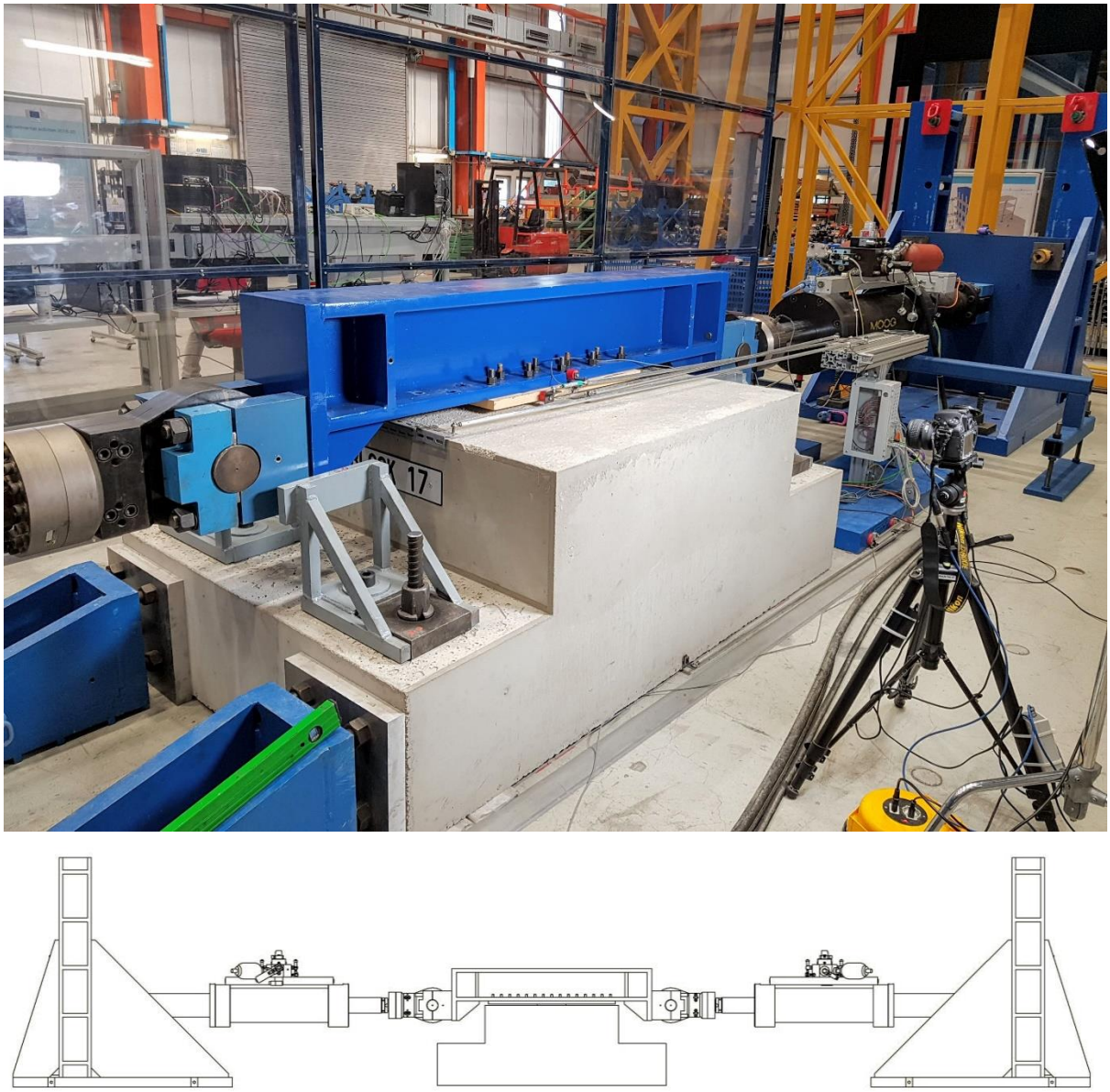

Figure A.1 – SLA4F4E two-actuator shear setup. Photograph and drawing.

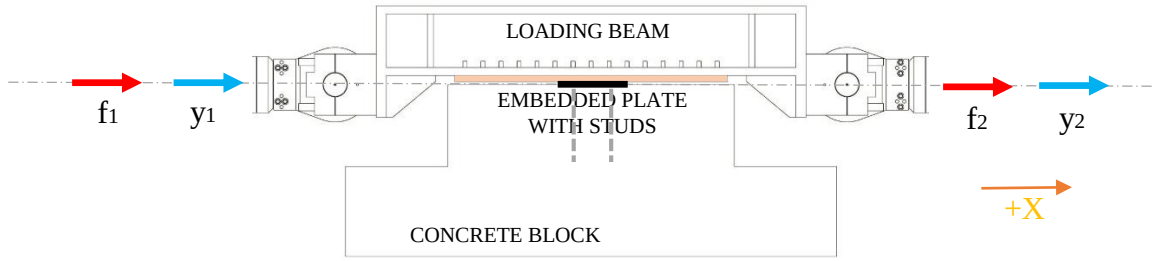

Figure A.2 – Actuator displacements and forces at SLA4F4E two-actuator shear setup.

was defined as

$$[y_c] = [1/2 \quad 1/2] \begin{bmatrix} y_1 \\ y_2 \end{bmatrix} \tag{A.2}$$

where y_1 and y_2 were the internal displacements at both actuators. The remaining DoF was defined in force as the average tension stress (between the two halves) in the loading beam or, equivalently, the 'deformable' coordinate

$$\boldsymbol{f_d = Qf} \tag{A.3}$$

More precisely,

$$[f_d] = [-1/2 \quad 1/2]\begin{bmatrix} f_1 \\ f_2 \end{bmatrix} \tag{A.4}$$

Note that, if the resultant force on the plate is

$$f_s = f_1 + f_2 \tag{A.5}$$

By combining, equations (A.4) and (A.5), the force given by each actuator is

$$f_1 = \frac{f_s}{2} - f_d; \qquad f_2 = \frac{f_s}{2} + f_d \tag{A.6}$$

The idea was to have the possibility to control f_d to be a constant positive value f^0 larger than one half of the maximum expected force to apply on the plate

$$f^0 > \max(\left|\frac{f_s}{2}\right|) \tag{A.7}$$

in order to guarantee out-of-plane stability by avoiding compression on any side of the beam.

The mixed feedback was directly formulated in the actuator coordinates by transforming and combining the rigid-body mode and the flexible mode in the form

$$\boldsymbol{y^{MIX} = C\, y_c + w\, D\, f_d} \tag{A.8}$$

More precisely,

$$\begin{bmatrix} y_1^{MIX} \\ y_2^{MIX} \end{bmatrix} = \begin{bmatrix} 1 \\ 1 \end{bmatrix}[y_c] + w\begin{bmatrix} -1/2 \\ 1/2 \end{bmatrix}[f_d] \tag{A.9}$$

In the case of using a pure proportional control algorithm equal for the two actuators, the control command would have been

$$\boldsymbol{u = p\left(y^R - y^{MIX}\right) = p\left[C\left(y_c^R - y_c\right) + w\, D\, \left(f_d^R - f_d\right)\right]} \tag{A.10}$$

where, by definition, the reference displacements are

$$\boldsymbol{y^R = C y_c^R + w\, D\, f_d^R} \tag{A.11}$$

And, by trial and error, a value was given to the scalar w

$$w = 0.004\ \text{mm/kN} \tag{A.12}$$

Note that in the mixed reference $\boldsymbol{y^R}$, defined by expression (A.11), the reference displacement at the centre y_c^R was a value that was iterated by increments in order to optimise the measured displacement or force on the embedded plate in comparison with prescribed values. On the other hand, in order to improve the stability of the actuators and connecting beam, the constant value (A.7) was used as reference $f_d^R = f^0$ for the force mode.

1.1.2 SLA4F4E two-actuator shear setup: assimilation to Plummer's approach

Plummer (2010, 2013) has developed a general approach for dealing with this kind of control setups in which the actuators coordinates are substituted by a set of rigid-body modes plus a set of deformable modes. The idea is to use coordinate transformation for displacement and forces so that effectively the

control loops are closed on the specimen rigid modes (in displacement control) and deformable modes (in force control). See Figure A.3 as extracted from the reference.

In the general case, Plummer (2010, 2013) basically decomposes the actuator displacements $\boldsymbol{y}$ in specimen coordinates (rigid modes $\boldsymbol{y_c}$ and deformable modes $\boldsymbol{y_d}$)

$$\boldsymbol{y = C\, y_c + D\, y_d} \tag{A.13}$$

and defines

$$\boldsymbol{y_c = Py} \tag{A.14}$$

for the rigid modes with displacement feedback and

$$\boldsymbol{f_d = Qf} \tag{A.15}$$

for the deformable modes with force feedback.

Then, he proposes a process for determining the introduced transformation matrices ($\boldsymbol{C, D, P, Q}$) for the particular case that can be summarised as follows.

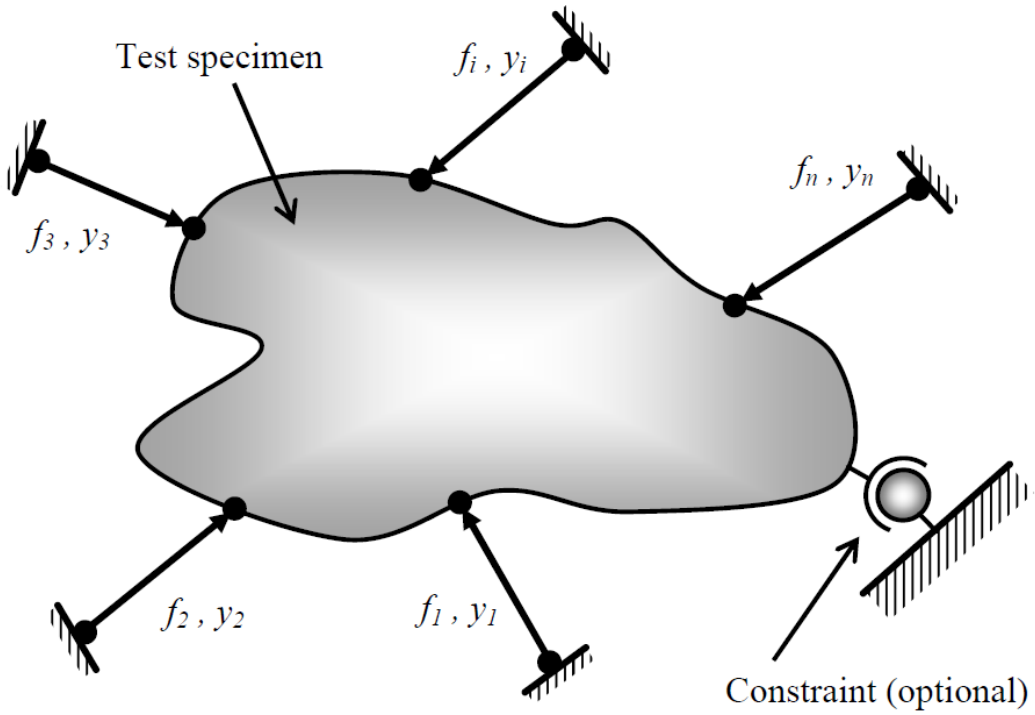

Figure A.3 – A generic test system.

Source: Plummer (2010).

- First, depending on the requirements of your application, select $\boldsymbol{C}$ so that, in the case of "null deformations", the actuator displacements are derived from a minimum set of rigid body coordinates

$$\boldsymbol{y]_{f_d=0} = C\, y_c} \tag{A.16}$$

For our SLA4F4E case, for null average tension in the loading beam, this would have been

$$\begin{matrix} y_1 \\ y_2 \end{matrix}\Big]_{\boldsymbol{f_d=0}} = \begin{bmatrix} 1 \\ 1 \end{bmatrix} [y_c] \tag{A.17}$$

where y_c is the average displacement of the beam as a rigid body. Note that here we are talking about "null (average) deformation" in the loading beam, but not in the concrete block with the embedded plate.

- Second, in order to have

$$\boldsymbol{PC} = \boldsymbol{I} \tag{A.18}$$

and

$$\boldsymbol{PD} = \boldsymbol{0} \tag{A.19}$$

and then, following (A.14), to define

$$\boldsymbol{y_c} = \boldsymbol{Py} = \boldsymbol{PC}\,\boldsymbol{y_c} + \boldsymbol{PD}\,\boldsymbol{y_d} \tag{A.20}$$

compute $\boldsymbol{P}$ as the pseudoinverse of $\boldsymbol{C}$

$$\boldsymbol{P} = \left(\boldsymbol{C^T C}\right)^{-1}\boldsymbol{C^T} \tag{A.21}$$

and determine $\boldsymbol{D}$ as a basis for the null space of $\boldsymbol{P}$.

For our SLA4F4E case, $\boldsymbol{P}$ would have been

$$\boldsymbol{P} = \left(\boldsymbol{C^T C}\right)^{-1}\boldsymbol{C^T} = ([2])^{-1}[1 \quad 1] = [1/2 \quad 1/2] \tag{A.22}$$

as we already had (see expression (A.2)).

For $\boldsymbol{D}$, Plummer, more precisely, proposes to use a "rational" basis obtained from the reduced row echelon form of $\boldsymbol{P}$, as it is given, for example, by the MATLAB [29] function $\boldsymbol{null}(\boldsymbol{P}, \boldsymbol{'r'})$, i.e.,

$$\text{MATLAB: } \boldsymbol{null}(\boldsymbol{P}, \boldsymbol{'r'}) = \begin{bmatrix} -1 \\ 1 \end{bmatrix} \tag{A.23}$$

Note that, in general, multiplying $\boldsymbol{D}$ by a scalar might be desirable so that the transformed forces are physically meaningful. Again, for our SLA4F4E case, this is equivalent to what we used in (A.9)

$$\boldsymbol{D} = \begin{bmatrix} -1/2 \\ 1/2 \end{bmatrix} \tag{A.24}$$

- Third, in order to define, following (A.15),

$$\boldsymbol{f_d} = \boldsymbol{Qf} \tag{A.25}$$

determine $\boldsymbol{Q}$ as

$$\boldsymbol{Q} = \boldsymbol{D^T} = [-1/2 \quad 1/2] \tag{A.26}$$

which coincides with what we used in (A.4).

- Fourth, by deriving (A.13),define your control signal in terms of velocity commands as

$$\boldsymbol{u} = \boldsymbol{C}\,\boldsymbol{u_c} + \boldsymbol{D}\,\boldsymbol{u_d} \tag{A.27}$$

See Figure A.4.

Now, in the particular case of using a pure proportional control algorithm for the rigid-body modes in displacement control

$$\boldsymbol{\varepsilon_c = y_c^R - y_c} \quad ; \quad \boldsymbol{u_c = p_c \varepsilon_c = p_c\left(y_c^R - y_c\right)} \tag{A.28}$$

and for the deformable modes in force control

$$\boldsymbol{\varepsilon_d = f_d^R - f_d} \quad ; \quad \boldsymbol{u_d = p_d \varepsilon_d = p_d\left(f_d^R - f_d\right)} \tag{A.29}$$

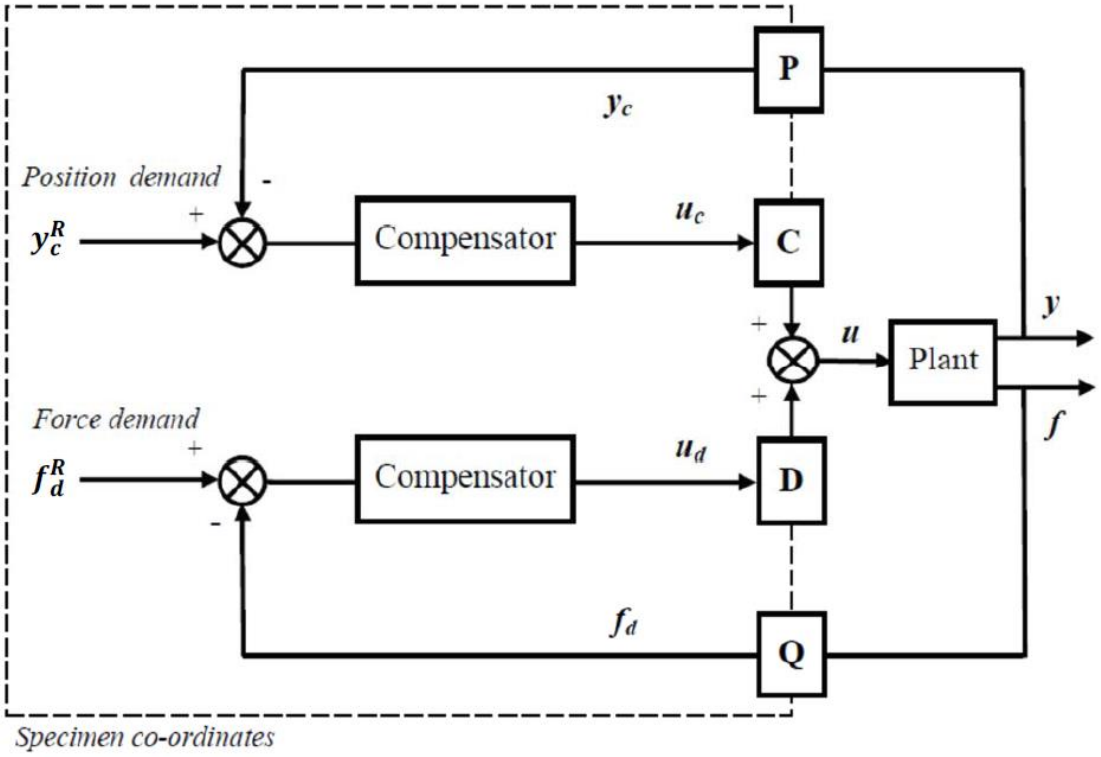

Figure A.4 – Multi-axis control with co-ordinate transformations.

Source: Plummer (2010).

and being in this case $\boldsymbol{p_c}$ and $\boldsymbol{p_d}$ scalars, we could have

$$\boldsymbol{u = C\, u_c + D\, u_d} = p_c \left[\boldsymbol{C}\left(\boldsymbol{y_c^R - y_c}\right) + \frac{p_d}{p_c}\,\boldsymbol{D}\,\left(\boldsymbol{f_d^R - f_d}\right)\right] \tag{A.30}$$

which is equivalent to what we applied as described in the previous section (see expression (A.10))

$$\boldsymbol{u} = p\left[\boldsymbol{C}\left(\boldsymbol{y_c^R - y_c}\right) + w\,\boldsymbol{D}\,\left(\boldsymbol{f_d^R - f_d}\right)\right] \tag{A.31}$$

1.1.3 SLA4F4E two-actuator shear setup: graphic results

As an example, this section includes some graphic results for one low-cycle fatigue test performed on SLA4F4E Block25 using the described two-actuator shear setup and control strategy. Basically the test consisted of introducing 5050 cycles of shear load on the embedded plate specimen with several constraints to be respected for every cycle regarding the minimum and the maximum values of force, displacement or a linear combination of both. Since we are now interested only on the performance of the control, the results will be shown just for 4 typical cycles for which the dominant constraint was a specimen displacement y_s equal to zero

$$[y_s]_{min} = 0 \tag{A.32}$$

for the minimum and a combination of specimen force and displacement equal to 317 kN

$$[f_s + 176\, y_s]_{max} = 317\ kN \tag{A.33}$$

for the maximum, where f_s is expressed in kN and y_s in mm. Figure A.5 shows the specimen force (A.5) (resultant from both actuators) and the specimen displacement y_s (mean of two transducers positioned at the central line of the embedded plate, front and back of the loading beam). Both resultant force and mean displacement for the specimen are oriented in the +X direction (see Figure A.2). At the moment of performing these four cycles, some damage had already been introduced into the specimen by the previous 450 cycles. The shape of the four cycles is repetitive with very small damage accumulation –not visible in the figure.

In Figure A.6, the time histories for the same variables are plotted for the four cycles. Note that the time variable used as abscissa corresponds to one second (prototype time) per cycle but in reality the adopted period of the cycles was two seconds (real time).

Regarding the mixed-mode control defined by the control loop (A.30), Figure A.7 shows, for the same four cycles, in the upper graph, the reference y_c^R and the feedback y_c variables for the rigid-body mode, which is controlled in displacement. This upper graph includes also a third curve which is the specimen displacement y_s. Note that the rigid-body mode feedback displacement (A.2) was computed from the actuator internal displacements (easier to control), whereas the specimen displacement was measured by other transducers directly fixed on the embedded plate as it has been mentioned. The difference between one displacement and the other is due to the flexibility in the actuators, their attachments and the connecting beam as well as the reaction system. The same figure also shows, in the lower graph, the reference f_d^R and the feedback f_d variables for the flexible mode, which is controlled in force. The flexible mode force was defined as the mean tension in the loading beam, as shown in expression (A.4), and, for its reference (A.7), a constant value

$$f_d^R = f^0 = 150\ kN \tag{A.34}$$

had been adopted. Since the frequency (0.5 Hz) of the applied cycles is relatively high for a quasistatic test, the control errors are significant for both modes, but the stability and robustness of the control were the priority in this case. Note that the prescribed constraints where used for the modulation of the reference displacement y_c^R only through an iterative algorithm. Said algorithm corrects the oscillation extremes of the reference for the next cycle by using as input the relevant measured extremes of the displacements, forces and their combinations at the previous cycle. The result was highly accurate at the constraints, such as (A.32) and (A.33), except for the first cycles at the beginning of the test and after any sudden change in the constraints or in the behaviour.

Finally, for completeness, the time histories of the actuator internal displacements and load cell forces are plotted in Figure A.8. Note that, for these transducers associated to each actuator, the sign criterion in ELSA is such that the force is positive when the actuator is pulling (tension) from its attachments and the displacement is positive when the attachments get closer to each other (shrinkage). This means that, with respect to the sign definitions in Figure A.2, the plotted variables in Figure A.8 are orderly $-y_1$, y_2, $-f_1$, and f_2. This figure confirms that, as it was desired, there was no significant spurious oscillation between the actuators (uncontrolled deformable mode of the loading beam) and the tension as each side of the loading beam was kept always positive.

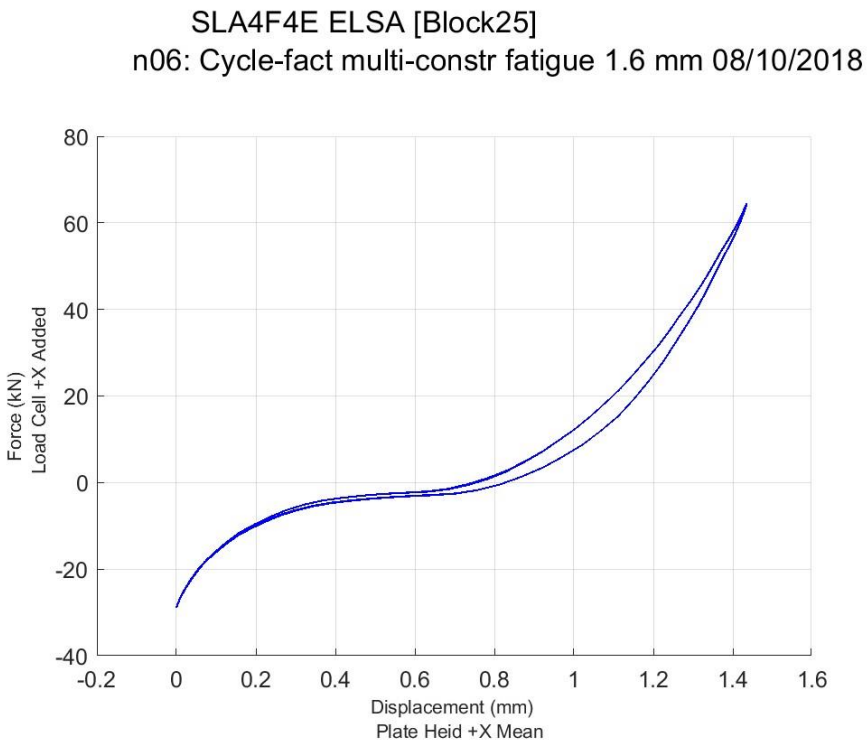

Figure A.5 – Total shear load versus mean horizontal displacement on specimen embedded plate (4 cycles).

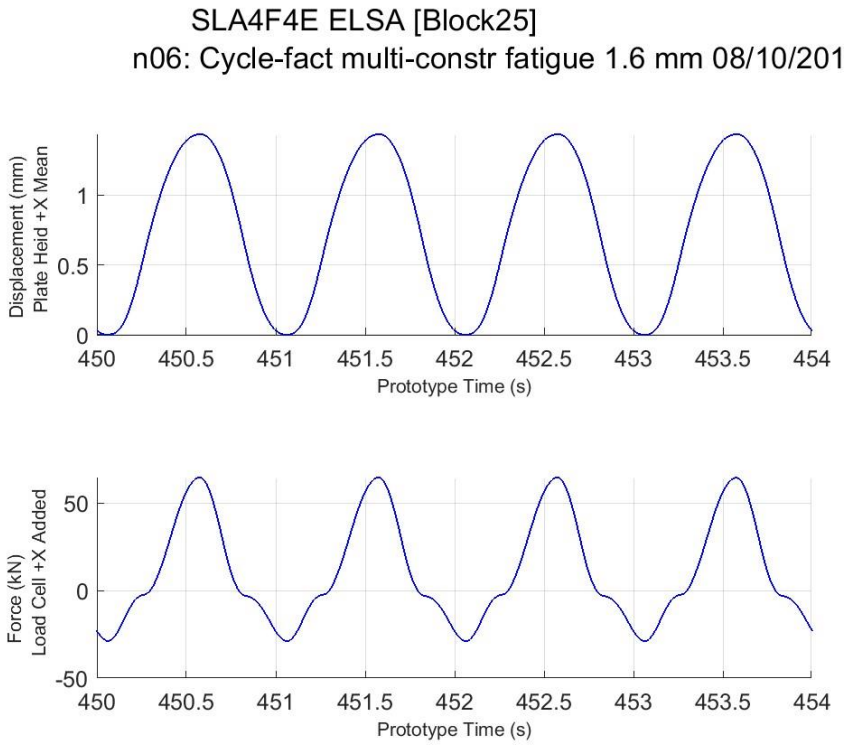

Figure A.6 – Time histories of mean horizontal displacement and total shear load on specimen embedded plate (4 cycles).

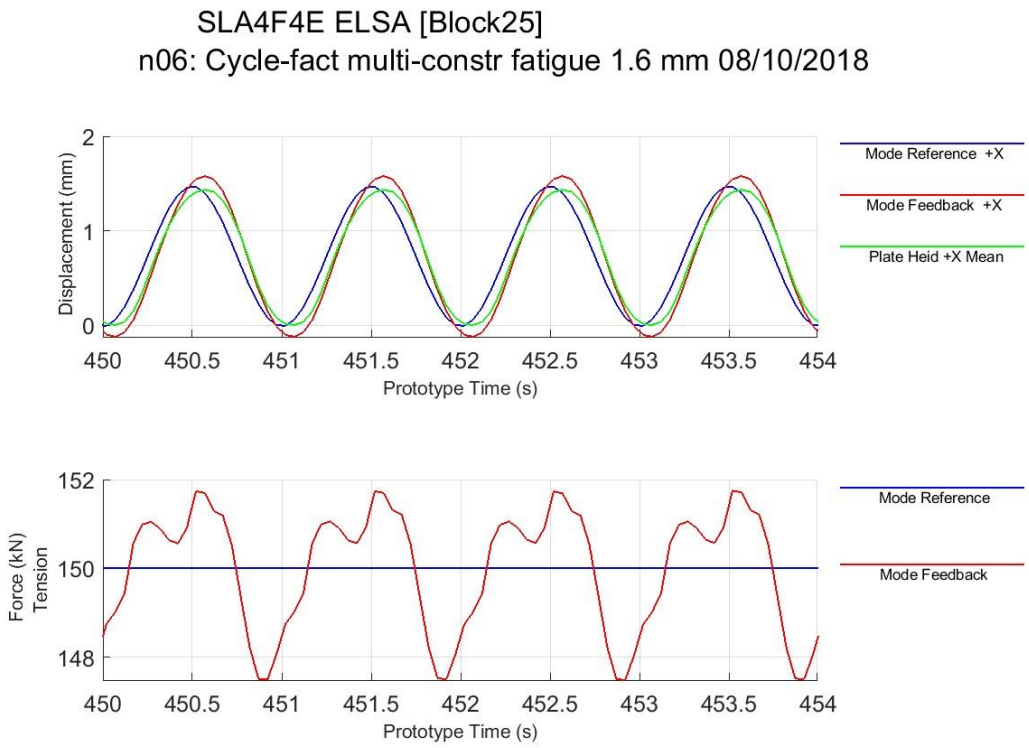

Figure A.7 – Reference and feedback signals for displacement mode (upper graph) and force mode (lower graph).

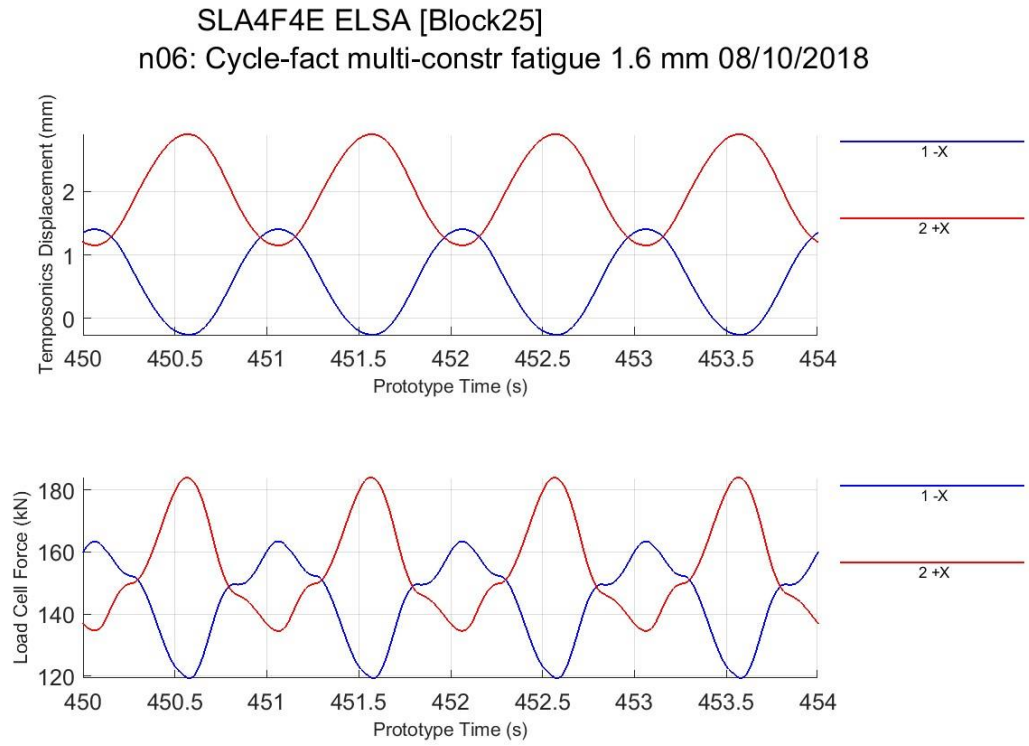

Figure A.8 – Actuator internal displacements (upper graph) and actuator load cell forces (lower graph).

2 Enhanced adoption of online offline dynamic substructuring methods

2.1 Complementary use of online offline dynamic substructuring methods

Numerical/physical online hybrid dynamic substructuring simulations have shown their potential to allow realistic dynamic analysis of almost any type of non-linear structural system.

Successful online hybrid (numerical/physical) dynamic substructuring simulations have shown their potential in enabling realistic dynamic analysis of almost any type of non-linear structural system (e.g., an as-built/isolated viaduct, a petrochemical piping system subjected to non-stationary seismic loading, etc.). Moreover, owing to faster and more accurate testing equipment, a number of different offline experimental substructuring methods, operating both in time (e.g. the impulse-based substructuring) and frequency domains (i.e. the Lagrange multiplier frequency-based substructuring), have been employed in mechanical engineering to examine dynamic substructure coupling.

When part of the emulated system lacks a predictive computational model, measuring (instead of modelling) its response represents a convenient approach for deriving low-discrepancy simulators with reduced cost and effort. In this regard, the EDS paradigm provides the response history of a so-called emulated system that includes PSs and NSs

The class of EDS methods is divided into online and offline algorithms, depending on the strategy adopted for the calculation of the emulated system response. In the online case, primal/dual boundary conditions imposed to the PS, e.g. displacements/forces, are updated at each step of the simulation and corresponding dual/primal boundary conditions, e.g. force/displacement, enter into a time integration algorithm, which solves the system of equilibrium equations and advances to the next step. Real-time computing synchronized with precise servo-controlled actuators is crucial for the implementation of the simulation loop. Conversely, offline EDS algorithms require all experimental data to be measured prior to the calculation of the emulated system response. In this case, less expensive and dangerous operational and experimental modal analysis tools such as accelerometers, impulse hammers and shakers are used to characterize the PS response.

2.1.1 The localized version of the method of Lagrange multipliers

In a primal formulation, a unique set of interface DoFs is retained. Classically, FE models are assembled in this primal manner [9]. Conversely, in a dual assembly formulation, all subdomains' DoFs are retained, all interface DoFs are present as many times as there are subdomains connected to the same DoF; an additional set of Lagrange multipliers enforces compatibility [16]. Although it may sound inconvenient to treat subdomains as separated in a pure numerical context at the price of adding further system unknowns (Lagrange multipliers), this is not the case in EDS. In fact, only the dual approach allows for tailoring algorithms and implementations to specific requirements on single (physical or numerical) subdomains, which guarantee both stability and accuracy.

From this perspective, the localized version of the method of Lagrange multipliers (LLM), can provide a dual assembly framework for connecting multiple NSs and PSs within the C-EDS method. It is well known that the classical method of Lagrange multipliers (CLM) allows for multiple sets of interface

compatibility equations for the modeling of interfaces connecting more than two subdomains by the same DoF. Nonetheless, to avoid singularity in modeling an arbitrary number of multi-point constraints, Park et al. [17] proposed a localized version of the CLM method.

In order to elucidate the use of the LLMs as method for dual assembly within the C-EDS framework, let us consider the following system of differential algebraic equations (DAE), in which m mechanical subdomain are coupled by LLMs,

$$\begin{cases} \mathbf{M}^{(l)}\ddot{\mathbf{u}}^{(l)} + \mathbf{R}^{(l)}\left(\mathbf{u}^{(l)}, \dot{\mathbf{u}}^{(l)}\right) = \mathbf{L}^{(l)^T}\boldsymbol{\Lambda}^{(l)} + \mathbf{F}^{(l)}(t) \\ \mathbf{L}^{(l)}\mathbf{u}^{(l)} + \bar{\mathbf{L}}^{(l)}\mathbf{u}_g = \mathbf{0} \; or \; \mathbf{L}^{(l)}\dot{\mathbf{u}}^{(l)} + \bar{\mathbf{L}}^{(l)}\dot{\mathbf{u}}_g = \mathbf{0} \end{cases} \quad \forall\, l \in \{1, \dots, m\} \tag{B.1a}$$

$$\sum_{l=1}^{m} \bar{\mathbf{L}}^{(l)^T}\boldsymbol{\Lambda}^{(l)} = \mathbf{0} \tag{B.1b}$$

where, $\mathbf{M}^{(l)}$ and $\mathbf{R}^{(l)}$ are the mass matrix and the restoring force vector of the l-th subdomain, respectively, whilst $\ddot{\mathbf{u}}^{(l)}, \dot{\mathbf{u}}^{(l)}$ and $\mathbf{u}^{(l)}$denote acceleration, velocity and displacement vectors. For a linear system, $\mathbf{R}^{(l)}$ reads,

$$\mathbf{R}^{(l)}\left(\mathbf{u}^{(l)}, \dot{\mathbf{u}}^{(l)}\right) = \mathbf{K}^{(l)}\mathbf{u}^{(l)} + \mathbf{C}^{(l)}\dot{\mathbf{u}}^{(l)} \tag{B.2}$$

with $\mathbf{C}^{(l)}$ and $\mathbf{K}^{(l)}$ damping and stiffness matrices of domain l. Vector $\mathbf{F}^{(l)}(t)$ represents the external time-varying load that, for seismic response history analyses, is typically defined as

$$\mathbf{F}^{(l)}(t) = -\mathbf{M}^{(l)}\mathbf{T}^{(l)}a_g(t) \tag{B.3}$$

where $\mathbf{T}^{(l)}$ is a Boolean vector depending on the direction of the seismic acceleration $a_g(t)$. For the sake of brevity, time dependence is omitted and therefore the independent variable t is dropped in the following. $\mathbf{L}^{(l)}$ and $\bar{\mathbf{L}}^{(l)}$ are Boolean signed matrices that collocate interface DoFs on the single subdomain DoF vector $\mathbf{u}^{(l)}$ and the generalized interface DoF vector $\mathbf{u}_g$, respectively. The latter gathers all coupled systems' interface DoFs taken once. According to Eq. (B.1a), each Lagrange multiplier vector $\boldsymbol{\Lambda}^{(l)}$ enforces compatibility between the corresponding subdomain l-th and the generalized interface DoF vector $\mathbf{u}_g$. Finally, Eq. (B.1b) imposes self-balance among all m interface force fields represented by Lagrange multiplier vectors.

As a dual-assembly approach, the LLM introduces additional sets of Lagrange multipliers, which satisfy interface equilibrium a priori through Eq. (B.1b) and enforce kinematic compatibility a posteriori by means of Eq. (B.1a). More precisely, at each simulation step displacement and velocity solutions of (B.1) split into free and link components. The former are calculated discarding coupling conditions and used to compute the latter by means of a linearized Steklov-Poincaré operator.

To crystallize the idea, Fig. B.1 illustrates an example of three-substructure coupling achieved by using the LLMs.

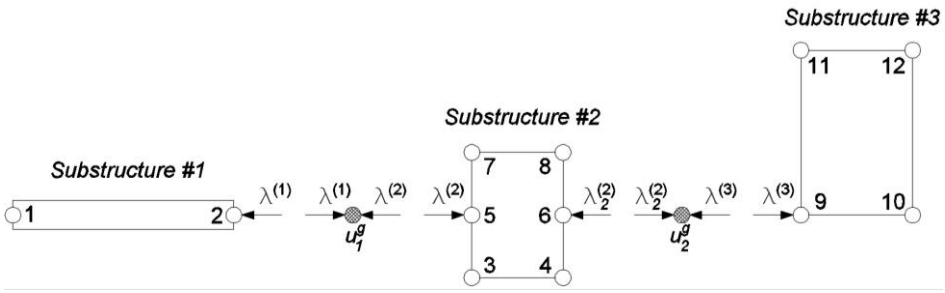

$$\mathbf{u}^{(1)^T} = \left[u_1^{(1)}, u_2^{(1)}\right]$$
$$\mathbf{u}^{(2)^T} = \left[u_3^{(2)}, u_4^{(2)}, u_5^{(2)}, u_6^{(2)}, u_7^{(2)}, u_8^{(2)}\right]$$
$$\mathbf{u}^{(3)^T} = \left[u_9^{(3)}, u_{10}^{(3)}, u_{11}^{(3)}, u_{12}^{(3)}\right]$$
$$\mathbf{u}_g^T = \left[u_1^g, u_2^g\right]$$
$$\mathbf{L}^{(1)} = [0,1], \bar{\mathbf{L}}^{(1)} = [-1,0]$$
$$\mathbf{L}^{(2)} = \begin{bmatrix}0,0,1,0,0,0\\0,0,0,1,0,0\end{bmatrix}, \bar{\mathbf{L}}^{(2)} = \begin{bmatrix}-1, & 0\\ 0, & -1\end{bmatrix}$$
$$\mathbf{L}^{(3)} = [1,0,0,0], \bar{\mathbf{L}}^{(3)} = [0,-1]$$

Fig. B.1. Three-substructure coupling based on the LLM.

We underline that Eq. (B.1a) permits both coupling on displacement and velocity. The latter approach is pursued when the coupled system response is calculated by using a time stepping algorithm. As proved by Gravouil and Combescure [16], this preserves stability of the coupled simulation as long as local stability conditions are satisfied for each subdomain taken independently.

As clearly explained by Park et al. [17], in the most general multi-point constraint case, that is, when $m > 2$ subdomains share all same interface DoFs, the CLM method leads to $m(m-1)/2$ linearly dependent systems of constraint equations, which cast kinematic compatibility among all possible pairs of subdomains. The task of retaining a subset of linearly independent constraint equations, which is not unique, has been a major issue in the CLM method. On the other side, the LLM method casts all constraint equations with respect to a single set of generalized interface DoFs $\mathbf{u}_g$, see Eq. (B.1), which leads to a unique set of m linearly independent systems of constraint equations for the same multi-point constraint case. As a result, for the same multi-point constraint case, Boolean coupling matrices $\boldsymbol{L}^{(l)}$ and $\bar{\boldsymbol{L}}^{(l)}$ are uniquely derived to form a set of m linearly independent systems of constraint equations, which guarantee non-singular Steklov-Poincaré coupling operators, as explained in the following sections. This feature extremely simplifies the implementations of EDS simulations with more than two subdomains and multi-point constraints with respect to state-of-the-art algorithms based on CLM [11].

The setting defined by Eq. (B.1) is valid for all EDS methods presented in the following subsections for the simplest case of two subdomains. Accordingly, to indicate PS and NS, respectively, superscript P and N replace (l).

2.1.2 The online hybrid dynamic substructuring method

As anticipated, online EDS methods compute the emulated system response while the PS is being tested. In the specific case of the HDS method, at each time step of a time integration loop, a set of servo-controlled actuators impose displacement to the PS and measure corresponding restoring forces. A computational driver solves the equation of motion of the coupled system and the simulation moves to the next time step. In the conventional HDS method, the actuator motion stops when the tested specimen reaches the target displacement and holds the position while the restoring force is measured. Conversely, actuators do not stop in the continuous HDS method so that the specimen follows very accurately the target displacement. In this case, the PS restoring force is measured at every controller sampling period Δt^C and the time integration loop shares the same rate of the controller. As a result, any stress-relaxation effect on the specimens is removed, even though the strain-rate effect may still be present if the real-time speed is not reached. However, Δt^C could be too small to accommodate the solution of the NS. In this context, partitioned time integration can play a crucial role: in fact, it allows for the synchronization of time integration of PS and NS, which can be performed with different time integration stepping methods and time steps.

With reference to the continuous HDS method, which is referred to as HDS method hereinafter, two partitioned time integration algorithms, namely the PM algorithm [11] and the GC algorithm [16] are presented in the following subsection.

Several HDS applications were successfully executed by using the partitioned PM integration method [8], which originates from the GC method [16]. The GC method was originally conceived to combine a pair of arbitrary Newmark schemes [18] with their own parameters and time steps, as schematically illustrated in Fig. B.2a. Since the GC is a staggered algorithm where task executions on both subdomains are consecutive or sequential, it does not allow for the continuous simulation of coupled numerical/physical sub-systems or, in other words, for a parallel solution of subdomains' responses. The PM method overcame the above limitation by modifying the task sequence of the GC method as shown in Fig. B.2b. In detail, a forward prediction of two coarse time steps on the numerical side enabled parallel implementations. However, this variant makes the PM method a non-self-starting procedure; therefore, the GC method initializes the simulation by solving the first coarse time step while the PM method is performing the first two-step forward prediction.

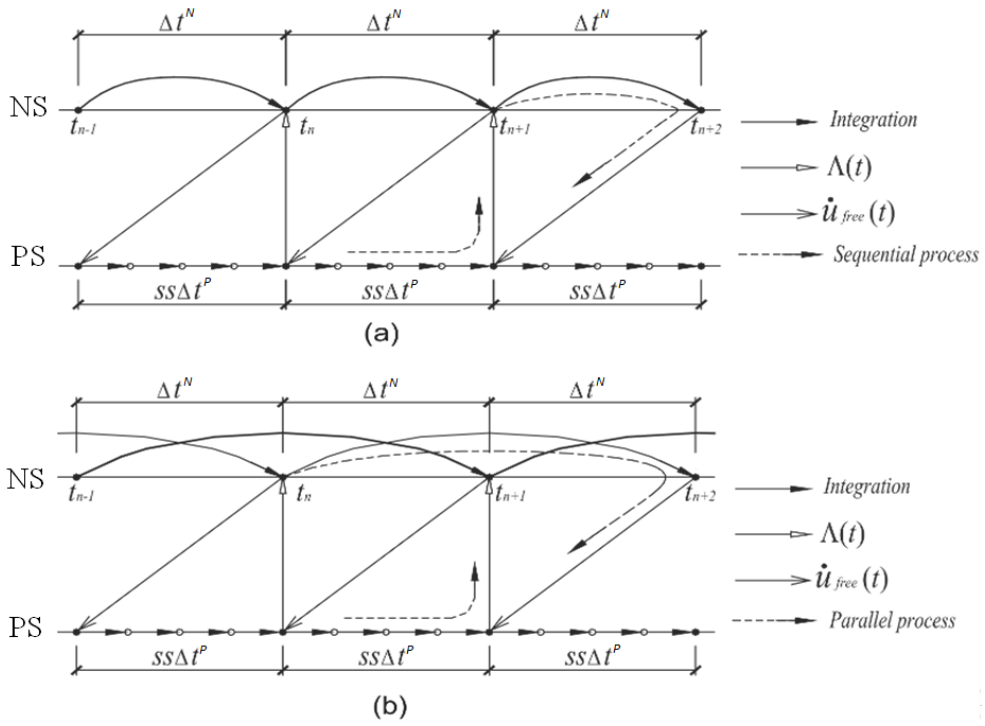

Fig. B.2. Task sequence of: (a) the staggered GC method; (b) the parallel PM method.

According to Figure 2, two parameters define the setting of the task sequence of both the GC and the PM algorithm,

- the testing time scale λ, defined as $\lambda = \Delta t^C / \Delta t^P$;
- the subcycling ss, obtained as $ss = \Delta t^N / \Delta t^P$.

where Δt^N defines the coarse time step, adopted for the NS, whilst Δt^P is the fine time step used to calculate the PS response. The optimal selection of these parameters is the result of a trade-off between numerical accuracy and experimental constraints. In particular, when $\lambda = 1$, one integration time step is performed on the PS in the same wall-clock time, which corresponds to the controller time step Δt^C and the test is conducted in real-time. Conversely, when $\lambda > 1$, the simulation time is

extended in comparison with the wall-clock time and the test is conducted in a pseudo–dynamic regime. When the response of the PS does not depend on the rate of loading, λ usually ranges between 50 and 200. Thus, a very small time step Δt^P can be achieved on the PS. This is beneficial for the stability of the explicit scheme. This approach improves the test quality by increasing the signal-to-noise ratio of response signals and reduces the control tracking error. Moreover, an extended simulation time scale λ reduces the destabilizing effect of electro-hydraulic actuator delays, which is typically of the order of $10 \div 20\, ms$ [19]. If λ is supposed to cope with the limitations of the actuation system performance, the subcycling parameter ss lets us adjust the allowable solving time $t^S = ss\, \Delta t^C$, which constrains the size and complexity of the NS.

For the sake of clarity, the PM method [11], enriched with the LLMs [17], is summarized in algorithmic form hereinafter for the case of two subdomains, i.e. a PS and a NS. The central difference explicit scheme ($\gamma^P = 1/2$ and $\beta^P = 0$), which does not require an estimate of the tangent stiffness matrix, is typically employed for the PS. The key advantage of velocity coupling is that global dynamic stability is ensured as long as local stability requirements are satisfied for all subdomains taken as stand-alone systems. Accordingly, a PS integration time step $\Delta t^P < T^P/\pi$ is selected, where T^P is the period corresponding to the highest eigen-frequency of the PS. It is important to stress that very few DoFs characterizes the PS, whose eigenfrequencies as a stand-alone system are typically restricted to a low frequency range, e.g. 0÷10Hz. In order to guarantee A-stability even for a large number of DoFs, the trapezoidal rule implicit scheme ($\gamma^N = 1/2$ and $\beta^N = 1/4$) is used on the NS. However, other time-stepping schemes can be used [18-20]. Hence,

Step 1. Solve the free problem in the NS, thus advancing from t_n to t_{n+2},

$$\ddot{\mathbf{u}}_{n+2}^{N,free} = \mathbf{D}^{N^{-1}} \left(\mathbf{F}_{n+2}^{N} - \mathbf{R}^N \left(\tilde{\mathbf{u}}_{n+2}^{N}, \tilde{\dot{\mathbf{u}}}_{n+2}^{N} \right) \right) \tag{B.4}$$

$$\dot{\mathbf{u}}_{n+2}^{N,free} = \tilde{\dot{\mathbf{u}}}_{n+2}^{N,free} + \gamma^N (2\Delta t^N) \ddot{\mathbf{u}}_{n+2}^{N,free} \tag{B.5}$$

$$\mathbf{u}_{n+2}^{N,free} = \tilde{\mathbf{u}}_{n+2}^{N,free} + \beta^N (2\Delta t^N)^{\mathbf{2}} \ddot{\mathbf{u}}_{n+2}^{N,free} \tag{B.6}$$

with,

$$\mathbf{D}^N = \mathbf{M}^N + \gamma^N (2\Delta t^N) \mathbf{C}^N + \beta^N (2\Delta t^N)^2 \mathbf{K}^N \tag{B.7}$$

$$\tilde{\mathbf{u}}_{n+2}^{N,free} = \mathbf{u}_n^N + (2\Delta t^N) \dot{\mathbf{u}}_n^N + (1/2 - \beta^N)(2\Delta t^N)^{\mathbf{2}} \ddot{\mathbf{u}}_n^N \tag{B.8}$$

$$\tilde{\dot{\mathbf{u}}}_{n+2}^{N,free} = \dot{\mathbf{u}}_n^N + (1 - \gamma^N)(2\Delta t^N) \ddot{\mathbf{u}}_{n+2}^{N,free} \tag{B.9}$$

In line with the Operator Splitting (OS) method [10], which underlays the one-step corrector solution approach of the PM algorithm, tangent stiffness and damping matrices of Eq. (B.7) are obtained by linearizing the restoring force vector as $\boldsymbol{K}^N = \left. \frac{\partial \boldsymbol{R}^N}{\partial \mathbf{u}^N} \right|_{\mathbf{u}^N = \mathbf{0}}$ and $\mathbf{C}^N = \left. \frac{\partial \boldsymbol{R}^N}{\partial \dot{\mathbf{u}}^N} \right|_{\dot{\mathbf{u}}^N = \mathbf{0}}$, respectively. In order to reduce the computational burden, this operation is done once at the beginning of the simulation and matrices are never updated. Particular care must be devoted to linearization error which remain negligible for sufficiently small time steps, as confirmed by numerical studies of Sections 4 and 5. When the NS restoring force is rate independent, a proportional formulation [21], e.g. Rayleigh or Caughey, is typically used to build up the damping matrix $\mathbf{C}^N$.

Step 2. Start the subcycling loop over $j = \{1, \dots, ss\}$ in the PS.

Step 3. Solve the free problem in the PS at $t_{n+\frac{j}{ss}}$ as,

$$\ddot{\mathbf{u}}^{P,free}_{n+\frac{j}{ss}} = \mathbf{D}^{P^{-1}} \left(\mathbf{F}^{P}_{n+\frac{j}{ss}} - \mathbf{R}^{P} \left(\tilde{\mathbf{u}}^{P}_{n+\frac{j}{ss}}, \tilde{\dot{\mathbf{u}}}^{P}_{n+\frac{j}{ss}} \right) \right) \tag{B.10}$$

$$\dot{\mathbf{u}}^{P,free}_{n+\frac{j}{ss}} = \tilde{\dot{\mathbf{u}}}^{P,free}_{n+\frac{j}{ss}} + \gamma^{P} (\Delta t^{P}) \ddot{\mathbf{u}}^{P,free}_{n+\frac{j}{ss}} \tag{B.11}$$

$$\mathbf{u}^{P,free}_{n+\frac{j}{ss}} = \tilde{\mathbf{u}}^{P,free}_{n+\frac{j}{ss}} + \beta^{P} (\Delta t^{P})^{\mathbf{2}} \ddot{\mathbf{u}}^{P,free}_{n+\frac{j}{ss}} \tag{B.12}$$

with,

$$\mathbf{D}^{P} = \mathbf{M}^{P} + \gamma^{P} \Delta t^{P} \mathbf{C}^{P} + \beta^{P} \Delta t^{P^{2}} \mathbf{K}^{P} \tag{B.13}$$

$$\tilde{\mathbf{u}}^{P,free}_{n+\frac{j}{ss}} = \mathbf{u}^{P}_{n+\frac{j-1}{ss}} + \Delta t^{P} \dot{\mathbf{u}}^{P}_{n+\frac{j-1}{ss}} + (1/2 - \beta^{P}) \Delta t^{P^{2}} \ddot{\mathbf{u}}^{P}_{n+\frac{j-1}{ss}} \tag{B.14}$$

$$\tilde{\dot{\mathbf{u}}}^{P,free}_{n+\frac{j}{ss}} = \dot{\mathbf{u}}^{P}_{n+\frac{j-1}{ss}} + (1 - \gamma^{P}) \Delta t^{P} \ddot{\mathbf{u}}^{P,free}_{n+\frac{j-1}{ss}} \tag{B.15}$$

In a real-time setting, both displacement and the velocity vectors, $\tilde{\mathbf{u}}^{P}_{n+\frac{j}{ss}}$ and $\tilde{\dot{\mathbf{u}}}^{P}_{n+\frac{j}{ss}}$, predicted by the Newmark scheme [18] are imposed onto the PS, so as to measure the rate dependent restoring force $\mathbf{R}^{P} \left(\tilde{\mathbf{u}}^{P}_{n+\frac{j}{ss}}, \tilde{\dot{\mathbf{u}}}^{P}_{n+\frac{j}{ss}} \right)$ to be used in (B.10). Conversely, a reduced velocity $\tilde{\dot{\mathbf{u}}}^{P}_{n+\frac{j}{ss}}/\lambda$ is physically imposed to the PS in the pseudo-dynamic regime. However, a rate-independent restoring term is expected in this case. With regard to Eq. (B.13), it is worthwhile to recall that an explicit Newmark integrator ($\beta^{P} = 0$) is used and, therefore, it is not necessary to estimate/measure the physical tangent stiffness matrix $\mathbf{K}^{P}$. Moreover, a perfectly hysteretic damping is assumed on the PS [22], which is taken into account through the measured restoring force $\mathbf{R}^{P} \left(\tilde{\mathbf{u}}^{P}_{n+\frac{j}{ss}}, \tilde{\dot{\mathbf{u}}}^{P}_{n+\frac{j}{ss}} \right)$. As a result, the physical tangent damping matrix $\mathbf{C}^{P}$ is set to zero and matrix $\mathbf{D}^{P}$ of Eq. (2.13) is simply defined as $\mathbf{D}^{P} = \mathbf{M}^{P}$. This is one of the most valuable features of the PM method, which avoids assumptions on PS tangent stiffness and damping matrices. It is important to stress that mass at interface DoFs can be arbitrarily moved from NS to PS, which imposes to numerically integrate the PS response as done on the NS. Accordingly, our implementation of HDS considers a numerical mass for the PS also in the real-time case. Although this could sounds as an unnecessary complication, such approach allows for controlling the stability domain of the coupled simulation [6].

Step 4. Interpolate the *free velocity* in subdomain,

$$\widetilde{\dot{\mathbf{u}}}^{N,free}_{n+\frac{j}{ss}} = \left(1-\frac{j}{ss}\right)\dot{\mathbf{u}}^{N,free}_{n} + \left(\frac{j}{ss}\right)\dot{\mathbf{u}}^{N,free}_{n+1} \tag{B.16}$$

Step 5. Compute the Lagrange multiplier sets $\mathbf{\Lambda}^{N}_{n+\frac{j}{ss}}$ and $\mathbf{\Lambda}^{P}_{n+\frac{j}{ss}}$ and the reference velocity vector $\dot{\mathbf{u}}_{g,n+\frac{j}{ss}}$ by solving the condensed interface problem,

$$\mathbf{G}\begin{bmatrix} \mathbf{\Lambda}^{N}_{n+\frac{j}{ss}} \\ \mathbf{\Lambda}^{P}_{n+\frac{j}{ss}} \\ \dot{\mathbf{u}}_{g,n+\frac{j}{ss}} \end{bmatrix} = -\begin{bmatrix} \boldsymbol{L}^{N}\dot{\mathbf{u}}^{N,free}_{n+\frac{j}{ss}} \\ \boldsymbol{L}^{P}\dot{\mathbf{u}}^{P,free}_{n+\frac{j}{ss}} \\ \mathbf{0} \end{bmatrix} \tag{B.17}$$

where the linearized Steklov-Poincaré operator G reads,

$$\mathbf{G} = \begin{bmatrix} \gamma^{N}(2\Delta t^{N})\mathbf{L}^{N}\mathbf{D}^{N^{-1}}\mathbf{L}^{N^{T}} & \mathbf{0} & \bar{\mathbf{L}}^{N} \\ \mathbf{0} & \gamma^{P}\Delta t^{P}\mathbf{L}^{P}\mathbf{D}^{P^{-1}}\mathbf{L}^{P^{T}} & \bar{\mathbf{L}}^{P} \\ \bar{\mathbf{L}}^{N^{T}} & \bar{\mathbf{L}}^{P^{T}} & \mathbf{0} \end{bmatrix} \tag{B.18}$$

Step 6. Solve the link problem in the PS at $t_{n+\frac{j}{ss}}$

$$\ddot{\mathbf{u}}^{P,link}_{n+\frac{j}{ss}} = \mathbf{D}^{P^{-1}}\mathbf{L}^{P}\mathbf{\Lambda}^{P}_{n+\frac{j}{ss}} \tag{B.19}$$

$$\dot{\mathbf{u}}^{P,link}_{n+\frac{j}{ss}} = \gamma^{P}\Delta t^{P}\ddot{\mathbf{u}}^{P,link}_{n+\frac{j}{ss}} \tag{B.20}$$

$$\mathbf{u}^{P,link}_{n+\frac{j}{ss}} = \beta^{P}\Delta t^{P^{2}}\ddot{\mathbf{u}}^{P,link}_{n+\frac{j}{ss}} \tag{B.21}$$

Step 7. Compute the kinematic quantities of the PS at $t_{n+\frac{j}{ss}}$, which is equal to the sum of *free quantities* (Step 3) and *link quantities* (Step 6)

$$(\cdot) = (\cdot)^{free} + (\cdot)^{link} \tag{B.22}$$

Step 8. If $j = ss$, then end the loop in the PS, otherwise $j = j + 1$ and go back to *Step 3*.

Step 9. Solve the *link problem* in the NS using the time step $\Delta t_N$from $\mathbf{t_n}$ to t_{n+1}

$$\ddot{\mathbf{u}}^{N,link}_{n+1} = \mathbf{D}^{N^{-1}}\mathbf{L}^{N}\mathbf{\Lambda}^{N}_{n+1} \tag{B.23}$$

$$\dot{\mathbf{u}}_{n+1}^{N,link} = \gamma^N (2\Delta t^N) \ddot{\mathbf{u}}_{n+1}^{N,link} \tag{B.24}$$

$$\mathbf{u}_{n+1}^{N,link} = \beta^N (2\Delta t^N)^2 \ddot{\mathbf{u}}_{n+1}^{N,link} \tag{B.25}$$

Step 10. Compute the kinematic quantities of the NS at t_{n+1} by employing the *free problem* (Step 1) and the *link problem* (Step 9)

$$(\cdot) = (\cdot)^{free} + (\cdot)^{link} \tag{B.26}$$

According to (B.12) and (B.21) when the central difference scheme is used on the PS, *link* displacements are null and corrections are exclusively needed for velocities and accelerations. As a result, the specimen smoothly follows the prototype response. In any case, the mass matrix $\mathbf{M}^P$ contributes to $\mathbf{D}^P$, which dominates the right-hand side of Eq. (B.13); thus, the physical link acceleration $\ddot{\mathbf{u}}_{n+\frac{j}{ss}}^{P,link}$ computed in Eq. (B.19) could generate discontinuities on actuator trajectories. Hence sometimes, it is convenient to modulate the magnitude of each *link* solution by moving interface mass from the NS to the PS. To this end, we can modulate the mass fraction parameter m_f for a generic *i-th* interface DoF. More precisely, m_f is defined as the ratio between physical and total interface mass,

$$m_{f,i} = \frac{M_i^P}{M_i^N + M_i^P} \tag{2.27}$$

where M_i^P and M_i^N are physical and numerical contributions to the mass of the *i-th* interface DoF. As a result, we can reduce the magnitude of physical link quantities by tuning m_f without affecting the structure prototype response. For the sake of brevity, the GC method procedure is omitted but can be easily derived by replacing the NS time step $(2\Delta t^N)$ with Δt^N in Eqs. (B.4) to (B.26).

2.1.3 Two offline experimental dynamic substructuring methods

As explained in Section 2, when offline EDS methods are used the experimental response of the PS needs to be acquired before the calculation of the emulated system response. In this context, both the Impulse-Based Substructuring (IBS) [13, 14] and the Receptance-Based Substructuring (RBS) method, which is formally derived from the LM-FBS method of Voormeeren et al. [15] are presented in the following subsections. The former operates in time domain and the PS is represented in terms of measured Impulse Response Functions (IRFs); the latter operates in the Laplace domain and measured Receptance Functions (RFs) account for the PS response. Both methods rely on operational and experimental modal analysis tools such as accelerometers, shakers and impact hammers. The IBS methods allows for combining linear PSs to non-linear NSs whilst the RBS can be used for both coupling and decoupling linear NSs and PSs.

2.1.4 The impulse-based substructuring method

The easiest way to introduce the IBS framework is to briefly revisit the equation of motion of a generic M-DoF linear dynamic system subjected to an arbitrary force vector $\mathbf{F}(t)$,

$$\mathbf{M\ddot{u}} + \mathbf{C\dot{u}} + \mathbf{Ku} = \mathbf{F}(t) \tag{B.28}$$

Let us designate $\mathbf{H}_d(t)$ the matrix of the displacement response for a linear system that is at rest at $t = 0$ and is subjected to a unit impulse excitation applied to a specific DoF, described by a Dirac δ function. The elements $[\mathbf{H}_d(t)]_{ij}$ of the impulse response matrix represent the displacement response of DoF i to a unit impulse at DoF j. Since any arbitrary force function of time can be expressed as a sequence of force impulses over time, the impulse response functions can be used to evaluate the response of a generic system in the time domain. As a result, the displacement response of the linear system can be evaluated through the Duhamel's convolution integral between $\mathbf{H}_d(t)$ and $\mathbf{F}(t)$,

$$\mathbf{u}(t) = \int_0^t \mathbf{H}_d(t-\tau)\mathbf{F}(\tau)\mathrm{d}\tau \tag{B.29}$$

Likewise, velocity and acceleration responses can be evaluated as follows,

$$\dot{\mathbf{u}}(t) = \int_0^t \mathbf{H}_{\mathrm{v}}(t-\tau)\mathbf{F}(\tau)\mathrm{d}\tau \tag{B.30}$$

$$\ddot{\mathbf{u}}(t) = \int_0^t \mathbf{H}_a(t-\tau)\mathbf{F}(\tau)\mathrm{d}\tau \tag{B.31}$$

where $\mathbf{H}_v(t)$ and $\mathbf{H}_a(t)$ are the first and second time derivatives of $\mathbf{H}_d(t)$, respectively. Clearly,$\mathbf{H}_d(t)$, $\mathbf{H}_v(t)$ and $\mathbf{H}_a(t)$ contain information on the input-output relationship of the system dynamics. Typically, the following convolution sums are used in a discrete-time setting,

$$\mathbf{u}_n = \sum_{i=0}^{n} \mathbf{H}_{d,n-i}\mathbf{F}_i\,\Delta t \tag{B.32}$$

$$\dot{\mathbf{u}}_n = \sum_{i=0}^{n} \mathbf{H}_{v,n-i}\mathbf{F}_i\,\Delta t \tag{B.33}$$

$$\ddot{\mathbf{u}}_n = \sum_{i=0}^{n} \mathbf{H}_{a,n-i}\mathbf{F}_i\,\Delta t \tag{B.34}$$

The previous equations approximate the exact convolution integrals (B.29-B.31) and, therefore, the IRF matrices are discretized according to the sampling rate of $\mathbf{F}(t)$. In a greater detail, $\mathbf{H}_{*,n-i}$ corresponds to the IRF matrix $\mathbf{H}_*(t)$ evaluated at $t = \Delta t \cdot (n-i)$. In principle, $\mathbf{H}_d(t)$ can be obtained: i) analytically, relying on matrix exponentials -this method ensures the exact sampling of the impulse response function-; ii) numerically, by simulating the dynamic response of the system subjected to an impulse load by means of a time history response analysis; iii) experimentally, by using impact hammers and accelerometers. The resulting discretized coupled equations of motion for a two-subdomain system read,

$$\begin{cases} \mathbf{M}^N \ddot{\mathbf{u}}_n^N + \mathbf{R}^N(\mathbf{u}_n^N, \dot{\mathbf{u}}_n^N) = \mathbf{L}^{N^T} \boldsymbol{\Lambda}_n^N + \boldsymbol{F}_n^N \\ \dot{\mathbf{u}}_n^P = \sum_{i=0}^{n} \mathbf{H}_{v,n-i}^P \left(\mathbf{L}^{P^T} \boldsymbol{\Lambda}_i^{\boldsymbol{P}} + \mathbf{F}_i^P \right) \Delta t \end{cases} \tag{B.35}$$

$$\begin{cases} \mathbf{L}^N \dot{\mathbf{u}}_n^N + \bar{\mathbf{L}}^N \dot{\mathbf{u}}_{g,n} = \mathbf{0} \\ \mathbf{L}^P \dot{\mathbf{u}}_n^P + \bar{\mathbf{L}}^P \dot{\mathbf{u}}_{g,n} = \mathbf{0} \end{cases} \tag{B.36}$$

$$\bar{\mathbf{L}}^{N^T} \boldsymbol{\Lambda}_n^N + \bar{\mathbf{L}}^{P^T} \boldsymbol{\Lambda}_n^P = \mathbf{0} \tag{B.37}$$

The solution of (B.35) is obtained by discretizing the time integral needed to evaluate the convolution product and to solve for the additional interface force fields $\boldsymbol{\Lambda}_n^N$ and $\boldsymbol{\Lambda}_n^P$ at each step $\boldsymbol{n}$, which ensures the interface kinematic continuity. It is noteworthy that the original IBS algorithm [13] was conceived to combine exclusively subdomains represented in terms of impulse response matrices. In our hybrid experimental/numerical setting, only the PS is represented in terms of its impulse response matrices, whilst the NS is integrated using a Newmark-based time stepping scheme [18], which can also account for nonlinearities [14]. According to Gravouil and Combescure [16], in order to obtain an unconditionally stable algorithm, as long as stability requirements are satisfied in all individual subdomains, a velocity continuity condition at the interface DoFs suffices; this is achieved in Eq. (B.36). The implementation of the IBS algorithm based on the coupled scheme of the GC method is summarized herein for the case without subcycling, that is, $\Delta t^P = \Delta t^N = \Delta t$.

Step 1. Solve the free problem in the NS, thus advancing from $\boldsymbol{t_n}$ to $\boldsymbol{t_{n+1}}$,

$$\ddot{\mathbf{u}}_{n+1}^{N,free} = \mathbf{D}^{N^{-1}} \left(\mathbf{F}_{n+1}^N - \mathbf{R}^N \left(\tilde{\mathbf{u}}_{n+1}^N, \tilde{\dot{\mathbf{u}}}_{n+1}^N \right) \right) \tag{B.38}$$

$$\dot{\mathbf{u}}_{n+1}^{N,free} = \tilde{\dot{\mathbf{u}}}_{n+1}^{N,free} + \gamma^N \Delta t \ddot{\mathbf{u}}_{n+1}^{N,free} \tag{B.39}$$

$$\mathbf{u}_{n+1}^{N,free} = \tilde{\mathbf{u}}_{n+1}^{N,free} + \beta^N \Delta t^{\mathbf{2}} \ddot{\mathbf{u}}_{n+1}^{N,free} \tag{B.40}$$

with,

$$\mathbf{D}^N = \mathbf{M}^N + \gamma^N \Delta t \mathbf{C}^N + \beta^N \Delta t^2 \mathbf{K}^N \tag{B.41}$$

$$\tilde{\mathbf{u}}_{n+1}^{N,free} = \mathbf{u}_n^N + \Delta t \dot{\mathbf{u}}_n^N + (1/2 - \beta^N) \Delta t^2 \ddot{\mathbf{u}}_n^N \tag{B.42}$$

$$\tilde{\dot{\mathbf{u}}}_{n+1}^{N,free} = \dot{\mathbf{u}}_n^N + (1 - \gamma^N) \Delta t \ddot{\mathbf{u}}_{n+1}^{N,free} \tag{B.43}$$

As analogously done in Eq. (B.7) for the HDS method, tangent stiffness and damping matrices of Eq. (B.41) are obtained by linearizing the restoring force vector as $\boldsymbol{K}^N = \frac{\partial \boldsymbol{R}^N}{\partial \mathbf{u}^N}\Big|_{\mathbf{u}^N = \mathbf{0}}$ and $\mathbf{C}^N =$

$\left.\frac{\partial \boldsymbol{R}^N}{\partial \dot{\mathbf{u}}^N}\right|_{\dot{\mathbf{u}}^N=\mathbf{0}}$, respectively. In order to reduce the computational burden, this operation is done once at the beginning of the simulation and matrices are never updated. Particular care must be devoted to linearization errors which remain negligible for sufficiently small time steps, as confirmed by numerical studies of Section 1.2.6. When the NS restoring force is rate independent, a proportional formulation [21], e.g. Rayleigh or Caughey, is typically used to build up the damping matrix $\mathbf{C}^N$.

Step 2. Solve the *free problem* in the PS at from $\boldsymbol{t}_n$ to $\boldsymbol{t}_{n+1}$,

$$\ddot{\mathbf{u}}_{n+1}^{P,free} = \sum_{i=0}^{n} \mathbf{H}_{a,n+1-i}^{P} \left(\mathbf{L}^{P^T} \boldsymbol{\Lambda}_i^P + \boldsymbol{F}_i^P \right) \Delta t + \mathbf{H}_{a,0}^{P} \boldsymbol{F}_{n+1}^{P} \Delta t \tag{B.44}$$

$$\dot{\mathbf{u}}_{n+1}^{P,free} = \sum_{i=0}^{n} \mathbf{H}_{v,n+1-i}^{P} \left(\mathbf{L}^{P^T} \boldsymbol{\Lambda}_i^P + \boldsymbol{F}_i^P \right) \Delta t + \mathbf{H}_{v,0}^{P} \boldsymbol{F}_{n+1}^{P} \Delta t \tag{B.45}$$

$$\mathbf{u}_{n+1}^{P,free} = \sum_{i=0}^{n} \mathbf{H}_{v,n+1-i}^{P} \left(\mathbf{L}^{P^T} \boldsymbol{\Lambda}_i^P + \boldsymbol{F}_i^P \right) \Delta t + \mathbf{H}_{d,0}^{P} \boldsymbol{F}_{n+1}^{P} \Delta t \tag{B.46}$$

According to (B.44-B.46) convolution series are truncated at $\boldsymbol{n}$ because the interface force field $\boldsymbol{\Lambda}_{n+1}^P$ is unknown at this point of the procedure. As a result, the external load $\boldsymbol{F}_{n+1}^P$ only determines the last step of the free solution.

Step 3. Compute the Lagrange multiplier sets $\boldsymbol{\Lambda}_{n+1}^N$ and $\boldsymbol{\Lambda}_{n+1}^P$ and the reference velocities $\dot{\mathbf{u}}_{g,n+1}$ by solving the condensed interface problem

$$\mathbf{G} \begin{bmatrix} \boldsymbol{\Lambda}_{n+1}^N \\ \boldsymbol{\Lambda}_{n+1}^P \\ \dot{\mathbf{u}}_{g,n+1} \end{bmatrix} = - \begin{bmatrix} \boldsymbol{L}^N \dot{\mathbf{u}}_{n+1}^{N,free} \\ \boldsymbol{L}^P \dot{\mathbf{u}}_{n+1}^{P,free} \\ \mathbf{0} \end{bmatrix} \tag{B.47}$$

where,

$$\mathbf{G} = \begin{bmatrix} \gamma^N \Delta t \mathbf{L}^N \mathbf{D}^{N^{-1}} \mathbf{L}^{N^T} & \mathbf{0} & \bar{\mathbf{L}}^N \\ \mathbf{0} & \mathbf{L}^P \mathbf{H}_{v,0}^P \mathbf{L}^{P^T} & \bar{\mathbf{L}}^P \\ \bar{\mathbf{L}}^{N^T} & \bar{\mathbf{L}}^{P^T} & \mathbf{0} \end{bmatrix} \tag{B.48}$$

Step 4. Solve the *link problem* in the PS at $\boldsymbol{t}_{n+1}$

$$\ddot{\mathbf{u}}_{n+1}^{P,link} = \mathbf{H}_{a,0}^{P} \boldsymbol{\Lambda}_{n+1}^{P} \tag{B.49}$$

$$\dot{\mathbf{u}}_{n+1}^{P,link} = \mathbf{H}_{v,0}^{P} \boldsymbol{\Lambda}_{n+1}^{P} \tag{B.50}$$

$$\mathbf{u}_{n+1}^{P,link} = \mathbf{H}_{d,0}^{P} \mathbf{\Lambda}_{n+1}^{P} \tag{B.51}$$

Step 5. Compute the kinematic quantities of the PS at t_{n+1}, which is equal to the sum of *free quantities* (Step 2) and *link quantities* (Step 4)

$$(\cdot) = (\cdot)^{free} + (\cdot)^{link} \tag{B.52}$$

Step 6. Solve the *link problem* in the NS using the time step Δt_N from t_n to t_{n+1}

$$\ddot{\mathbf{u}}_{n+1}^{N,link} = \mathbf{D}^{N^{-1}} \mathbf{L}^{N} \mathbf{\Lambda}_{n+1}^{N} \tag{B.53}$$

$$\dot{\mathbf{u}}_{n+1}^{N,link} = \gamma^{N} \Delta t \ddot{\mathbf{u}}_{n+1}^{N,link} \tag{B.54}$$

$$\mathbf{u}_{n+1}^{N,link} = \beta^{N} \Delta t^{2} \ddot{\mathbf{u}}_{n+1}^{N,link} \tag{B.55}$$

Step 7. Compute the kinematic quantities of the NS at t_{n+1} by employing the *free problem* (Step 1) and the *link problem* (Step 6)

$$(\cdot) = (\cdot)^{free} + (\cdot)^{link} \tag{B.56}$$

In order to account for various sources of uncertainty, which contaminate the "exact" impulse response functions, the process of measuring $\mathbf{H}_d^P(t), \mathbf{H}_v^P(t)$ and $\mathbf{H}_a^P(t)$ matrices from hammer tests on the PS was simulated numerically.

2.1.5 The receptance-based substructuring method

Under the assumption that both NS and PS are linear -or linearized-, time invariant and operating at steady state, the LM-FBS method can be derived by Fourier transform of Eq. (B.1-B.2) [15]. However, the use of the Fourier transform is limited to periodic signals and, therefore, to stationary response analyses. Accordingly, the inverse Fourier transform cannot revert the dynamic response of the coupled system subjected to a transient excitation calculated in the frequency domain to the time domain. Therefore, the FBS method is reformulated in the Laplace domain as Receptance-Based Substructuring (RBS) method. The joint use of numerical Laplace transform and its inverse allowed for including the RBS method in the comparative uncertainty propagation analysis that quantifies the effect of various experimental sources of uncertainty on the time domain response of two benchmark systems subjected to a non-stationary excitation. A detailed description of the algorithm follows,

$$\begin{cases} \pm \mathbf{Z}^{N}(s)\mathbf{u}^{N}(s) = \mathbf{L}^{N^{T}} \mathbf{\Lambda}^{N}(s) + \mathbf{F}^{N}(s) \\ \mathbf{Z}^{P}(s)\mathbf{u}^{P}(s) = \mathbf{L}^{P^{T}} \mathbf{\Lambda}^{P}(s) + \mathbf{F}^{P}(s) \end{cases} \tag{B.57}$$

$$\begin{cases} \mathbf{L}^N \mathbf{u}^N(s) + \bar{\mathbf{L}}^N \mathbf{u}_g(s) = \mathbf{0} \\ \mathbf{L}^P \mathbf{u}^P(s) + \bar{\mathbf{L}}^P \mathbf{u}_g(s) = \mathbf{0} \end{cases} \tag{B.58}$$

$$\bar{\mathbf{L}}^{N^T} \mathbf{\Lambda}^N(s) + \bar{\mathbf{L}}^{P^T} \mathbf{\Lambda}^P(s) = \mathbf{0} \tag{B.59}$$

where s denotes the complex Laplace variable such that $Real(s) = \alpha$ and $Imag(s) = \omega$ whilst $\mathbf{Z}^N(s)$ and $\mathbf{Z}^P(s)$ are the impedance matrices of the NS and PS, respectively, calculated as,

$$\mathbf{Z}^{(l)} = \mathbf{M}^{(l)} s^2 + \mathbf{C}^{(l)} s + \mathbf{K}^{(l)} \tag{B.60}$$

In order to avoid the singularity of coupling operators for all values of s, compatibility conditions must be expressed in terms of displacements as in Eq. (B.58). The set of Eqs. (B.57-B.59) encompasses both substructure coupling and decoupling cases. In fact, the $\pm$ sign before $\mathbf{Z}^N$ indicates that the NS can be either added to or subtracted from the PS. The former is the case where two substructures form the global emulated system but only one is measured in the laboratory; the latter case occurs, for example, when the substructure of interest cannot be separately measured from a system with well-known dynamic properties, which is subtracted numerically afterwards [23].

Analogously to the IBS method, the RBS method relies on operational modal analysis tools such as impact hammers, shakers and accelerometers. In detail, each component $[\mathbf{Y}^P(s)]_{ij}$ of the PS receptance matrix $\mathbf{Y}^P(s) = \mathbf{Z}^{P^{-1}}(s)$ is typically calculated as the ratio between Laplace transforms of displacement response and loading excitation and measured at DoFs i and j, respectively. The trapezoidal rule is used to evaluate all Laplace integrals over a range of ω that includes all system and excitation frequencies assuming a constant and negative value of α, which is optimized according to the time span of the signals. The RBS algorithm expressed in terms of directly measurable receptance matrices reads,

$$\mathbf{u}(\mathbf{s}) = \mathbf{Y}(s)\big(\mathbf{F}(s) + \mathbf{L}^T \mathbf{\Lambda}(s)\big) \tag{B.61}$$

$$\mathbf{\Lambda}(\mathbf{s}) = -(\mathbf{L}\mathbf{Y}(s)\mathbf{L}^T)^{-1}\left(\mathbf{L}\mathbf{Y}(s)\mathbf{F}(s) + \bar{\mathbf{L}}\mathbf{u}_g(\mathbf{s})\right) \tag{B.62}$$

$$\mathbf{u}_g(\mathbf{s}) = -(\bar{\mathbf{L}}^T(\mathbf{L}\mathbf{Y}(s)\mathbf{L}^T)^{-1}\bar{\mathbf{L}})^{-1}(\bar{\mathbf{L}}^T(\mathbf{L}\mathbf{Y}(s)\mathbf{L}^T)^{-1}\mathbf{L}\mathbf{Y}(s)\mathbf{F}(s)) \tag{B.63}$$

where block matrices and vectors $\mathbf{u}, \mathbf{Y}, \mathbf{L}, \bar{\mathbf{L}}$ and $\mathbf{F}$ are defined as,

$$\mathbf{u}(s) = \begin{bmatrix} \mathbf{u}^N(s) \\ \mathbf{u}^P(s) \end{bmatrix}, \mathbf{Y}(s) = \begin{bmatrix} \pm\mathbf{Y}^N(s) & \mathbf{0} \\ \mathbf{0} & \mathbf{Y}^P(s) \end{bmatrix}, \mathbf{F}(s) = \begin{bmatrix} \mathbf{F}^N(s) \\ \mathbf{F}^P(s) \end{bmatrix}, \mathbf{\Lambda}(s) = \begin{bmatrix} \mathbf{\Lambda}^N(s) \\ \mathbf{\Lambda}^P(s) \end{bmatrix}, \quad \mathbf{L} = \begin{bmatrix} \mathbf{L}^N & \mathbf{0} \\ \mathbf{0} & \mathbf{L}^P \end{bmatrix}, \bar{\mathbf{L}} = \begin{bmatrix} \bar{\mathbf{L}}^N \\ \bar{\mathbf{L}}^P \end{bmatrix} \tag{B.64}$$

Although (B.57-B.59) refers to the collocated case, the dual formulation allows for non-collocated setting, i.e. interface force fields and compatibility conditions defined on different DoF subsets. The superior versatility and performance with respect to noise propagation of the non-collocated approach is well documented for the case of interface rotational DoFs [24].

In order to examine the practical implementation of the RBS method, the characterization of the PS receptance matrix $\mathbf{Y}^P(s)$ by means of hammer tests was simulated numerically considering as experimental sources of uncertainty both the variability of hammer impacts and noise on acceleration measurements.

In order to convert the emulated system response $\mathbf{u}(s)$ from the Laplace domain to the time domain, where it can be easily compared to both HDS and IBS simulations, the truncated series proposed by Durbin [31] is used to approximate inverse Laplace transform integrals,

$$f(t) = \mathcal{L}^{-1}\{F(s)\} \approx \frac{2e^{\alpha t}}{T}\left(-\frac{Re\big(F(\alpha)\big)}{2} + \sum_{k=1}^{q} Re\left(F\left(\alpha + i\frac{2\pi k}{T}\right)\right) cos\left(\frac{2\pi k}{T}t\right) - Im\left(F\left(\alpha + i\frac{2\pi k}{T}\right)\right) sin\left(\frac{2\pi k}{T}t\right)\right) \tag{B.65}$$

where $\mathcal{L}^{-1}\{\cdot\}$ represents the inverse Laplace transform operator, $F(s)$ is the Laplace transform of a generic time domain signal $f(t)$ of length T in s, α is a convergence parameter that constitutes the real part of the Laplace variable and q defines the number of terms, equal to 10^4 in our simulations, retained by the truncated series.

It is noteworthy that impulse response matrices defined by (B.29-B.31) can be derived from corresponding receptance matrices via inverse Laplace transform as,

$$\left[\mathbf{H}_a^{(l)}(t)\right]_{ij} = \mathcal{L}^{-1}\left\{\left[\mathbf{Y}^{(l)}(s)\right]_{ij}\right\}(t) \tag{B.66}$$

$$\left[\mathbf{H}_v^{(l)}(t)\right]_{ij} = \mathcal{L}^{-1}\left\{\left[s\mathbf{Y}^{(l)}(s)\right]_{ij}\right\}(t) \tag{B.67}$$

$$\left[\mathbf{H}_a^{(l)}(t)\right]_{ij} = \mathcal{L}^{-1}\left\{\left[s^2\mathbf{Y}^{(l)}(s)\right]_{ij}\right\}(t) \tag{B.68}$$

Accordingly, in the context of C-EDS, the truncated series of Eq. (B.65) is also proposed to convert coupled/decoupled receptance matrices to impulse response matrices, which can be used in combination with IBS and HDS methods.

2.1.6 Application of the C-EDS method to a petrochemical prototype plant

In order to highlight the versatility of the presented C-EDS framework in combining radically different EDS methods for simulating the response of heterogeneous systems, a virtual experiment was conducted on the petrochemical prototype plant case study depicted in Fig. B.11. In this prototype example, all the PSs are simulated numerically in a noise-free condition.

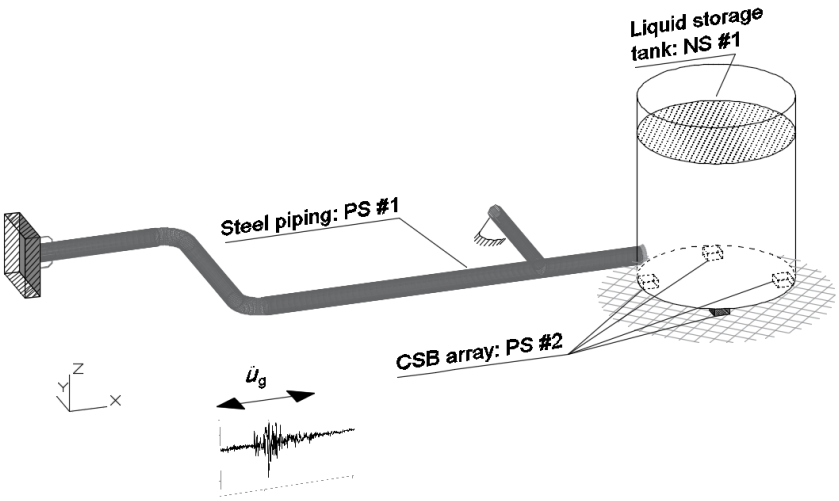

Fig. B.11. Petrochemical prototype plant case study with highlighted substructures.

As shown in Fig. B.11, four concave sliding bearings (CSBs) support a liquid storage tank that is connected to a steel piping. Water at ambient temperature fills both the tank and the piping. The same accelerogram of the 1989 Loma Prieta earthquake with 4.25 m/s^2 PGA, was selected as the reference seismic excitation signal. The goal of this virtual experiment is to estimate residual displacements of CSBs, which must remain small to guarantee safe operating conditions for the piping system. To this end, a simulator of the petrochemical plant case study was developed by combining different PSs and NSs by means of the presented C-EDS framework.

It was assumed that the piping response remains linear but boundary conditions are highly uncertain. However, such substructure is available onsite for dynamic characterization; offline EDS can be conveniently used to emulate its response. On the other hand, the difficulty in the modelling of friction effects between sliding parts, which depends on speed, vertical load, temperature and wear [25], justifies the use of online EDS to account for the non-linear hysteretic response of the CSB array that can be tested in the laboratory. Under these premises, Fig. B.12 depicts a schematic of the substructuring configuration assumed for the virtual experiment.

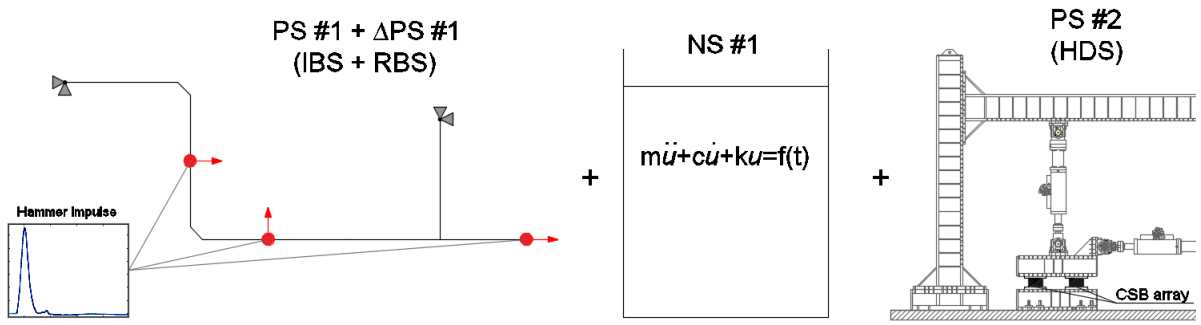

Fig. B.12. Substructuring schematics of the petrochemical prototype plant case study.

As can be appreciated from Fig. B.12, an impulse response matrix is needed to represent the piping system -PS #1-, which is characterized offline by using the RBS, whilst the sliding liquid storage tank with sloshing fluid -NS #1- is numerically simulated. Consequently, in order to account for the hysteretic response of the CSB array -PS #2-, which was tested in the laboratory, IBS and HDS methods were combined. Detailed descriptions of all substructures as well as the main results of the virtual C-EDS experiment are reported in the next subsections.

2.1.6.1 Physical piping system

The piping system combines 40 straight elements of 8" (outer diameter: 219.08 mm; thickness: 8.18 mm) and 6" diameter (outer diameter: 168.28 mm; thickness: 7.11 mm) and several critical components such as elbows and one tee joint. API 5L Gr. X52 steel material (nominal yield strength f_y and tensile strength f_u equal to $418\ MPa$ and 554 MPa, respectively) characterizes all elements. A temporary support frame, which will be replaced by the liquid storage tank, provides additional mass and stiffness to the displacement DoF of the end flange of the piping system in the *X* direction. Three accelerometers are installed on the system, which was assumed to be available onsite for experimental modal analysis based on hammer tests. Fig. B.13 depicts the piping system including the temporary support frame and the locations of three accelerometers.

2.1.6.2 Bending and shear - construction phase

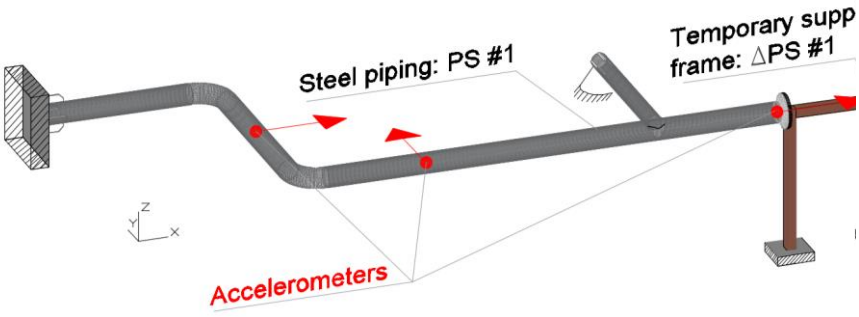

	Modal Frequency [Hz]	
Mode	PS #1+ΔPS #1	PS #1
1	7.13	6.77
2	12.60	13.16
3	15.96	29.71
4	29.72	114.54

Fig. B.13. Piping system with main dimensions and locations of accelerometers for experimental modal analysis.

In order to simulate the substructuring process, the 30-DoF FE model of the piping system including the temporary support frame, which is depicted in Fig. B.14, was implemented. All pipes including elbows were modelled using straight beam elements with an equivalent linear stiffness. An equivalent material density accounts for filling water at 3.2 MPa pressure [12]. Two additional lumped masses $M_v = 1e3\ kg$ account for valves and other components connected to the piping system whilst the lumped mass $M_f = 1e3\ kg$ and the stiffness $K_f = 1e5\ N/m$ simulate the effect of the temporary support frame.

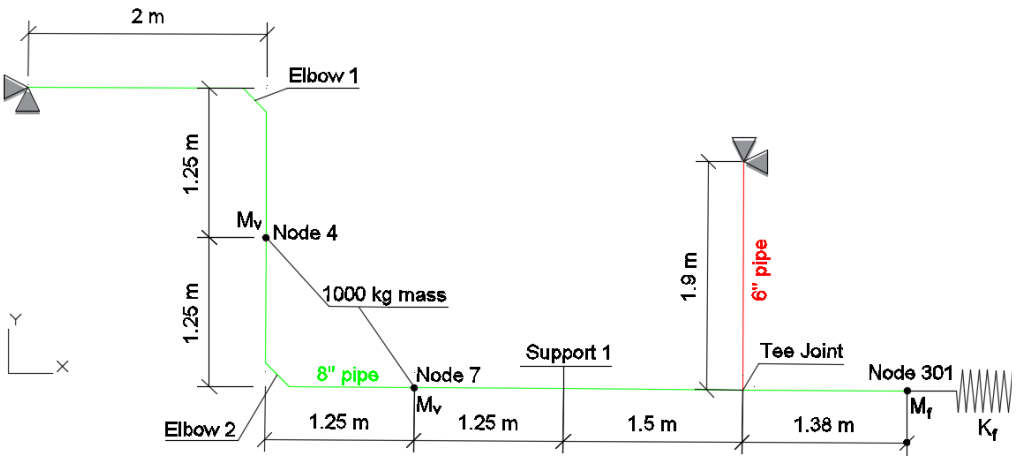

Fig. B.14. FE model and main characteristics of both piping system and temporary support frame.

The receptance matrices of the piping system with temporary support frame -PS #1 + ΔPS #1- and the temporary support frame alone -ΔPS #1- were calculated according to Eq. (B.60) based on FE matrices. Subsequently, the DoFs measured by accelerometers were retained via static condensation. In order to obtain the receptance matrix of the piping system alone -PS #1-, RBS was used to subtract the contribution of the temporary support frame -ΔPS #1- from the measured receptance matrix of the entire system, i.e. the piping system connected to the temporary support frame -PS #1 + ΔPS #1-. Finally, the corresponding impulse response matrix was calculated via numerical inverse Laplace transform according to Eqs. (B.66-B.68), considering $\alpha = 0.2, T = 15\ s$ and $q = 1e4$. Fig. 15 compares coupled/decoupled receptance and impulse response functions and relevant reference solutions analytically obtained from the FE matrices of the piping system according to Eq. (B.60).

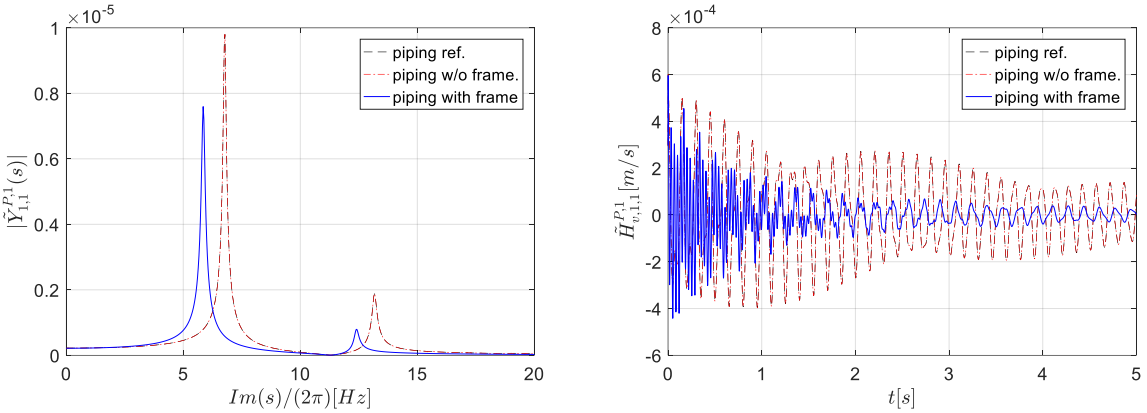

Fig. B.15. EDS of the piping system: a) receptance function -Laplace domain- and b) corresponding impulse response function -time domain- relevant to Node #301, dir. X.

In Fig. B.15, the label "piping ref." designates the reference analytical response, derived from FE matrices of the piping system alone; "piping with frame" represents the piping coupled with the anchorage frame whilst "piping w/o frame" indicates the decoupled piping network after RBS. As can be appreciated from Fig. B.15 where curves of "piping ref" and "piping w/o frame" overlap, the procedure yields an accurate estimation of impulse response functions that can be used for time history response analysis with the IBS. In order to solve Eq. (B.35), the last step of the EDS of the piping network consists in condensing the external load vector to the set of retained DoFs measured by the accelerometers. Accordingly, the approach suggested by Bursi and co-workers [12] was followed, which relies on the Guyan method [39]. First, the stiffness matrix of the piping system extracted from the relevant FE model was partitioned according to the retained (r) and discarded (d) DoFs.

$$\mathbf{K}^{P,1} = \begin{bmatrix} \mathbf{K}^{P,1}_{rr} & \mathbf{K}^{P,1}_{rd} \\ \mathbf{K}^{P,1}_{dr} & \mathbf{K}^{P,1}_{dd} \end{bmatrix} \tag{B.69}$$

Then, the matrix of restraint modes $\boldsymbol{\Phi}^{P,1}$ was derived as,

$$\boldsymbol{\Phi}^{P,1} = \begin{bmatrix} \mathbf{I}_{rr} \\ -\mathbf{K}^{P,1^{-1}}_{dd}\mathbf{K}^{P,1}_{dr} \end{bmatrix} \tag{B.70}$$

where $\mathbf{I}_{rr}$is an identity square matrix of size equal to the number of retained DoFs. Thus, restraint modes were used to condense the external seismic load to the master DoFs.

$$\tilde{\mathbf{F}}^{P,1}(t) = -\boldsymbol{\phi}^{P,1^T}\mathbf{M}^{P,1}\mathbf{T}^{P,1}a_g(t) \tag{B.71}$$

Impulse response matrices $\tilde{\mathbf{H}}_d^{P,1}(t)$, $\tilde{\mathbf{H}}_v^{P,1}(t)$ and $\tilde{\mathbf{H}}_a^{P,1}(t)$ and external vector $\tilde{\mathbf{F}}^{P,1}(t)$ emulate the response of the piping network -PS #1- within the coupled simulation. The tilde "hats" emphasize the Guyan condensation to the retained DoFs.

2.1.6.3 Physical concave sliding bearing array

An array of 2x2 CSBs with a single sliding surface -PS #2- supports the liquid storage tank; therefore, we use HDS to emulate the non-linear hysteretic response of the seismic isolation devices through virtual testing in the laboratory. Fig. B.16 depicts the adopted CSB as well as the test setup for HDS.

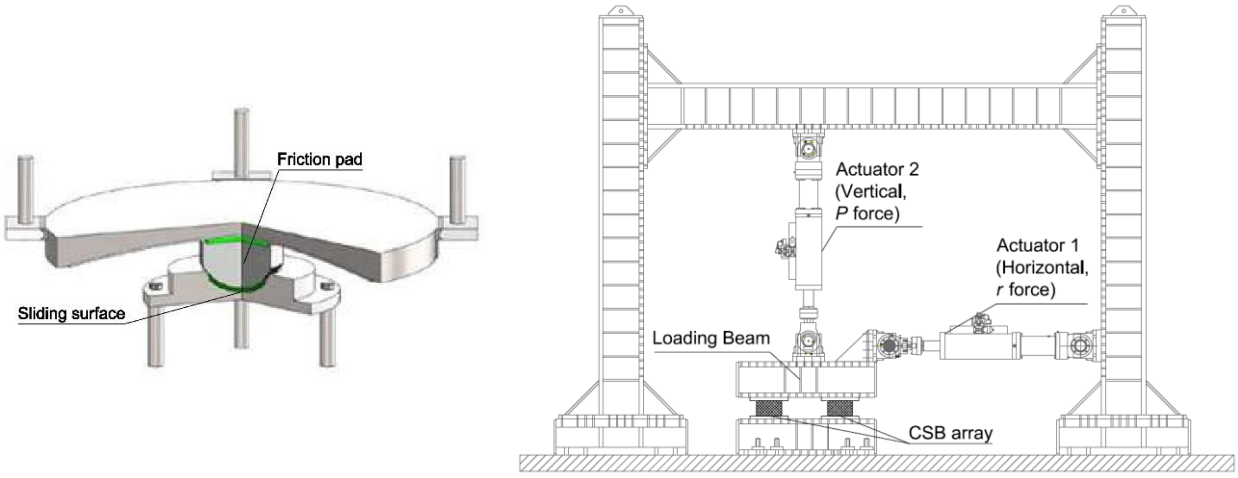

a b

Fig. B.16. Details of the CSB and test setup of the CSB array.

Since the variability in the force response among different devices is small, it is reasonable to test a reduced CSB array in the laboratory and multiply the measured restoring force so as to simulate the full CSB array. Thus, as can be appreciated in Fig. B.16b, only two CSBs out of four were virtually tested in the laboratory. An example of a more complex testing setup for CSBs, which controls tilting angles and out-of-plane moments can be found in [7-8]. From a mechanical viewpoint, a single CSB device can be characterized by a simplified linear piece-wise force-displacement relationship,

$$\begin{cases} r = \dfrac{\mu_f P}{\Delta}u, u \le \Delta \\ r = \mu_f \,\mathrm{sign}(\dot{u})P + \dfrac{P}{R}u, u > \Delta \end{cases} \tag{B.72}$$

where μ_f is the friction coefficient, R is the device curvature radius, $\dot{u}$ and u are the instantaneous velocity and sliding displacement of the isolator, respectively; *P* is a constant vertical load whilst r is the transversal restoring force of the CSB, which are measured by both vertical and horizontal actuators of Fig. B.16, respectively. More precisely, all CSB devices are characterized by surface radius R equal to $5000\ mm$, friction coefficient μ_f equal to $8\ \%$ and initial yield displacement Δ of $0.5\ mm$. Moreover, each single CSB device carries a vertical load P equal to $1360\ kN$, which corresponds to one fourth of the weight of the liquid storage tank filled with water up to its maximum capacity.

The interaction of multiple displacement-controlled actuators, connected to the same very stiff specimen, can easily trigger dynamic instability. In order to overcome this problem, common testing practice of seismic isolation devices consists in applying the nominal value of vertical loading via force control and imposing transverse displacement via position control.

In order to replicate the slip-based behaviour of the CSB array -PS #2- the differential model proposed by Mostaghel [27] was adopted. Fig. B.17 shows both a schematic of the aforementioned model and its bilinear hysteretic loop.

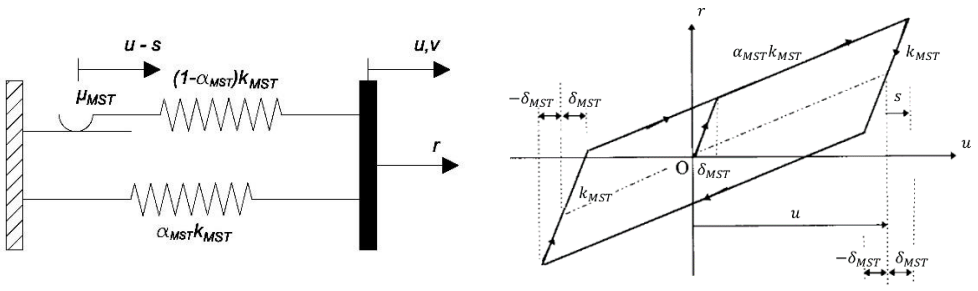

a b

Fig. B.17. Bilinear Mostaghel model: a) S-DoF idealization; b) Hysteretic loop.

The corresponding ODE set, which defines the hysteretic Mostaghel model subjected to a given velocity history $v(t)$, reads,

$$\begin{cases} \dot{r} = \left(\alpha_{MST}k_{MST} + (1-\alpha_{MST})k_{MST}\left(\bar{N}(v)\bar{M}(s-\delta_{MST}) + M(v)N(s+\delta_{MST})\right)\right)v \\ \dot{u} = v \end{cases} \tag{B.73}$$

with,

$$s = \frac{r - \alpha_{MST}k_{MST}u}{(1-\alpha_{MST})k_{MST}} \tag{B.74}$$

where, u and r represents displacement and restoring force state variables of the element and s defines slip displacement. The remaining functions $N, M, \bar{N}$ and $\bar{M}$ read,

$$\begin{aligned} N(w) &= 0.5\big(1+sgn(w)\big)\Big(1+\big(1-sgn(w)\big)\Big) \\ M(w) &= 1 - N(w) \end{aligned} \tag{B.75}$$

$$\bar{N}(w) = M(-w)$$
$$\bar{M}(w) + N(-w)$$

where $sgn(\cdot)$ is the sign function. The parameters k_{MST}, α_{MST} and δ_{MST} represent initial stiffness, post-yielding stiffness reduction factor and yielding displacement of a single CSB device, respectively. They are related to the physical parameters of the CSB model of Eq. (B.72) as,

$$\begin{aligned} \delta_{MST} &= \Delta = 5e-4\ m \\ \alpha_{MST} &= \frac{\Delta}{\mu_f R} = 1.30e-3 \\ k_{MST} &= \frac{\mu_f P}{\Delta} = 2.18e+8\frac{N}{m} \end{aligned} \tag{B.76}$$

In order to assemble Mostaghel's hysteretic springs in a FE fashion, a finite element driver was implemented, which numerically integrates Eq. (B.73) for a given displacement increment by using a 4-th order Runge-Kutta scheme. Four Mostaghel's elements in parallel simulated the response of the CSB array -PS #2-.

2.1.6.4 Numerical model of a sliding liquid storage tank

In order to simulate the response of the liquid storage tank -NS #1-, the 3-DoFs linear model proposed by Malhotra and co-workers [28] was adopted. The model accounts for fluid-structure interaction in a simplified yet accurate manner. A schematic of the liquid storage tank model is illustrated in Fig. B.18. In detail, H and r define height and radius of the tank whilst h is the equivalent uniform thickness of the tank wall.

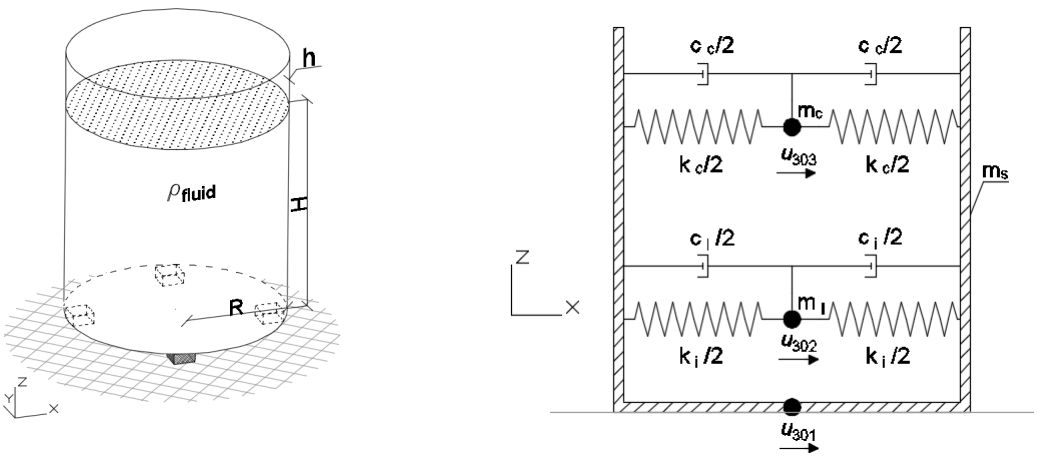

Fig. B.18. Sliding liquid storage tank according to [41]; a) schematic; b) numerical model with mass DoF numbering

As depicted in Fig. B.18, two S-DoF damped oscillators emulate impulsive and convective vibration modes of the sloshing fluid. In this regard, natural vibration periods T_i and T_c and masses m_i and m_c associated with impulsive and convective fluid oscillation modes are respectively calculated as,

$$T_i = C_i H\sqrt{\frac{\rho r}{Eh}}, T_c = C_c\sqrt{r} \tag{B.77}$$

$$m_i = \gamma_i m_l, m_c = \gamma_c m_l \tag{B.78}$$

where, ρ the mass density of liquid, E the modulus of elasticity of the tank material; C_i, C_c, γ and γ_c are four coefficients depending on the tank wall slenderness H/r; m_l is the total mass of the liquid. Values of stiffness parameters k_c and k_i were calibrated to match pre-selected target periods; convective and impulsive damping ratios, $\zeta_c = 0.5\%$ and $\zeta_i = 5\%$ respectively, determine the parameters of equivalent linear dashpots in the model.

$$k_i = m_i\left(\frac{2\pi}{T_i}\right)^2, k_c = m_c\left(\frac{2\pi}{T_c}\right)^2 \tag{B.79}$$

$$c_i = \frac{4\pi m_i \zeta_i}{T_i}, c_c = \frac{4\pi m_c \zeta_c}{T_c} \tag{B.80}$$

For the sake of completeness, mass, damping and stiffness matrices, needed to study the dynamic response of the liquid storage tank -NS #1-, are reported below,

$$\mathbf{M}^N = \begin{bmatrix} m_s & 0 & 0 \\ 0 & m_i & 0 \\ 0 & 0 & m_c \end{bmatrix}, \mathbf{C}^N = \begin{bmatrix} (c_i + c_c) & -c_i & -c_c \\ -c_i & c_i & 0 \\ -c_c & 0 & c_c \end{bmatrix}, \quad \mathbf{K}^N = \begin{bmatrix} (k_i + k_c) & -k_i & -k_c \\ -k_i & k_i & 0 \\ -k_c & 0 & k_c \end{bmatrix} \tag{B.81}$$

where $m_s = m_t + m_l - m_i - m_c$ is the residual sliding mass and m_t is the storage tank mass without liquid. Table B.8 reports all parameter values whilst Table B.9 summarizes the global parameters of the sloshing fluid model.

Table B.8 Parameters of the liquid storage tank model.

Parameter	Value	Unit
E	210	GPa
ρ_{fluid}	900	kg/m^3
ρ_{tank}	7850	kg/m^3
γ_c	0.1580	
γ_i	0.8320	
C_c	1.48	
C_i	7.03	
H	12	m
R	4	m
h	6e-3	m
m_t	28000	kg
m_l	5.43e5	kg
m_s	33200	kg

Table B.9 Global parameters of the sloshing fluid model.

Sloshing mode	Mass [kg]	Damping [Ns/m]	Stiffness [N/m]	Vibration period [s]	Damping ratio ζ
Convective	8.58e4 (m_c)	1.82e3 (c_c)	3.86e7 (k_c)	2.96 (T_c)	0.50 % (ζ_c)
Impulsive	4.52e5 (m_i)	1.99e6 (c_i)	8.77e10 (k_i)	0.14 (T_i)	5.00 % (ζ_i)

2.1.6.5 Simulation of the emulated system with the C-EDS method

In order to simulate the seismic response of the petrochemical prototype plant of Fig. B.11 a partitioned model of the emulated system was implemented in MATLAB [29]. In detail, all NS and PS models described in Subsections 1.2.6 were coupled together by using the LLMs within the C-EDS method. Fig. B.19 illustrates a sketch of the partitioned model with node numbering.

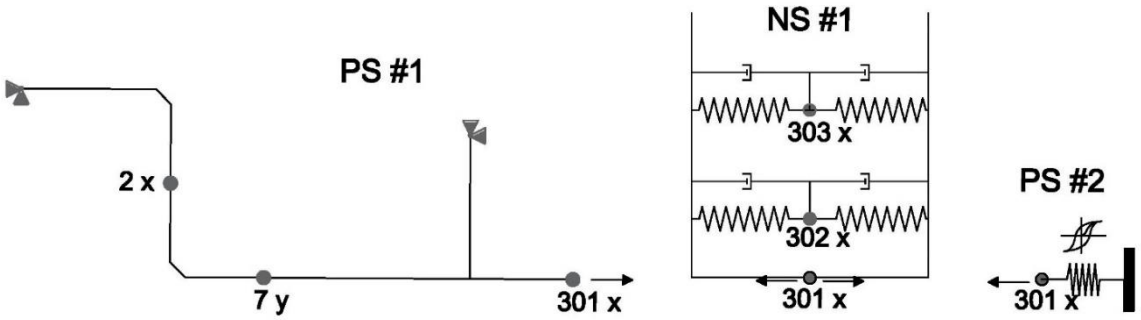

Fig. B.19. Partitioned model of the petrochemical prototype plant case study.

The time history response of the system was numerically obtained by considering a time integration step $\Delta t = 0.1\,\mathrm{ms}$ without subcycling $(ss = 1)$. In line with the goal of this virtual experiment, which aims at estimating the residual shift of the liquid storage tank, Fig. B.20 compares both displacement and velocity response histories relevant to Node 301, which is shared by all substructures, to a reference solution. The reference "exact" solution was calculated by Newmark method $(\Delta t = 0.1\,\mathrm{ms}, \gamma = 1/2, \beta = 1/4)$, considering a monolithic model of the prototype plant case study that merges the FE models of all substructures condensed to the same DoFs retained by the partitioned model of Fig. B.19.

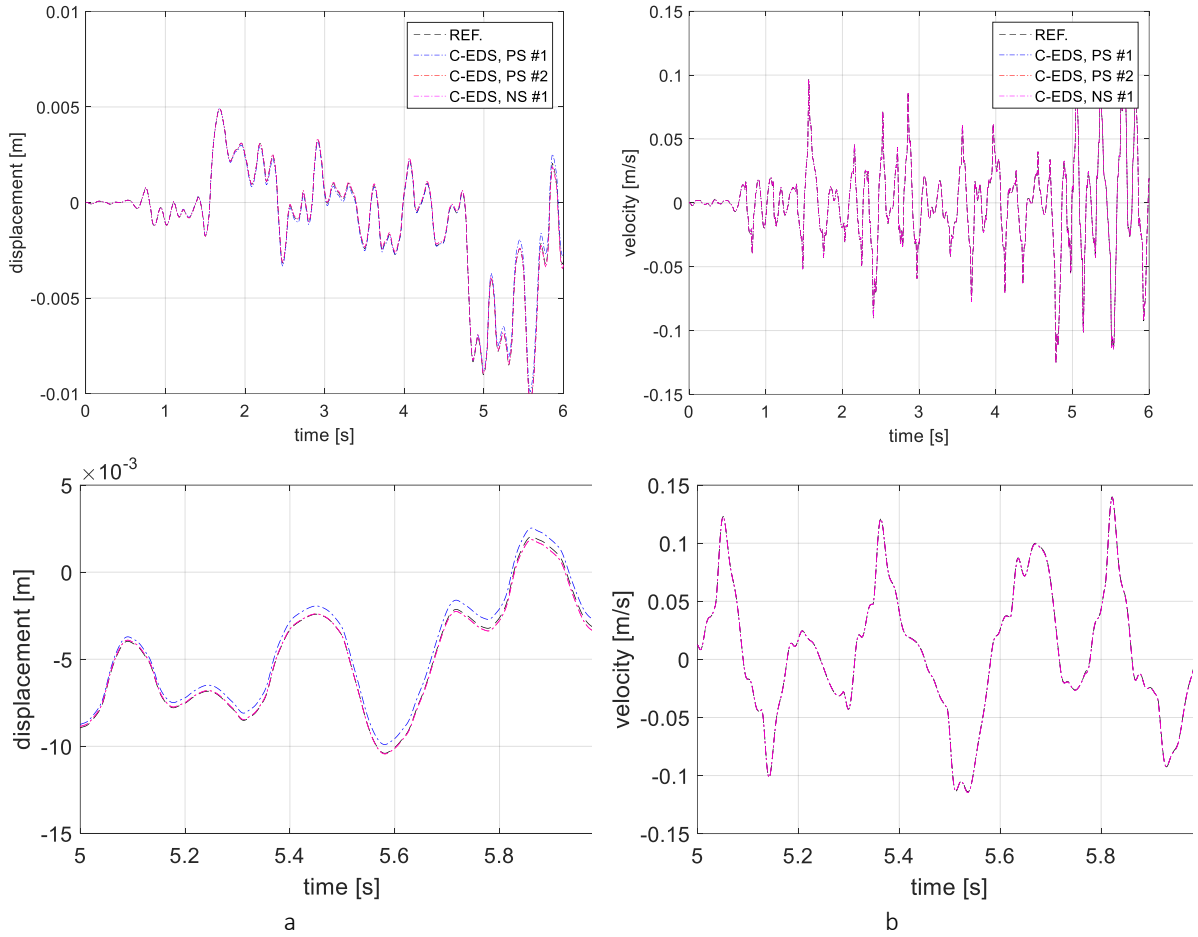

Fig. B.20. Time history responses of Node 301: a) displacement; b) velocity and relevant zoomed views.

As can be appreciated from Fig. B.20a, a small drift is observed among displacement histories corresponding to the same coupling DoF that belong to different subdomains. On the other hand, as illustrated in Fig. B.20b, interface velocity coupling ensures exact matching of velocity histories. Similarly, Fig. B.21 compares both force time history response and displacement-force hysteretic loop of the CSB array -PS #2-.

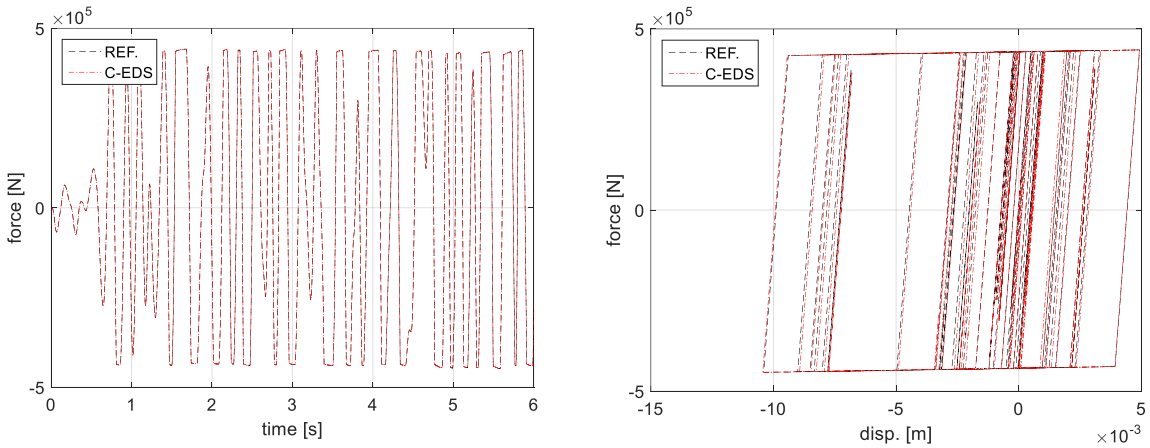

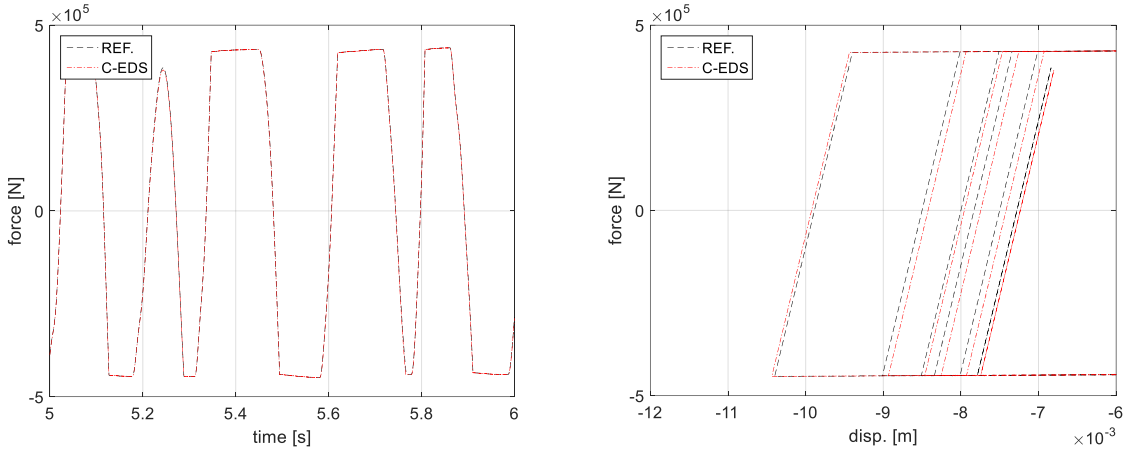

Fig. B.21. Dynamic response of the CSB array: a) force time history; b) displacement-force hysteretic loop and relevant zoomed views.

3 Thermomechanical coupled analysis for HDS: numerical studies

3.1 Numerical simulations of hybrid fire testing

Earthquakes are destructive and unpredictable events of nature with catastrophic consequences for both people and built environment. Secondary triggered effects can strike further an already weakened community, i.e. ground shaking, surface faults, landslides and tsunamis. In this respect, also fires following earthquake (FFE) are a considerable threat as they can be widespread both at the building level and at the regional level within the seismic affected area owing to the rupture of gas lines, failure of electrical systems etc. and at the same time failure of the compartmentation measures. Moreover, they are more difficult to tackle by the fire brigades because of their possible large number and extent as well as of possible disruptions within the infrastructural network that hinder their timely intervention and within the water supply system. In this context, the structural fire performance can worsen significantly because the fire acts on an already damaged structure. Furthermore, passive and active fire protections may have also been damaged by the seismic action and the fire can spread more rapidly if compartmentation measures have failed. Thus, the seismic performance of the non-structural components may directly affect the fire performance of the structural members. As consequence, the minimization of the non-structural damage is paramount in mitigating the possible drop in structural fire performance. The loss of fire protection is particularly dangerous for steel structures because the high thermal conductibility associated with small profile thicknesses entails quick temperature rise in the profiles with consequent fast loss of strength and stiffness.

Normally to study the behaviour of an element or a part of the building there are three approaches:

1. Numerical simulation of the structure: the real behaviour of the elements/structures may be very different.
2. Physical tests of the whole structure. However, large-scale structural fire tests are expensive and need specialized facilities.
3. Physical tests on single components subjected to standard heating curves or partial subassemblies: they offer significant information for the understanding of fire performance of specific structural elements, but they do not provide insight on the interaction between the fire development and the whole structure.

In order to overcome such limitations, Hybrid Simulation (HS), extensively investigated in the seismic domain, represents a tempting approach. The hybrid model of the prototype structural system combines numerical and physical substructures (NSs and PSs).

3.1.1 Description of the D2LAB framework and the RT-HFT method

ETH and University of Trento developed a MATLAB framework (D2LAB) [43] for finite element analyses (FEA) and partitioned analyses. It is an in-house finite element code and it is created to provide a robust framework for various types of finite elements that can be added to the library. The ability of this

framework to perform partitioned analyses represents a major advantage that cannot be found in other commercial software.

For the thermomechanical element inside the framework, a nonlinear method of frame analysis has been used which includes the effect of geometric nonlinearity, temperature-dependent nonlinear material behaviour and variation in temperature distribution both along and across the section. This method is based on large deformation theory (corotational formulation) under the assumption of small strains [55-56]. To discretize the section, 2 Gauss points along the element and 7 or 15 Gauss points in the section are used. The effects of thermal strains are also included and different values of the elastic stiffnesses of the support conditions can be considered. Deterioration in material strength and stiffness at increasing temperature is represented by a set of nonlinear stress-strain temperature relationships using two temperature dependent steel material functions, one has a bilinear stress-strain relationship and the other is defined according to Eurocode 3 stress-strain curve [46].

Structures subject to increasing loads or temperatures are analysed using an incremental Newton-Raphson iterative procedure. The analysis provides a complete load-deformation and temperature-deformation history for two-dimensional steel frames. At the beginning of each load step, the external loads are applied to the element of which nodal loads are directly applied and elemental load are transferred to equivalent fixed end force. Then the iterations are conducted by a solver following the predefined iterative procedures (Newton-Raphson) to derive convergence once the predefined error tolerance is satisfied.

D2LAB also uses RT-HFT methods that relies on the Gravouil and Combescure (GC) algorithm [16] and the Localized Lagrange Multipliers (LLM) method [44] to couple multiple PS and NS. A Dynamic relaxation (DR) algorithm [45] is adopted to build an equivalent dynamic system that mimic the static response of substructures. In order to maximize the convergence rate of DR, Component-mode synthesis (CMS) [57] is used to derive reduced-order matrices for both PS and NS thus minimizing the bandwidth of the emulated structure.

The idea behind the DR is to solve a static structural problem by computing the transient response of an equivalent dynamic system where mass and damping are fictitious.

$$\boldsymbol{M\ddot{u} + C\dot{u} + r(u) = f(t)} \tag{C.1}$$

In detail, M and C are diagonal matrices to maximize convergence rate of DR algorithm.

$$\boldsymbol{M_{ii} = \frac{(1.1\,\Delta t)^2}{4} \sum_j |K_{ij}|} \tag{C.2}$$

$$\boldsymbol{C_{ii} = 2\omega_0 M_{ii}} \tag{C.3}$$

The Newton algorithm with parameters $\gamma = 0.5$ and $\beta = 0$ is used to integrate Eq. C.1.

The LLM-GC algorithm form to integrate from t_k to t_{k+1} with a step time Δt reads:

$$\begin{cases} \begin{cases} \mathbf{M}^N \ddot{\boldsymbol{u}}_{k+1}^N + \mathbf{C}^N \dot{\boldsymbol{u}}_{k+1}^N + \mathbf{r}^N(\mathbf{u}_{k+1}^N, \boldsymbol{\theta}_{k+1}^N) = \mathbf{f}_{k+1}^N + \mathbf{L}^{N^T} \Lambda_{k+1}^N \\ \mathbf{L}^N \dot{\boldsymbol{u}}_{k+1}^N + \bar{\mathbf{L}}^N \dot{\boldsymbol{u}}_{k+1}^g = \mathbf{0} \end{cases} \\ \begin{cases} \mathbf{M}^P \ddot{\boldsymbol{u}}_{k+1}^P + \mathbf{C}^P \dot{\boldsymbol{u}}_{k+1}^P + \mathbf{r}^P(\mathbf{u}_{k+1}^P, \theta_{k+1}^P) = \mathbf{f}_{k+1}^P + \mathbf{L}^{P^T} \Lambda_{k+1}^P \\ \mathbf{L}^P \dot{\boldsymbol{u}}_{k+1}^P + \bar{\mathbf{L}}^P \dot{\boldsymbol{u}}_{k+1}^g = \mathbf{0} \end{cases} \\ \bar{\mathbf{L}}^{N^T} \Lambda_{k+1}^N + \bar{\mathbf{L}}^{P^T} \Lambda_{k+1}^P = \mathbf{0} \end{cases} \tag{C.4}$$

For the sake of simplicity this formula is presented for a single pair of PS and NS.

The method is summarized herein:

1. Solve the NS free problem at t_{k+1}

$$\begin{cases} \tilde{\boldsymbol{u}}_{k+1}^{N,free} = \mathbf{u}_k^N + \dot{\mathbf{u}}_k^N \Delta t + \left(\frac{1}{2} - \beta\right) \Delta t^2 \ddot{\mathbf{u}}_k^N \\ \tilde{\dot{\boldsymbol{u}}}_{k+1}^{N,free} = \dot{\mathbf{u}}_k^N + (1-\gamma)\Delta t \ddot{\mathbf{u}}_k^N \end{cases} \tag{C.5}$$

$$\ddot{\boldsymbol{u}}_{k+1}^{N,free} = \mathbf{D}^{N^{-1}} \left(\mathbf{f}_{k+1}^N - \mathbf{C}^N \tilde{\dot{\boldsymbol{u}}}_{k+1}^{N,free} - \mathbf{r}_{k+1}^N (\tilde{\boldsymbol{u}}_{k+1}^{N,free}) \right) \tag{C.6}$$

$$\begin{cases} \mathbf{u}_{k+1}^{N,free} = \tilde{\boldsymbol{u}}_{k+1}^N + \ddot{\boldsymbol{u}}_{k+1}^{N,free} \beta \Delta t^2 \\ \dot{\boldsymbol{u}}_{k+1}^{N,free} = \tilde{\dot{\boldsymbol{u}}}_{k+1}^N + \ddot{\boldsymbol{u}}_{k+1}^{N,free} \gamma \Delta t \end{cases} \tag{C.7}$$

where:

$$\mathbf{D}^N = \mathbf{M}^N + \mathbf{C}^N \gamma \Delta t + \mathbf{K}^N \beta \Delta t^2 \tag{C.8}$$

γ=0.5 and β=0 (according DR).

2. Solve the PS free problem at t_{k+1}

$$\begin{cases} \tilde{\boldsymbol{u}}_{k+1}^{P,free} = \mathbf{u}_k^P + \dot{\mathbf{u}}_k^P \Delta t + \left(\frac{1}{2} - \beta\right) \Delta t^2 \ddot{\mathbf{u}}_k^{P,free} \\ \tilde{\dot{\boldsymbol{u}}}_{k+1}^{P,free} = \dot{\mathbf{u}}_k^P + (1-\gamma)\Delta t \ddot{\mathbf{u}}_k^{P,free} \end{cases} \tag{C.9}$$

$$\ddot{\boldsymbol{u}}_{k+1}^{P,free} = \mathbf{D}^{P^{-1}} \left(\mathbf{f}_{k+1}^P - \mathbf{C}^P \tilde{\dot{\boldsymbol{u}}}_{k+1}^{P,free} - \mathbf{r}_{k+1}^N (\tilde{\boldsymbol{u}}_{k+1}^{P,free}) \right) \tag{C.10}$$

$$\begin{cases} \mathbf{u}_{k+1}^{P,free} = \tilde{\boldsymbol{u}}_{k+1}^{P,free} + \ddot{\boldsymbol{u}}_{k+1}^{P,free}\beta\Delta t^2 \\ \dot{\boldsymbol{u}}_{k+1}^{P,free} = \tilde{\dot{\boldsymbol{u}}}_{k+1}^{P,free} + \ddot{\boldsymbol{u}}_{k+1}^{P,free}\gamma\Delta t \end{cases} \tag{C.11}$$

where:

$$\mathbf{D}^P = \mathbf{M}^P + \mathbf{C}^P\gamma\Delta t + \mathbf{K}^P\beta\Delta t^2 \tag{C.12}$$

γ=0.5 and β=0 (according DR).

3. Calculation of interface Lagrange multiplier

$$\begin{bmatrix} \boldsymbol{\Lambda}_{k+1}^N \\ \boldsymbol{\Lambda}_{k+1}^P \\ \dot{\mathbf{u}}_{k+1} \end{bmatrix} = -\boldsymbol{G}^{-1} \begin{bmatrix} \boldsymbol{L}^N \dot{\mathbf{u}}_{k+1}^{N,free} \\ \boldsymbol{L}^P \dot{\mathbf{u}}_{k+1}^{P,free} \\ \mathbf{0} \end{bmatrix} \tag{C.13}$$

Where G is the Steklov-Poincarè operator and it is computed one based on the initial tangent stiffness of the substructure and inverted before the simulation starts.

4. Calculation of link accelerations

$$\begin{cases} \ddot{\boldsymbol{u}}_{k+1}^{N,link} = \mathbf{D}^N \mathbf{L}^{N^T} \Lambda_{k+1}^N \\ \dot{\boldsymbol{u}}_{k+1}^{P,link} = \mathbf{D}^P \mathbf{L}^{P^T} \Lambda_{k+1}^P \end{cases} \tag{C.14}$$

5. Calculation of coupled accelerations

$$\begin{cases} \ddot{\boldsymbol{u}}_{k+1}^N = \ddot{\boldsymbol{u}}_{k+1}^{N,free} + \ddot{\boldsymbol{u}}_{k+1}^{N,link} \\ \ddot{\boldsymbol{u}}_{k+1}^P = \ddot{\boldsymbol{u}}_{k+1}^{P,free} + \ddot{\boldsymbol{u}}_{k+1}^{P,link} \end{cases} \tag{C.15}$$

The block diagram of Figure (C.1) shows the architecture of the implementation of the LLM-GC algorithm [43].

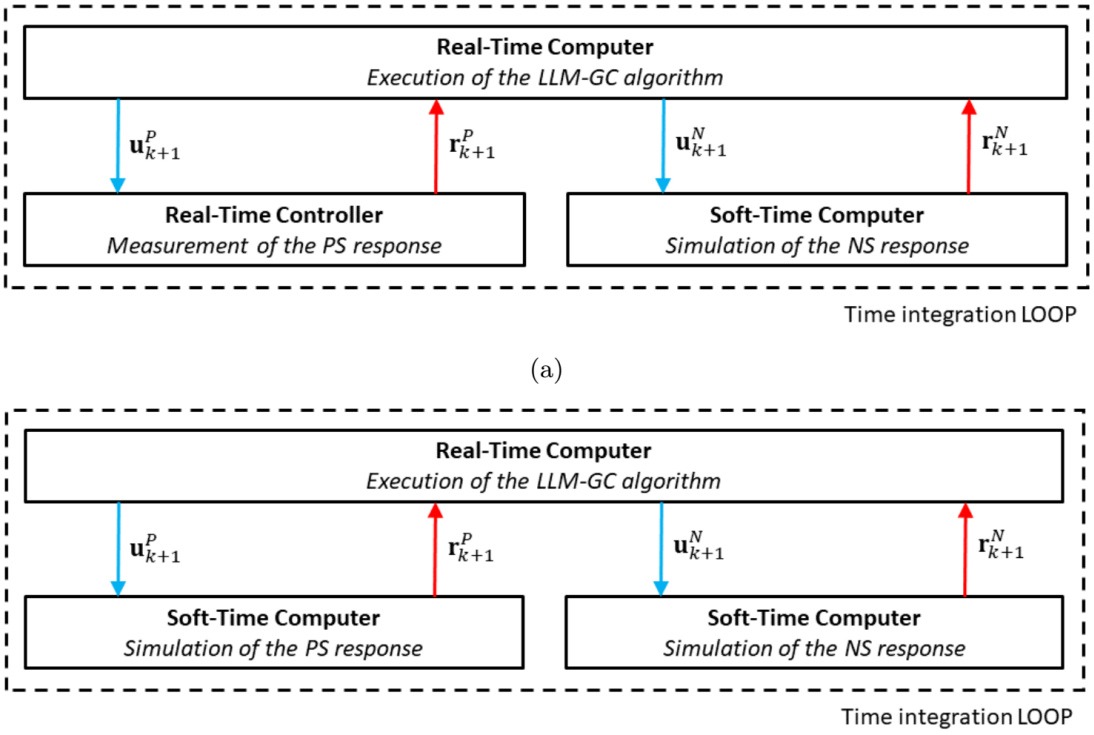

Figure C.1 Architecture of the HFT implementation of the LLM-GC algorithm: a) testing, b) rehearsal.

A real-time computer executes the LLM-GC algorithm that coordinates PS and NS. A real-time control system manipulates PS displacements and measures corresponding restoring forces while a soft-time computer computes the NS restoring force. The LLM-GC algorithm simplifies the coordination of multiple substructures and facilitate the reuse of existing structural analysis codes. In addition, test rehearsal can be easily performed by replacing the PS with a corresponding computational simulator.

3.1.2 Virtual real time hybrid fire test

In order to demonstrate the effectiveness of the framework with the RT-HFT method [43] and to illustrate the implementation of a real test, a virtual HFT campaign was conceived for a steel moment-resisting frame where both NS and PS were simulated numerically in MATLAB™ [29]. Results are verified against SAFIR™ [47] (FE software for the analysis of structures in fire) and ABAQUS™ [48].

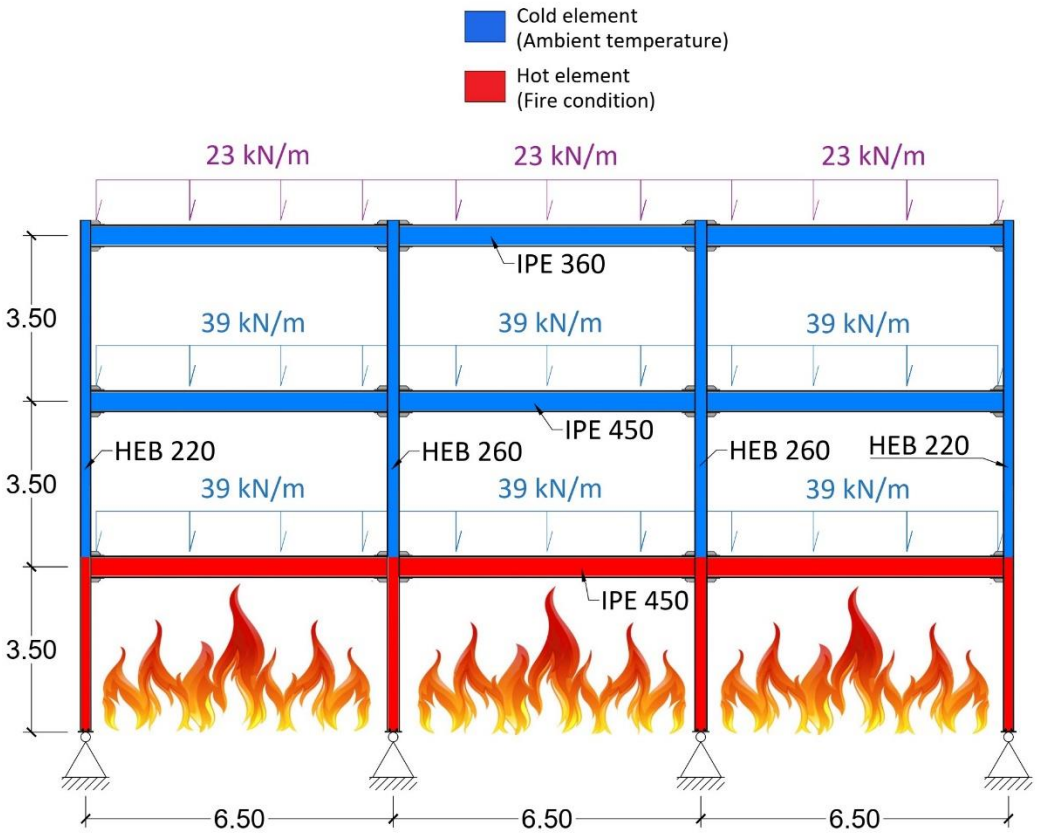

Figure C.2 Prototype structure: emulated moment-resisting frame

The three-storey three-bay moment-resisting frame [49, 43] reported in Fig. C.2 was selected as case study for the virtual HFT campaign. It is designed according to the Eurocode 3 considering a S235 steel grade. All beams and columns are characterized by standard commercial metric cross-section without any fire protection.

As show in Fig. C.2, only ground floor columns and first-storey beams are subjected to fire loading whilst the upper part of the frame remains at ambient temperature.

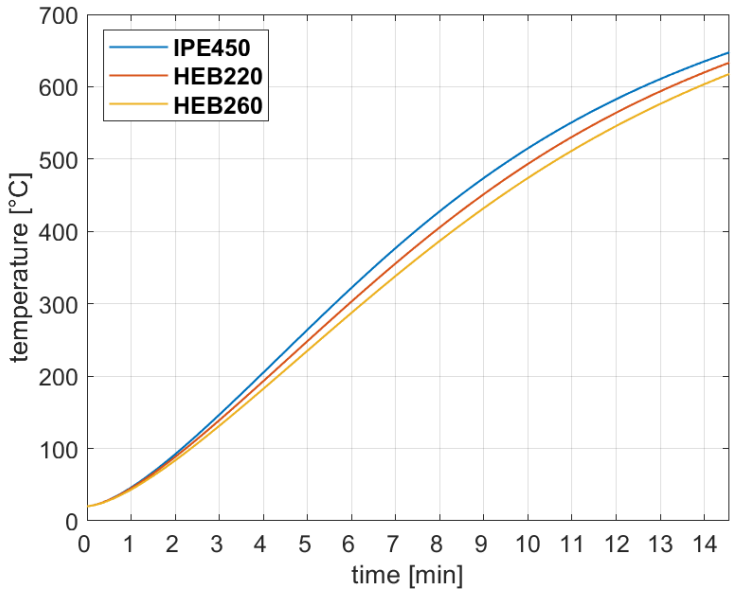

Figure C.3 time-temperature heating curves

This frame was partitioned into a NS and a PS as depicted in this figure.

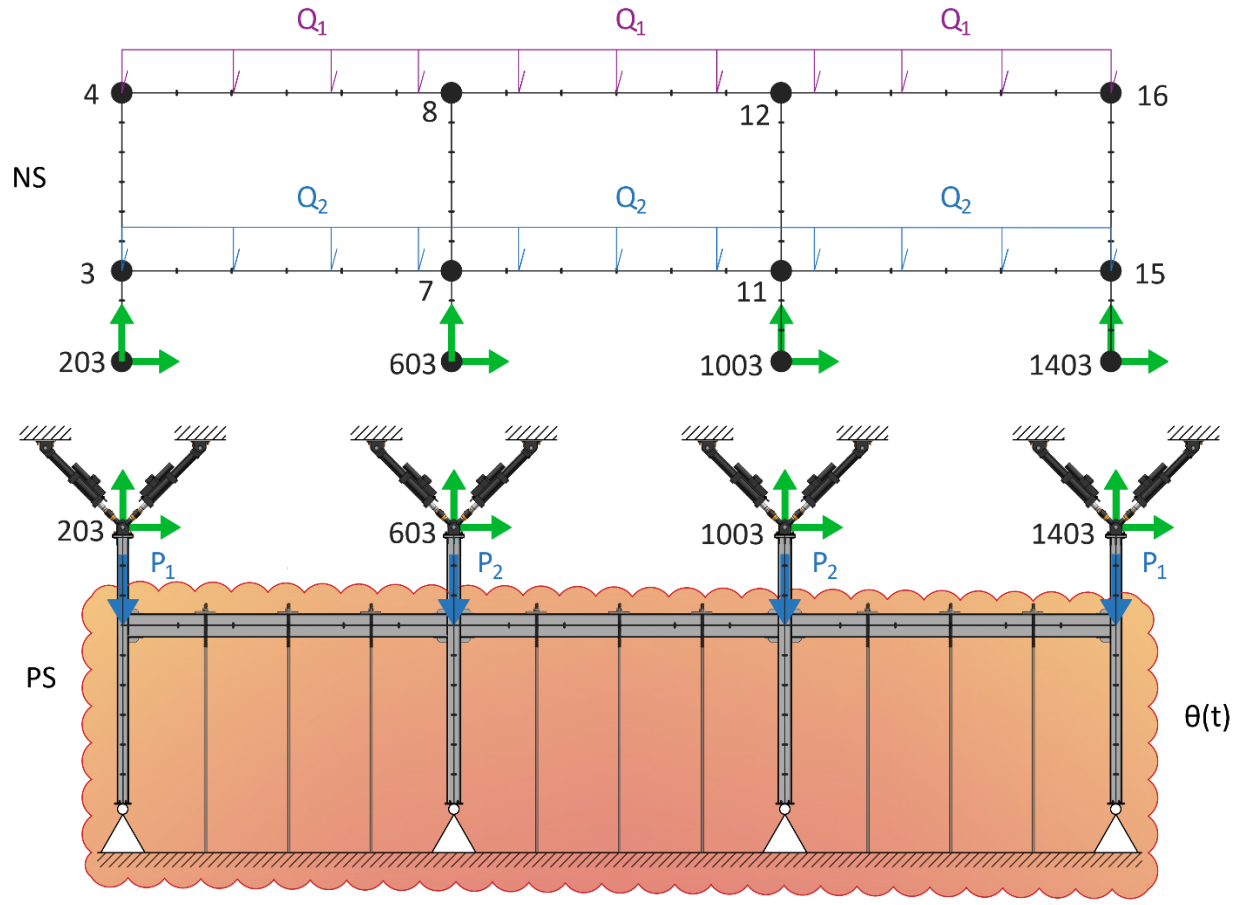

Figure C.4 Substructuring of the virtual moment-resisting frame: NS and PS.

As show in Fig. C.4 and Fig. C.5, we decided couple PS and NS at translational DoFs whilst continuity of rotational DoFs was neglected. This assumption was verified by nonlinear FE analyses of the frame response performed in SAFIR™.

The cold NS is linear elastic and each member is subdivided into six Bernoulli beam elements.

In order to reduce the frequency bandwidth of the NS, which deteriorates the convergence rate of the RT-HFT-FETI method, CMS was applied to condense NS matrices to the translational DoFs of the nodes numbered on this picture.

Since the HFT campaign is virtual, a refined nonlinear FE model was used to evaluate the response of the hot PS. Each member of the FE model is subdivided into six nonlinear thermomechanical beam elements endowed with material and geometric nonlinearities.

The history response of the steel moment resisting frame computed with the RT-HFT method is verified against the response of a reference monolithic FE model implemented in SAFIR™ and ABAQUS™.

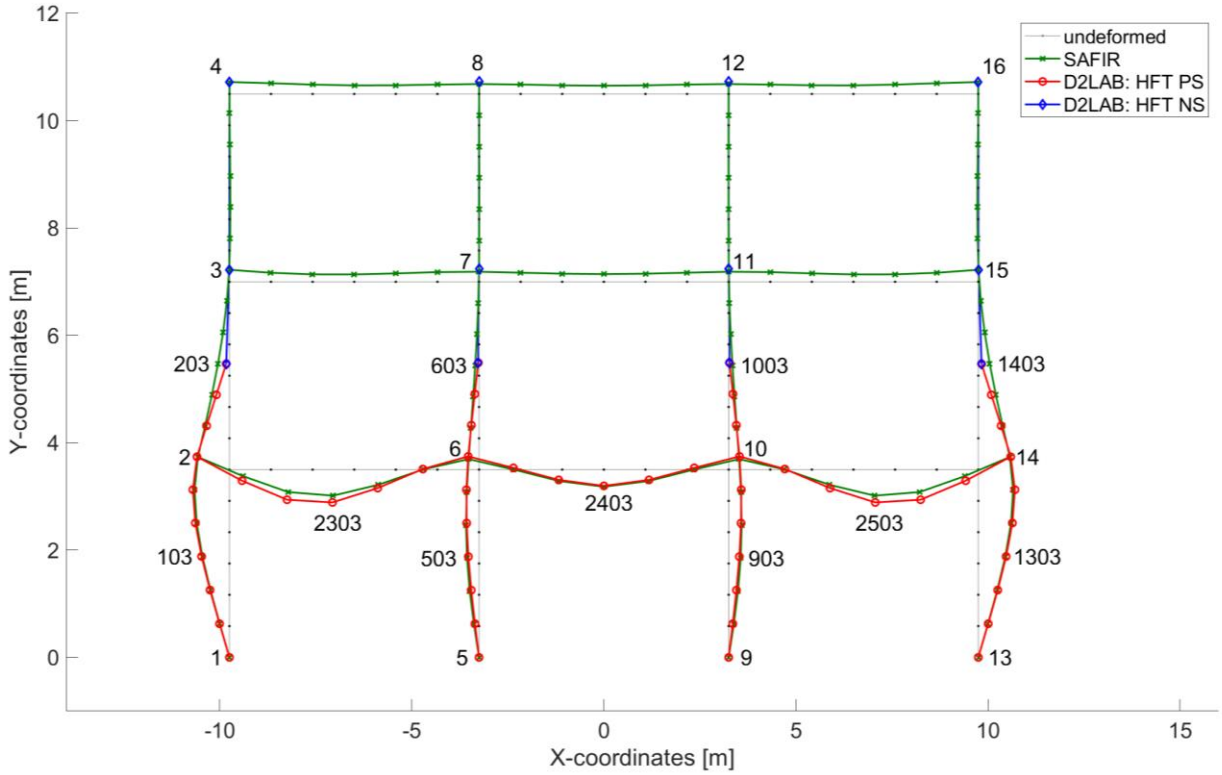

Figure C.5 Displacement comparison

Fig. C.5 compares the final deformed configuration of the moment-resisting frame at the end of the simulation (time=875 s). As can be appreciated, the static response of the frame obtained via HFT well matches the reference SAFIR™ solution. However, in order to represent the real case, continuity of rotation was enforced at the interface between PS and NS. For this reason, some discrepancies in the results were noticed. As expected, the location of the hinge at the column mid-height of the second floor was a good approximation at the beginning of the fire and during its first phases. However, as the fire progressed and the loss of strength and stiffness of the heated elements became significant, the load redistribution determined a variation of the bending moment diagram that was not compatible with the choice of the hinge at mid-level anymore.

Along the same line, Fig. C.7a and Fig. C.8a compare the horizontal displacement responses measured at Nodes 103 and 503, corresponding to the lateral responses of the first and the second columns of the PS measured at the mid-level. Analogously, Fig. C.9b and Fig. C10.b compare the vertical displacement responses of Nodes 2303 and 2403, which correspond to the central deflection of the first and the second beam of the PS.

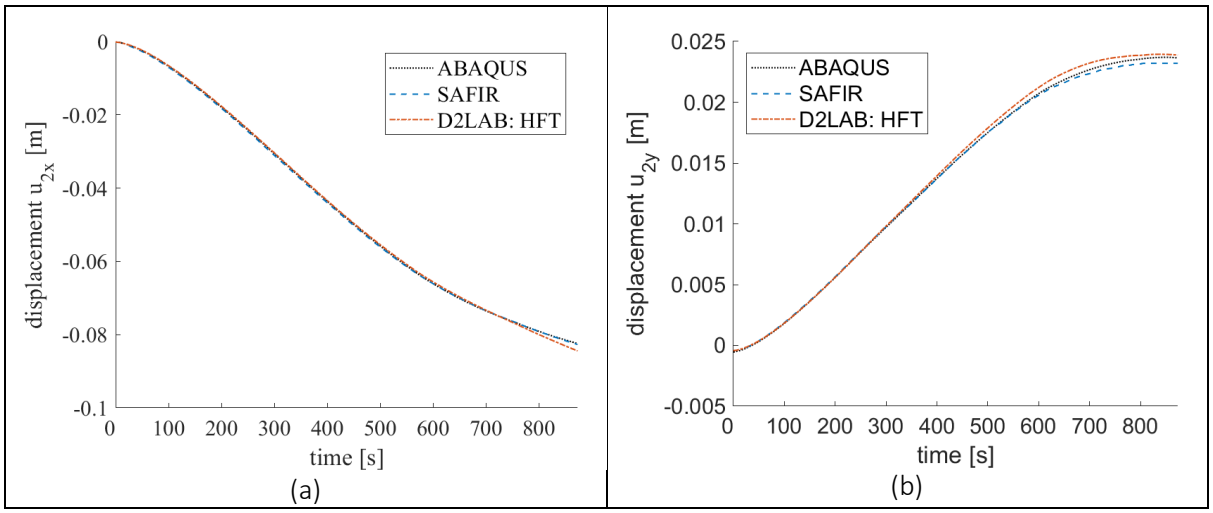

Figure C.6 Comparison of the horizontal(a) and vertical (b) displacement histories measured at node 2

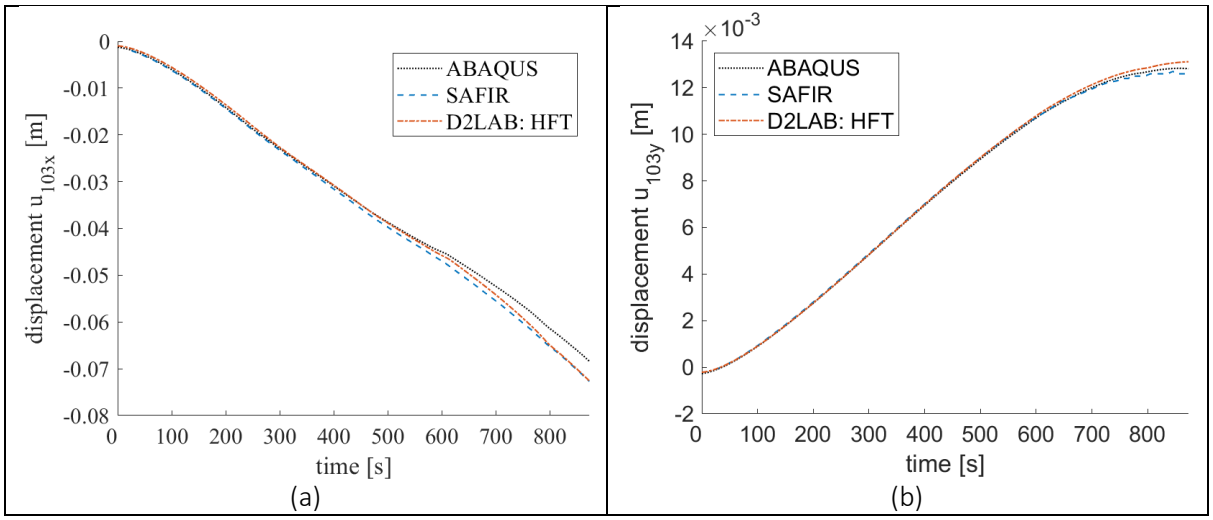

Figure C.7 Comparison of the horizontal (a) and vertical (b) displacement histories measured at node 103

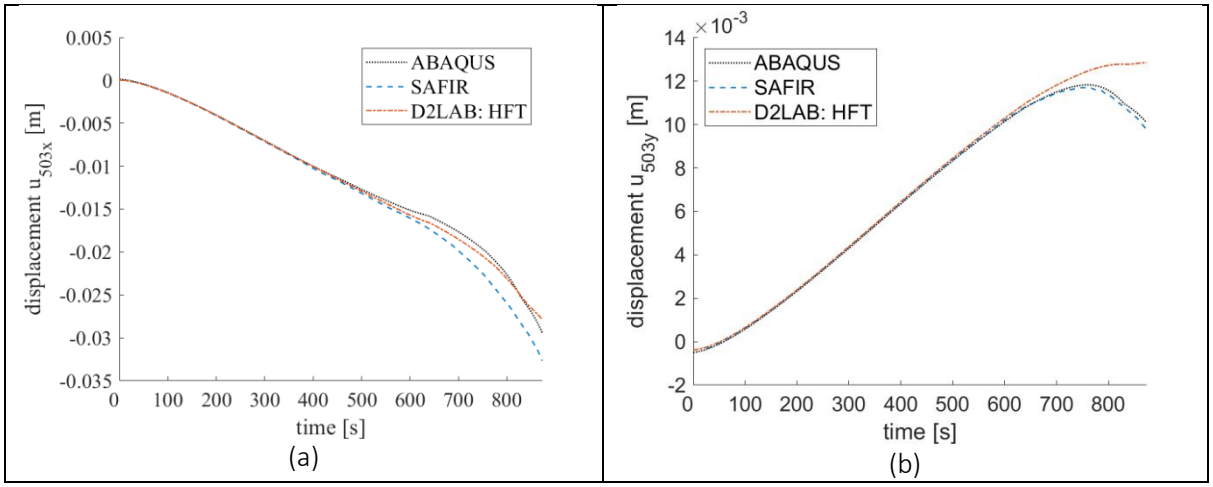

Figure C.8 Comparison of the horizontal (a) and vertical (b) displacement histories measured at node 503

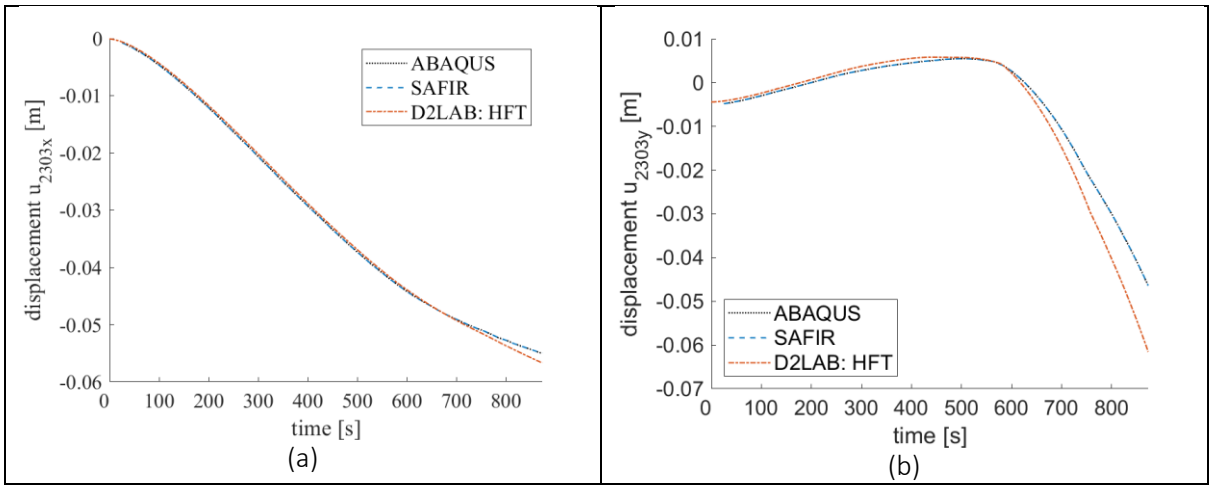

Figure C.9 Comparison of the horizontal (a) and vertical (b) displacement histories measured at node 2303

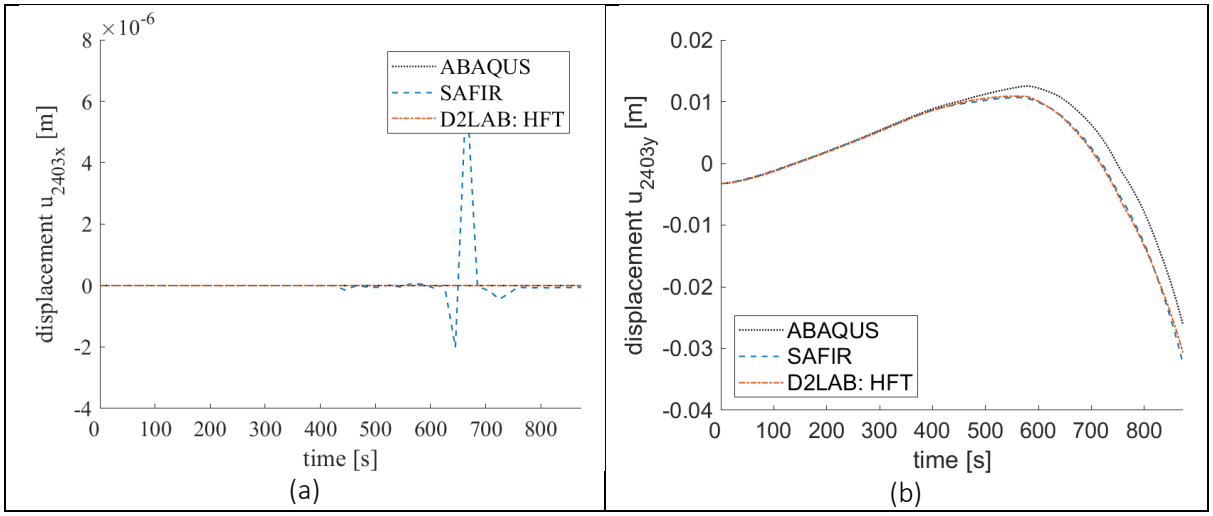

Figure C.10 Comparison of the horizontal (a) and vertical (b) displacement histories measured at node 2403

4 Reduction of epistemic uncertainties in hybrid simulations

4.1 Reducing ergodic seismic uncertainty: artificial accelerograms

Seismic risk evaluation of coupled systems of industrial plants often needs the implementation of complex finite element models able to take into account their multicomponent nature and the relevant coupling effects. These models typically rely on an extensive consumption of computational resources. Moreover, the relationships between seismic action, system response and relevant damage levels are often characterized by a high level of nonlinearity, thus requiring a solid background of experimental data. Furthermore, both fragility and reliability analyses depend on the adoption of a significant number of seismic waveforms. As a matter of fact, the variability of the seismic action and its characterization by a generic intensity measure (IM) are a source of uncertainty and error in fragility analyses. Nevertheless, these intensity variables (Der Kiureghan, 2005) are ergodic, i.e. statistically independent in the time domain, and, for this reason, the more samples are used, e.g. more seismic waveforms, the more accuracy will be obtained.

However, while it is possible to lower the uncertainty of seismic input by studying a large set of accelerograms, the availability of natural records is clearly limited. For this reason, with the aim of adopting a number of seismic signals higher than the available set of coherent natural accelerograms, we decided to use artificial ones. In detail we implemented a multi-step procedure to calibrate a stochastic ground motion model and generate coherent artificial seismic signals.

The first step of this procedure is performing a probabilistic seismic hazard analyses (PSHA), Cornell (1968) and Baker (2017), of a hypothetical geographical location where or case study would be located, i.e. Hanford in California (US). We relied on the United States Geological Survey (USGS) database and the relevant PSHA results are depicted in Fig. D.1 and D.2.

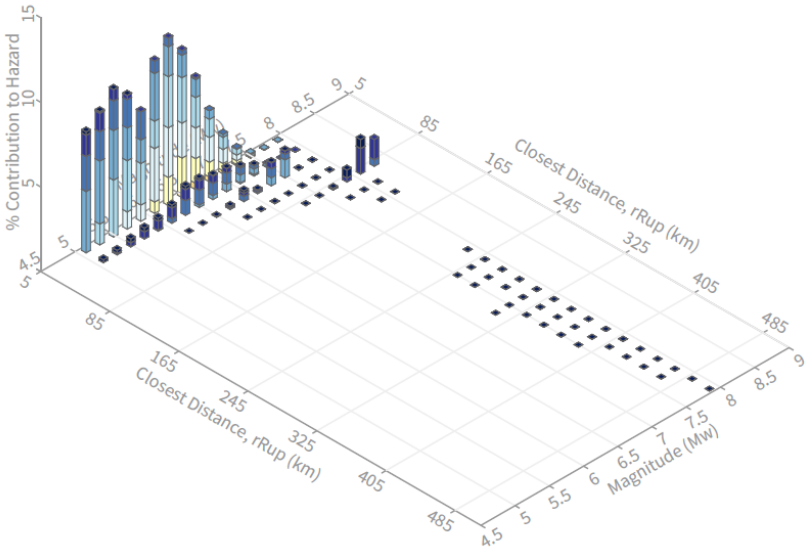

Fig. D.1: Probabilistic seismic hazard deaggregation analysis for Hanford, California (US).

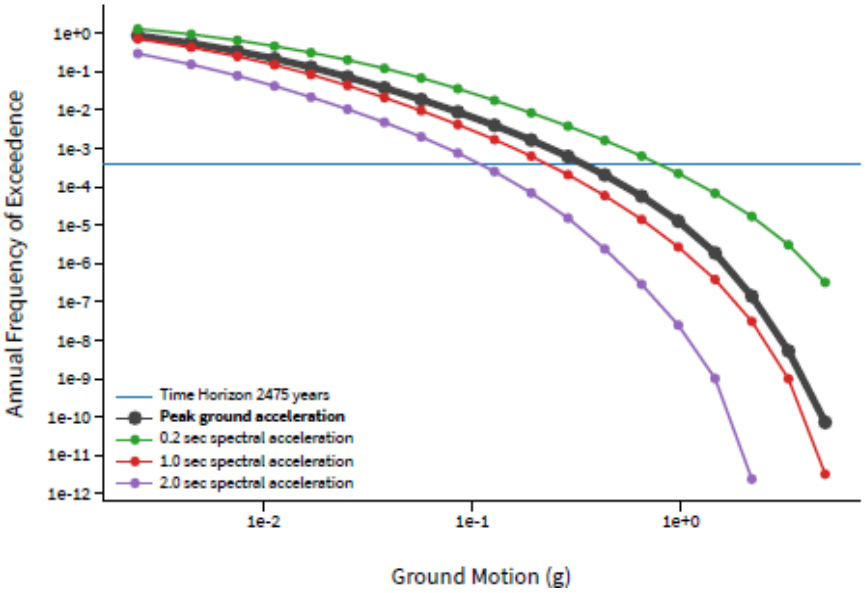

Fig. D.2: PSHA for Hanford, California (US).

From the deaggregation analysis, see Fig. D.1, we obtain a mode value for magnitude (M) and distance from the fault (R) equal respectively to 6.3 and 10.75 km. Based on these two values, a set of 7 compatible accelerograms is selected, as reported in Table 1.

Table D.1: Set of compatible accelerograms.

Earthquake Name	Year	Station Name	Magnitude	Distance (km)
"Northridge-01"	1994	"Canoga Park - Topanga Can"	6.69	14.7
"Northridge-01"	1994	"Canyon Country - W Lost Cany"	6.69	12.44
"Northridge-01"	1994	"N Hollywood - Coldwater Can"	6.69	12.51
"Northridge-01"	1994	"Northridge - 17645 Saticoy St"	6.69	12.09
"Northridge-01"	1994	"Simi Valley - Katherine Rd"	6.69	13.42
"Northridge-01"	1994	"Sun Valley - Roscoe Blvd"	6.69	10.05
"Northridge-01"	1994	"Sunland - Mt Gleason Ave"	6.69	13.35
"Northridge-02"	1994	"Pacoima Kagel Canyon"	6.05	11.34

As it is possible to notice from Table D.1, all the different signals are related to the same event, i.e. Northridge earthquake. Though this earthquake is clearly compatible with the geographical location, we decide to rely on a single event in order to limit the variability of the calibration input. In fact, the stochastic ground motion model, that we choose to calibrate based on these seismic signals, is already capable of taking into account a sufficient level of variability. In detail, the model was developed by Razaeian and Der Kiureghian (2010) and generates artificial waveforms from 6 different parameters, listed in Table D.2, by means of the following expression:

$$a_g(t) = q(t, \boldsymbol{\alpha}) \left[\frac{1}{\sigma_f(t)} \int_{-\infty}^{t} h\big(t - \tau, \boldsymbol{\lambda}(\tau)\big) \omega(\tau) d\tau \right] \tag{D.1}$$

Table D.2: Stochastic ground motion model parameters.

I_a	Arias intensity
$D_{5\text{-}95}$	Time interval of 95% of the I_a
t_{mid}	Time at which 45% of the I_a is reached
ω_{mid}	Filter frequency at t_{mid}
ω'	Rate of change of the filter frequency with time
ζ_f,	Filter damping ratio (constant).

Eq. (D.1) can be considered as the combination of three different factors, being the first of them $(t, \boldsymbol{\alpha})$, i.e. the time modulating function (TMF), given as following:

$$\begin{cases} q(t,\boldsymbol{\alpha}) = 0 & if\ t \le 0 \\ q(t,\boldsymbol{\alpha}) = \alpha_1 t^{\alpha_2 - 1} exp(-\alpha_3 t) & if\ t < 0 \end{cases} \tag{D.2}$$

where $\hat{\boldsymbol{\alpha}}$ is defined by means of:

$$\hat{\boldsymbol{\alpha}} = arg \min_{\boldsymbol{\alpha}} \left(\left| I_a(t_{45}) - \hat{I}_a(t_{45}) \right| + \left| I_a(t_{95}) - \hat{I}_a(t_{95}) \right| \right) \tag{D.3}$$

with:

$I_a(t) = \frac{\pi}{2g} \int_0^t a_g^2(\tau) d\tau$: Arias intensity of the real record (D.4)

$\hat{I}_a(t) = \frac{\pi}{2g} \int_0^t q^2(t, \boldsymbol{\alpha}) d\tau$: Arias intensity from the time modulating function (D.5)

The second factor in Eq. D.1 is $h\big(t - \tau, \boldsymbol{\lambda}(\tau)\big)$, i.e. the Impulse Response Function (IRF) of a linear time-varying filter, expressed as follows:

$$\begin{cases} h\big(t-\tau, \boldsymbol{\lambda}(\tau)\big) = \dfrac{\omega_f(\tau)}{\sqrt{1-\zeta_f^2(\tau)}} exp\big[-\zeta_f(\tau)\omega_f(\tau)(t-\tau)\big] sin\left[\omega_f(\tau)(t-\tau)\sqrt{1-\zeta_f^2(\tau)}\right] & if\ \tau \le t \\ h\big(t-\tau, \boldsymbol{\lambda}(\tau)\big) = 0 & if\ \tau > t \end{cases} \tag{D.6}$$

where:

$$\omega_f = \omega_{mid} + \omega'(t - t_{mid}) \tag{D.7}$$

Eq. (D.6) can also be used to compute $\sigma_f(t)$, by means of:

$$\sigma_f^2(t) = 2\pi S \int_{-\infty}^{t} h^2\big(t-\tau, \boldsymbol{\lambda}(\tau)\big) d\tau \tag{D.8}$$

The last of the three factors, (τ) , is the baseline noise. It is possible to notice that the parameters listed in Table D.2 influence both the TMF and the IRF while $\omega(\tau)$ is only affected by the baseline noise variability.

Following the calibration process described by Razaeian and Der Kiureghian (2010), we evaluate the model parameters able to generate a set of accelerograms similar to those listed in Table D.1. Once we get these values we make two hypotheses in order to define a statistical distribution for each of the model parameters. The first hypothesis is considering the parameters as statistically uncorrelated. With reference to this, the actual linear correlations between the different parameters are shown in Fig. D.3. The second hypothesis is the choice of uniform distributions to describe the probability distribution of all the parameters, with the only exception of ω' that we consider constant with a value of -0.568 rad/s^2. Regarding the uniformly distributed parameters, their lowest and highest boundaries, set to encompasses all the values from the aforementioned calibration process, are showed in Table D.3.

Table D.3: Distributions of stochastic parameters

Name	Distribution	LB	UB	Units
I_a	Uniform	0.019	3.992	m^2/s^3
D_{5-95}	Uniform	5.083	16.810	s
T_{45}	Uniform	1.596	5.664	s
ω_{mid}	Uniform	14.620	31.000	rad/s
ζ	Uniform	0.074	0.557	-

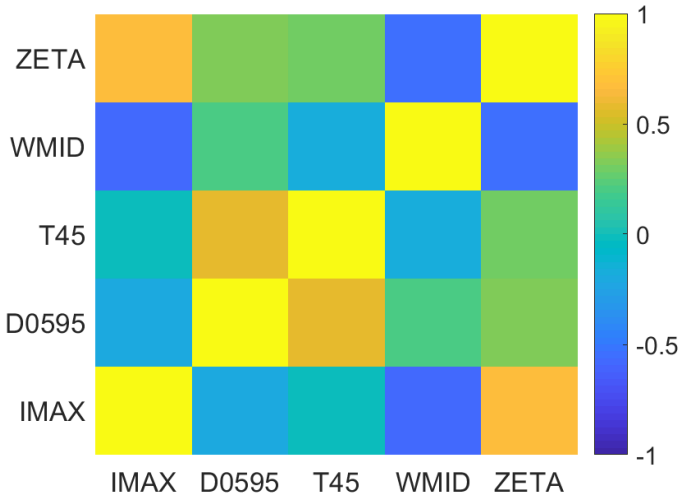

Fig. D.3: Linear correlation of stochastic parameters.

It is worthwhile to notice from Table D.3 that the degree of variability among the different parameters is not similar at all, while I_a and ζ exhibit wide distributions, the other three parameters are encompassed in a narrower range of values. Moreover, as shown in Fig. D.3, the hypothesis of uncorrelated parameters is not so far from the actual reality. Finally, with the aforementioned

parameters distributions and the model represented in the Eq. D.1, we are able to generate artificial accelerograms coherent with the seismic hazard characteristics of our geographical site.

4.2 Seismic fragility assessment of a tank-piping system based on hybrid simulation and surrogate modelling

The artificial seismic input introduced in section 2.1.1 is adopted to perform a fragility analysis of a realistic unanchored tank-piping system, as depicted in Fig. D.4. The fragility analysis is focused on LOC events from vulnerable piping components like pipe elbows, see in this respect Bursi et al, 2018. This analysis is achieved with a numerical Kriging surrogate model calibrated with FEMs and experimental results. In particular, this surrogate model is able to evaluate the seismic response of the tank-piping system based on the stochastics ground motion model parameters discussed in section 2.1.1.

The experimental tests are performed by means of hybrid simulations, with a numerical substructure (NS), i.e. the unanchored tank, replaced by a MTS actuator and a physical substructure, i.e. the piping network. The numerical substructure of the hybrid simulator (HS) is modelled with a simplified model based on Malhotra et al., 2000, as shown in Fig. D.5 while the relevant parameters are reported in Table D.4. For reference, the main scheme of HS is shown in Fig. D.6.

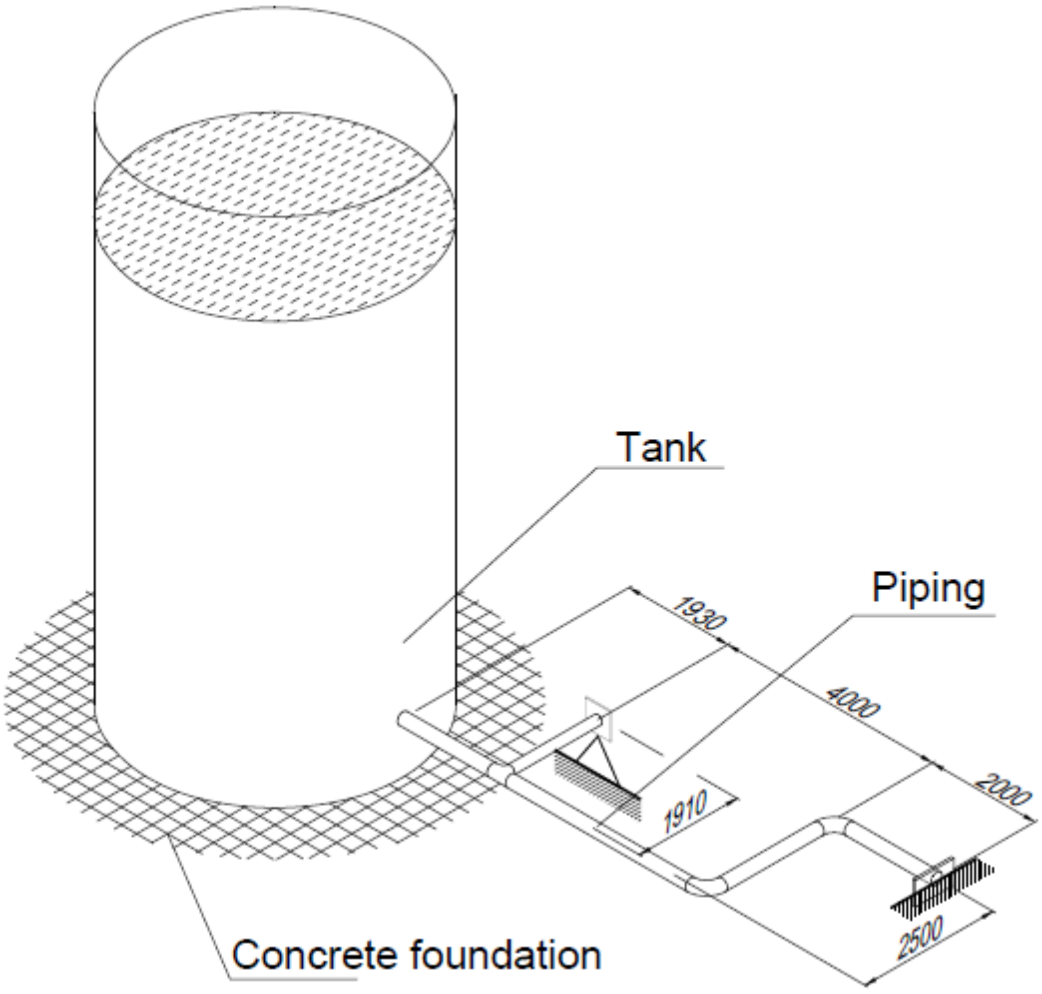

Fig. D.4: Realistic tank-piping system, measures in mm.

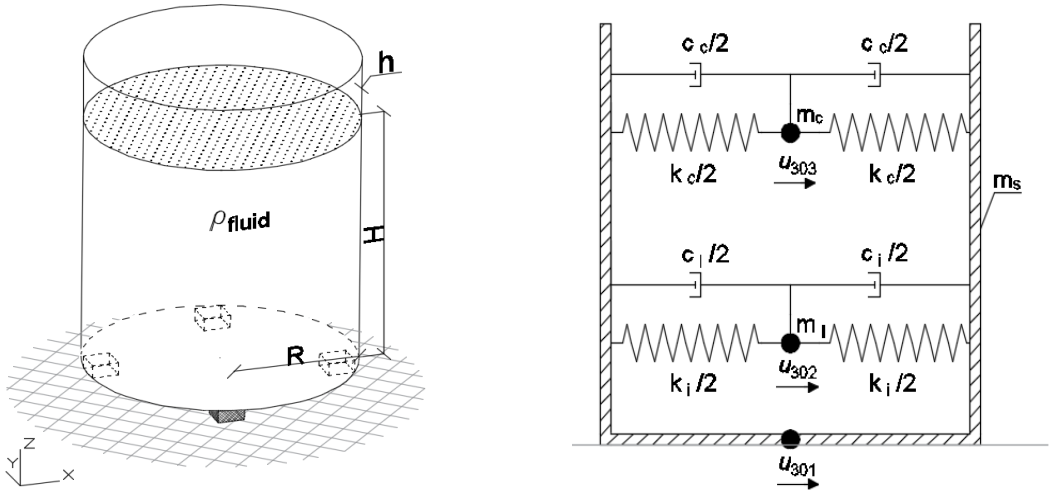

Fig. D.5: Simplified tank model after Malhotra et al., 2000.

Table D.4: Simplified tank model parameters.

Parameter	Value	Unit
E	210	GPa
ρ_{fluid}	900	kg/m3
ρ_{tank}	7850	kg/m3
c_c	1.69e3	Ns/m
c_i	1.93e6	Ns/m
H	14	m
R	4	m
m_t – steel tank mass	1.65e4	kg
m_l – liquid mass	6.33e5	kg
m_c – convective mass	7.98e+4	kg
m_i – impulsive mass	5.47e+5	kg

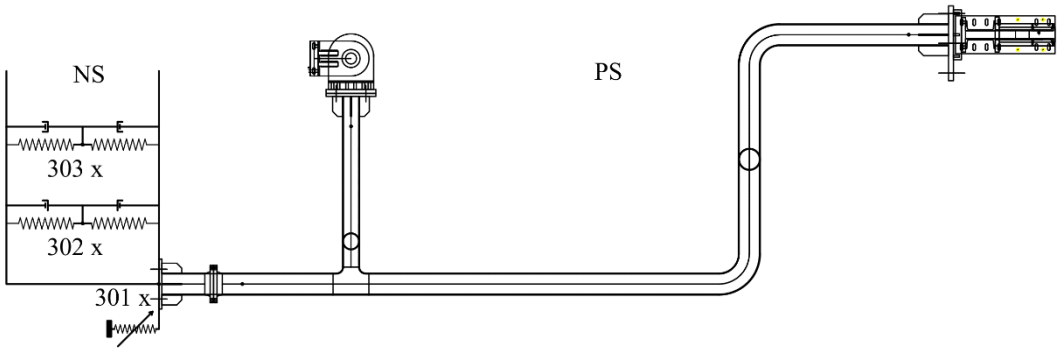

Fig. D.6: Hybrid simulator scheme.

Furthermore, the sliding effect at the base of the tank is set to replicate the friction interaction between the tank steel bottom and a concrete foundation. In detail, this effect is implemented into the NS trough a static friction model analytically described by a non-linear hysteretic model after Mostaghel, 1999. The model is shown in Fig. D.7 while its analytical formulation follows:

$$\begin{cases} \dot{r} = \left(\alpha_{MST} k_{MST} + (1-\alpha_{MST}) k_{MST} \left(\bar{N}(v)\bar{M}(s-\delta_{MST}) + M(v)N(s+\delta_{MST})\right)\right) v \\ \dot{u} = v \end{cases} \tag{D.9}$$

with,

$$s = \frac{r - \alpha_{MST} k_{MST} u}{(1-\alpha_{MST}) k_{MST}} \tag{D.10}$$

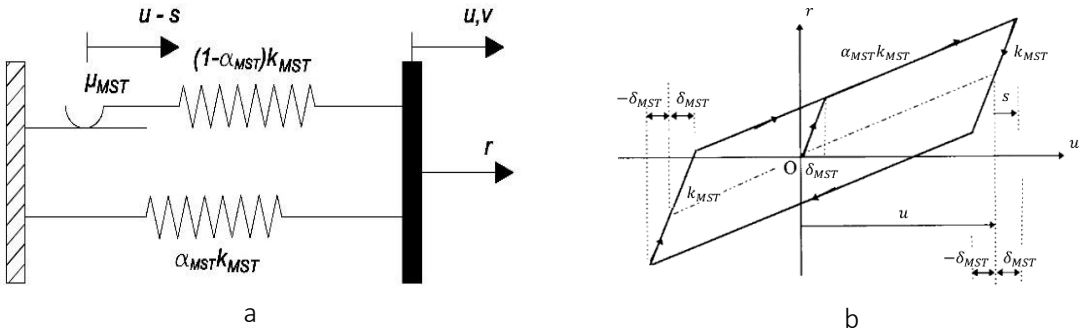

a b

Fig. D.7: Bilinear Mostaghel model: a) S-DoF idealization; b) Hysteretic loop.

The remaining functions $N, M, \bar{N}$ and $\bar{M}$ read,

$$\begin{aligned} N(v) &= 0.5\left(1 + sgn(v)\right)\left(1 + \left(1 - sgn(v)\right)\right) \\ M(v) &= 1 - N(v) \\ \bar{N}(v) &= M(-v) \\ \bar{M}(v) &+ N(-v) \end{aligned} \tag{D.11}$$

where $sgn(\cdot)$ is the sign function.

Specifically, we made the hypothesis of a static friction coefficient for the interaction steel-concrete equal to $\mu = 0.1$ after Gorst et al., 2002. The parameters k_{MST}, α_{MST} and δ_{MST} represent initial stiffness, post-yielding stiffness reduction factor and yielding displacement of the idealized spring system. These parameters are set in order to replicate the static friction phenomenon as follows:

$$\begin{gathered} \delta_{MST} = \Delta = 1e-3\ m \\ \alpha_{MST} = 1e-3 \\ k_{MST} = \frac{\mu(m_l + m_t)g}{\Delta} = 2.18e+8\frac{N}{m} \end{gathered} \tag{D.12}$$

With reference to the PS, the piping network consists of 8” (outer diameter: 219.08mm; thickness: 8.18mm) and 6” (outer diameter: 168.28mm; thickness: 7.11mm) schedule 40 straight pipes and contains several critical components, i.e. two elbows, a bolted flange joint and a Tee-joint. In this respect, see Fig. D.8 and D.9. Moreover, the piping network is filled with water at a pressure of 15 bar.

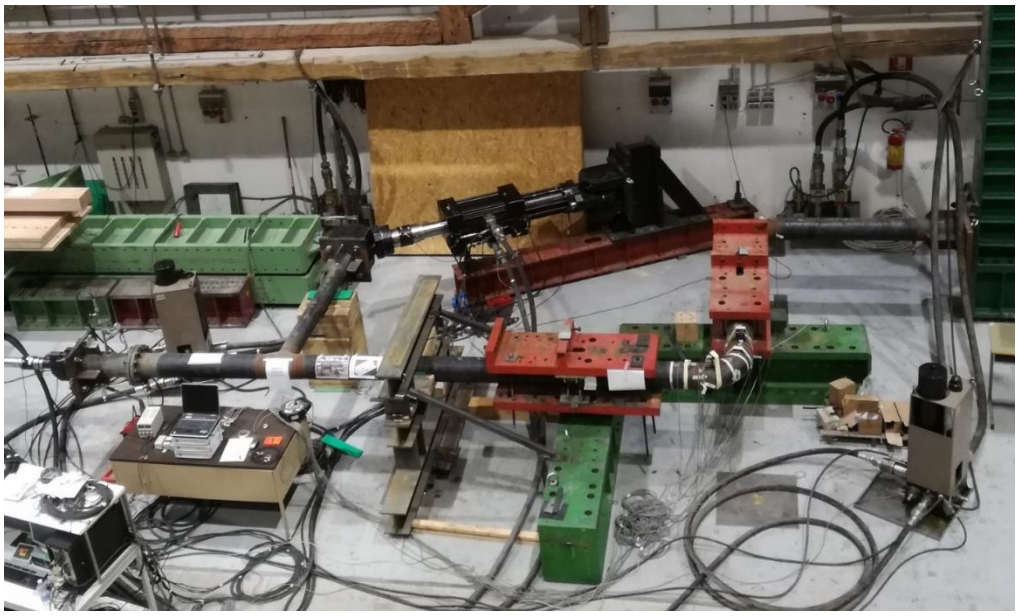

Fig. D.8: Experimental setup, physical substructure of hybrid simulator.

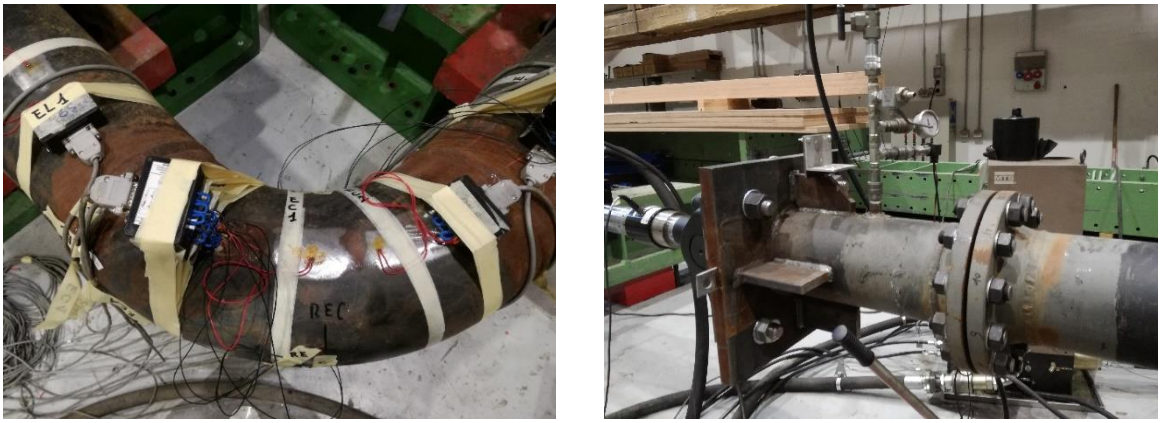

a) b)

Fig. D.9: a) piping elbow, b) bolted flange joint.

A set of different sensors, specifically strain gauges (SGs) and linear transducers (LVDTs), is placed on the experimental setup. In detail, three SGs are positioned on both the elbows in order to detect hoop strain levels, while four LVDTs are placed on the first of the two elbows. With respect to this see Fig. D.10 for additional details.

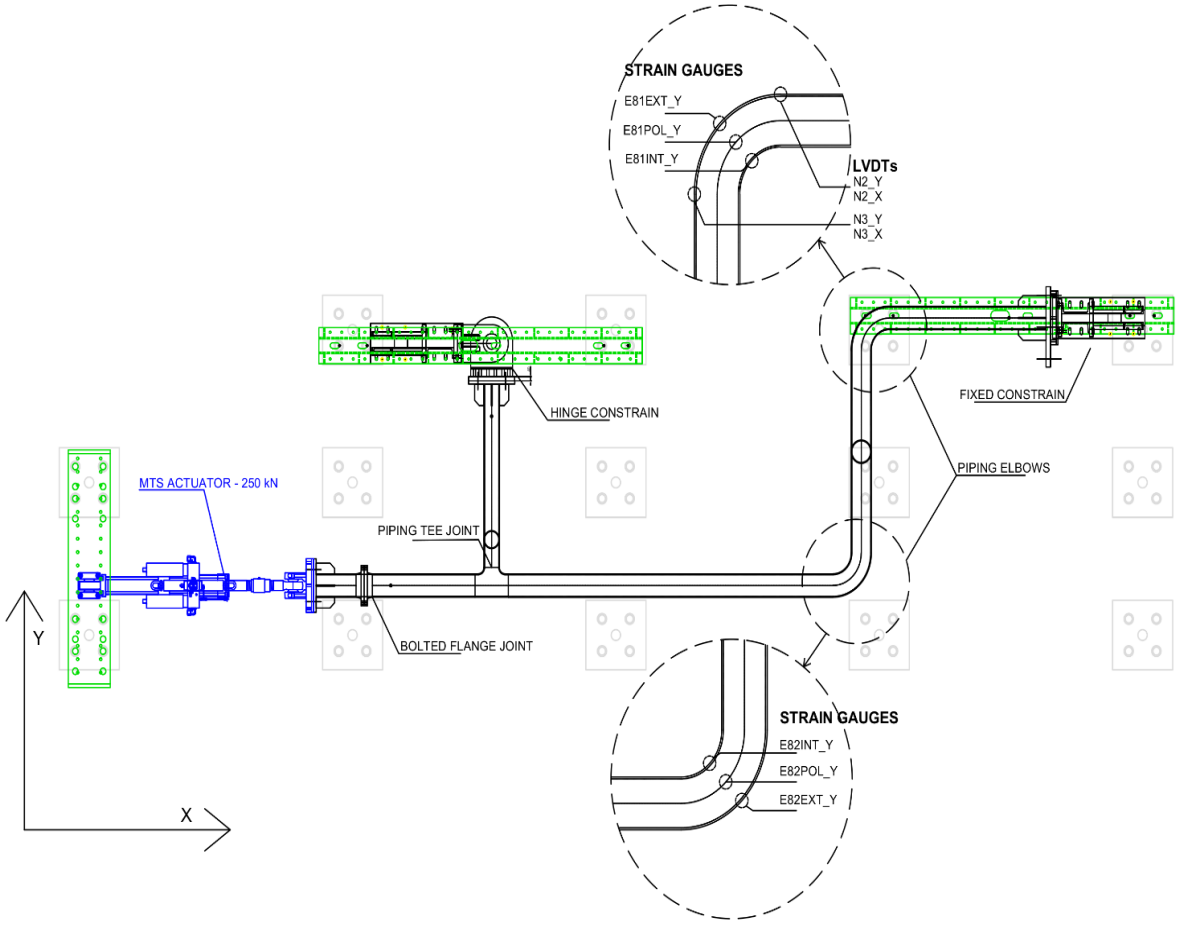

Fig. D.10: Experimental setup and sensor placement.

The experimental results from HS are used to evaluate the Kriging surrogate model and FEMs. In particular, we have two different FEMs, a high-fidelity (HF) ANSYS (ANSYS, 2015) model and a low-fidelity (LF) model. In both HF and LF models, the bolted flange joint and the tee-joint are implemented

with an equivalent spring system based on experimental findings according to Bursi et al., 2017. Moreover, the steel tank is built with spring and masses as in the numerical substructure of HS. On the other hand, the remaining part of the piping network are modelled with equivalent beam elements in both LF and HF model. Additionally, HF model encompasses two ELBOW290 elements which are able to calculate strain values in several points of the element itself, for reference see Fig. D.11. The computational cost for a single dynamic analysis of HF and LF models running on a simple workstation is 600 and 30 secs respectively.

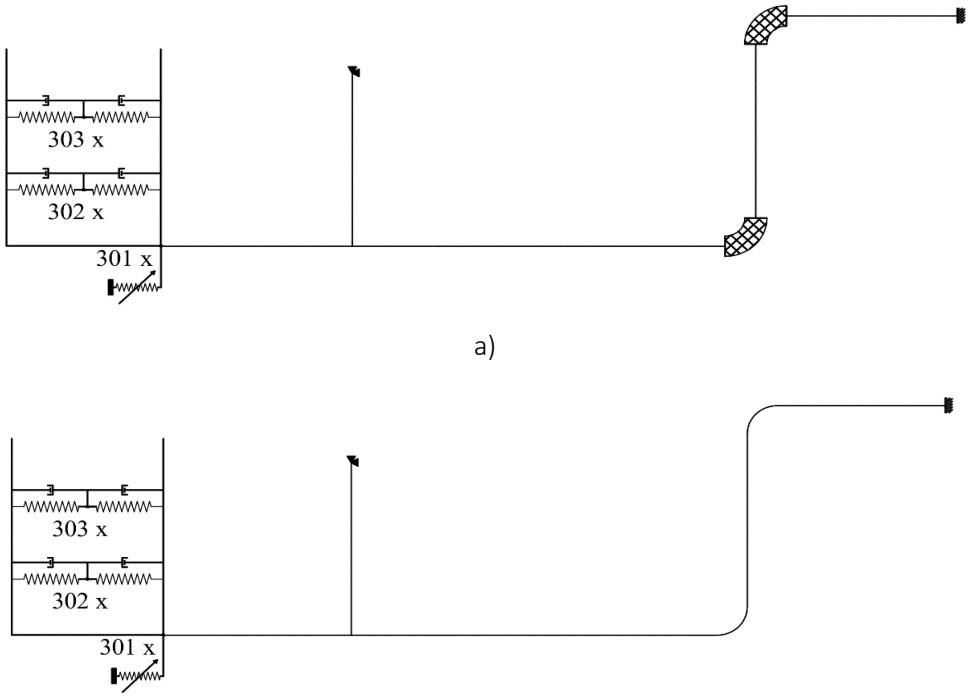

Fig. D.11: a) high-fidelity model, b) low-fidelity model.

To prepare the experimental campaign, we have to select the proper seismic input taking into account the limited number of tests practically manageable. On the other hand, we need to guarantee a certain variability of the parameters listed in Table D.2 to properly calibrate the surrogate model. For this reason, a preliminary step is that to reduce the space of these parameters selecting those with the highest influence on the system seismic response. In order to select a simple parameter to identify the seismic response with, the maximum sliding displacement of the steel tank, see Fig. D.12 for reference, is chosen since it generates the strongest external load to the piping system.

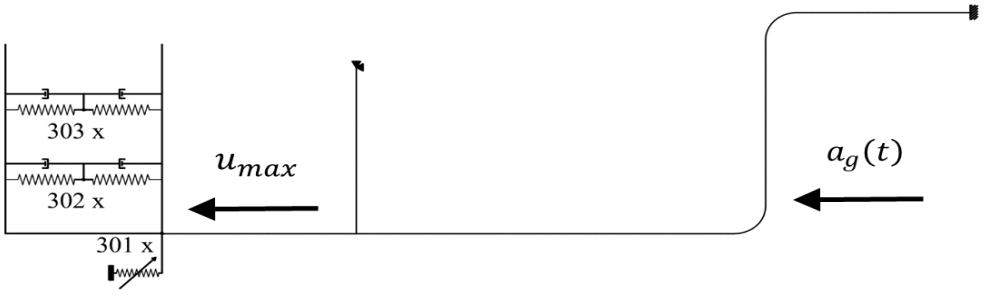

Fig. D.12: Scheme of system input/output.

Once the choice of inputs and outputs, respectively x and y, is done, it is possible to formalize them by means of:

$$x \in X_{ED} = \{I_a, D_{5-95}, T_{45}, \omega_{mid}, \zeta\} \quad \text{(D.13)}$$

$$y \in Y_{ED} = u_{max}^{80\%} \tag{D.14}$$

Thus, a set of 2e2 stochastic ground motion model parameters is generated according to the distributions defined in Table 3, in order to perform a Monte Carlo (MC) analysis with LF model. However, this set is expanded to a total of 4e4 artificial accelerograms combining each of the 2e2 parameters realizations with 2e2 different baseline noises, $\omega(\tau)$. A preliminary analysis on a smaller set is realized with a convergence check upon the 80% percentile of the maximum displacements, as depicted in Fig. D.13 while the complete distribution of u_{max} is shown in Fig. D.14.

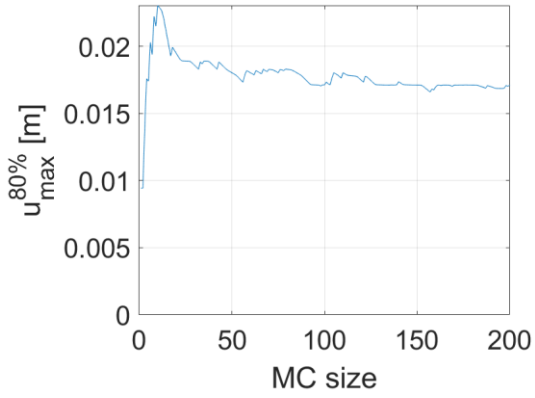

Fig. D.13: Convergence of the 80th percentile of maximum sliding displacement.

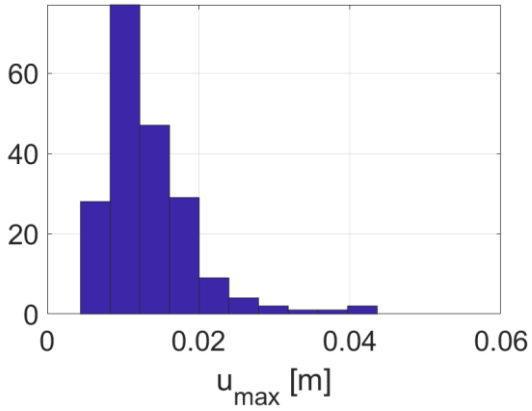

Fig. D.14: Distribution of maximum sliding displacements.

Therefore, a global sensitivity analysis (GSA) is adopted to assess the individual contributions of each of the input variables to the variance of the model response. A GSA can be performed with Sobol' decomposition (also called general ANOVA decomposition) of the computational model, which allows one to decompose a full model response in submodels, according to Sobol, 1993. As stated in Marelli and Sudret, 2014, polynomial chaos expansion (PCE) methodology provides an effective way to estimate the Sobol' indices, by spost-processing the polynomial coefficients. The analytical formulation of PCE method can be written as follows

$$\hat{y}(\boldsymbol{x}) = \mathcal{M}^{PC}(\boldsymbol{x}) = \sum_{\boldsymbol{\alpha} \in \mathcal{A}^{M,p}} y_{\boldsymbol{\alpha}} \Psi_{\boldsymbol{\alpha}}(\boldsymbol{x}) \tag{D.15}$$

Where $\Psi_{\boldsymbol{\alpha}}$ is a multivariate polynomial with multi-index vector $\boldsymbol{\alpha}$, $y_{\boldsymbol{\alpha}}$ is the coefficient of a single multivariate polynomial and $\mathcal{A}^{M,p} = \{\boldsymbol{\alpha} \in \mathbb{N}^M : |\boldsymbol{\alpha}| \leq p\}$ is the truncated set of multi-indices. In particular $\Psi_{\boldsymbol{\alpha}}$, can be written as:

$$\Psi_{\boldsymbol{\alpha}}(\boldsymbol{x}) \stackrel{\text{def}}{=} \prod_{i=1}^{M} \phi_{\alpha_i}^{(i)}(x_i) \tag{D.16}$$

where $\Psi_{\alpha_i}^{(i)}(X_i)$ is a univariate polynomial of degree α_i orthonormal with respect to the distribution of the input variable X_i. With respect to this, Table D.5 summarizes the usual pairs of polynomial families with their associated PDFs.

Table D.5: Classical families of orthogonal polynomials and the related PDFs.

Probability density function	Orthogonal polynomials
Uniform	Legendre
Gaussian	Hermite
Gamma	Laguerre
Beta	Jacobi

$$E[\mathcal{M}^{PC}(\boldsymbol{x})] = y_0 \tag{D.17}$$

$$Var[\mathcal{M}^{PC}(\boldsymbol{x})] = \sum_{\substack{\boldsymbol{\alpha} \in \mathcal{A}^{M,p} \\ \alpha \neq 0}} y_{\boldsymbol{\alpha}}^2 \tag{D.18}$$

In order to proceed with Sobol' decomposition of the computational model M and according to the procedure reported in Abbiati et. al, 2015, we can write:

$$M(\boldsymbol{x}) = M_0 + \sum_{i=1}^{M} M_i(x_i) + \sum_{1<i<j\leq M} M_{ij}(x_i, x_j) + \cdots + M_{12\ldots M}(\boldsymbol{x}) \tag{D.19}$$

Where M_0 is a constant, $\{M_i(x_i), 1 \leq i \leq M\}$ are univariate functions, $\{M_{ij}(x_i, x_j), 1 \leq i < j \leq M\}$ are bivariate functions. With the definition of a multi-index $\boldsymbol{u} = \{i_1, \ldots, i_s\} \subset \{1, \ldots, M\}$, the Sobol' decomposition can be rewritten as:

$$M(\boldsymbol{x}) = M_0 + \sum_{\substack{\boldsymbol{u} \subset \{1,\ldots,M\} \\ \boldsymbol{u} \neq \emptyset}} M_{\boldsymbol{u}}(\boldsymbol{x}_{\boldsymbol{u}}) \tag{D.20}$$

Partial variances can be defined as follows:

$$D_{\boldsymbol{u}} \stackrel{\text{def}}{=} \mathrm{Var}\big(M_{\boldsymbol{u}}(\boldsymbol{X}_{\boldsymbol{u}})\big) \tag{D.21}$$

By taking into account the orthogonality of the elements of the decomposition, total variance of the model output can accordingly be defined as the sum of the partial variances over all the possible subsets :

$$D \stackrel{\text{def}}{=} \mathrm{Var}\big(M(\boldsymbol{X})\big) = \sum_{\substack{\boldsymbol{u}\subset\{1,\dots,M\} \\ \boldsymbol{u}\neq\emptyset}} D_{\boldsymbol{u}} \tag{D.22}$$

The Sobol' index for each subset of input variables $\boldsymbol{u}$ can be written as follows:

$$S_{\boldsymbol{u}} = \frac{D_{\boldsymbol{u}}}{D} \tag{D.23}$$

On the other hand, *first-order* Sobol' indices are defined as:

$$S_i = \frac{D_i}{D} \tag{D.24}$$

These indices measure the contribution of each single variable (without interactions with others) to the total variance. Conversely, Total Sobol' indices quantify the entire contribution of each variable, both singularly and in interaction with others, to the total variance:

$$S_i^T = \sum_{\boldsymbol{u}\ni i} S_{\boldsymbol{u}} \tag{D.25}$$

By means of (D.18) we can rewrite (D.24) and (D.25) as:

$$\hat{S}_i^{PC} = \frac{\sum_{\boldsymbol{\alpha}\in\mathcal{A}_i} \hat{y}_{\boldsymbol{\alpha}}^2}{\sum_{\substack{\boldsymbol{\alpha}\in\mathcal{A} \\ \boldsymbol{\alpha}\neq\mathbf{0}}} \hat{y}_{\boldsymbol{\alpha}}^2}, \quad \mathcal{A}_i = \{\alpha \in \mathcal{A} : \alpha_i > 0,\ \alpha_{j\neq i} = 0\} \tag{D.26}$$

and

$$\hat{S}_i^{T,PC} = \frac{\sum_{\boldsymbol{\alpha}\in\mathcal{A}_i^T} \hat{y}_{\boldsymbol{\alpha}}^2}{\sum_{\substack{\boldsymbol{\alpha}\in\mathcal{A} \\ \boldsymbol{\alpha}\neq\mathbf{0}}} \hat{y}_{\boldsymbol{\alpha}}^2}, \quad \mathcal{A}_i^T = \{\alpha \in \mathcal{A} :\ \alpha_i > 0\} \tag{D.27}$$

Finally, the results of GSA with the relevant values of Sobol' indices are showed in Fig. 15.

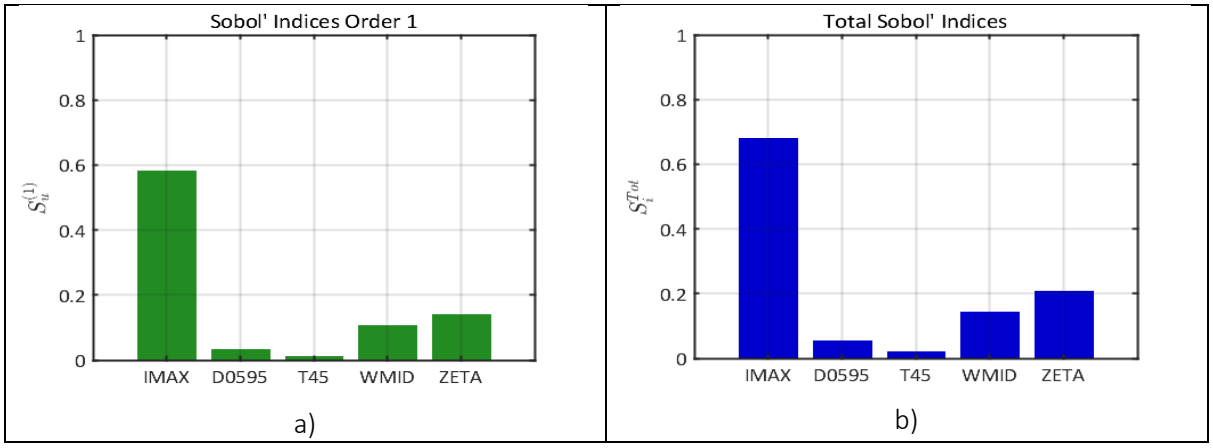

Fig. D.15: a) first-order and b) total Sobol' indices.

From Fig. D.15 it is possible to notice that three parameters generate most part of the output variance, i.e. I_a, ω_{mid} and ζ. This is somehow expected since they represent the most significant part of the intensity of seismic signals effects. Based on GSA results these three parameters are chosen to vary according to the statistical distributions defined in Table D.3, while the remaining three are fixed at their average value as reported in Table D.6.

Table D.6: Constant parameters.

Name	Value	Units
D_{5-95}	10.441	s
T_{45}	3.700	s
$\dot{\omega}$	-0.568	rad/s2

According to these modifications to the parameters distributions, a new set of 4e4 artificial accelerograms is so generated combining 2e2 parameters realizations with 2e2 different baseline noises. From this set of artificial accelerograms, seven signals are selected to be tested with HS. Among them, 4 are chosen to keep the system in the linear regime, equivalent to service limit state (SLS), and 3 to go slightly in the non-linear regime, to investigate ultimate limit state (ULS). This categorization is made upon u_{max} value predicted by LF model, by setting $u_{max} < 0.04\ m$ for SLS signals and $u_{max} > 0.06\ m$ for ULS ones. Spectral accelerations and displacements of these 7 accelerograms are depicted in Fig. D.16 and D.17 respectively with SLS signals in blue and ULS in red.

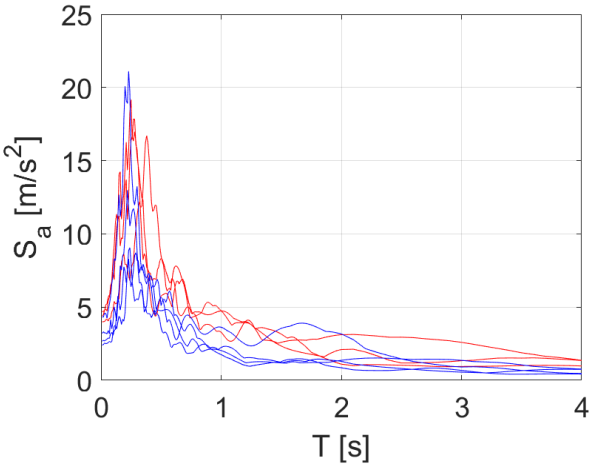

Fig. D.16: Spectral accelerations of ULS (red) and SLS (blue) artificial seismic signals

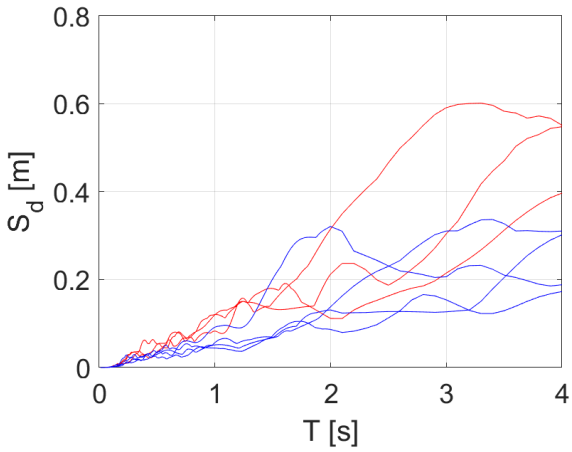

Fig. D.17: Spectral displacements of ULS (red) and SLS (blue) artificial seismic signals

Thus, these 7 signals are experimentally tested with HS and two examples of strain values detected in one of the elbows together with hysteresis loops are depicted in Fig. D.18- D.21.

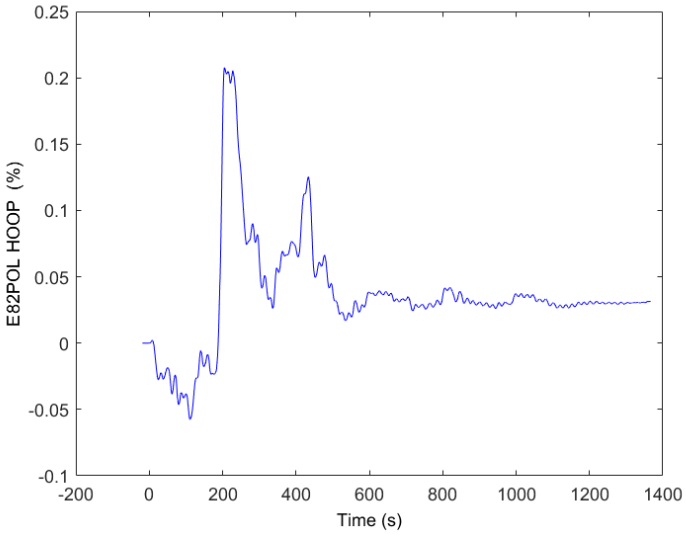

Fig. D.18: Elbow hoop strain - ULS seismic signal

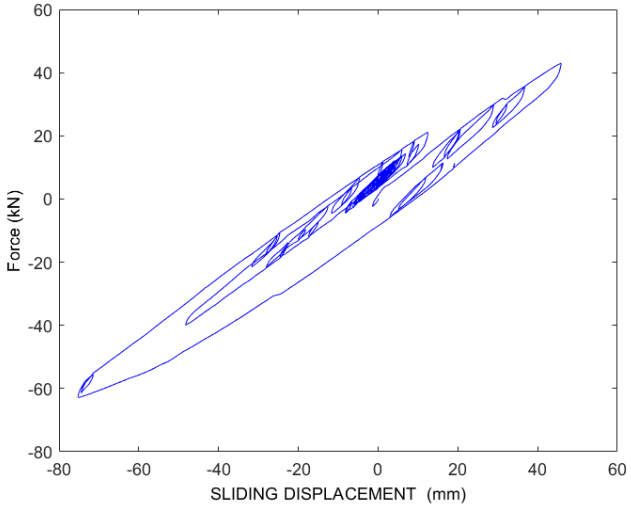

Fig. D.19: MTS force versus sliding displacement – ULS seismic signal

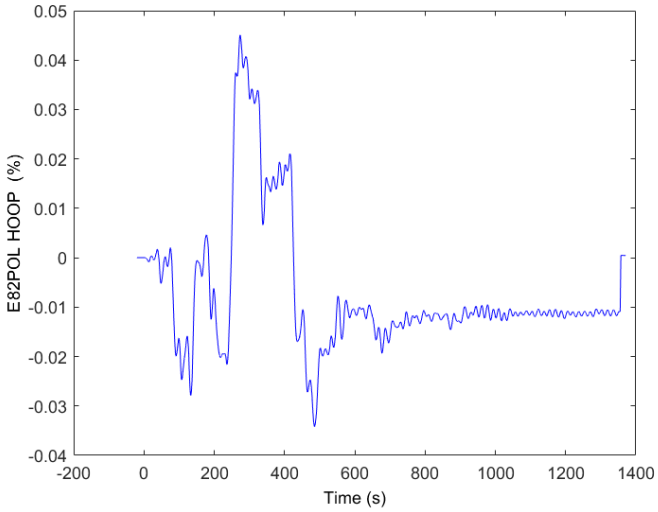

Fig. D.20: Elbow hoop strain - SLS seismic signal

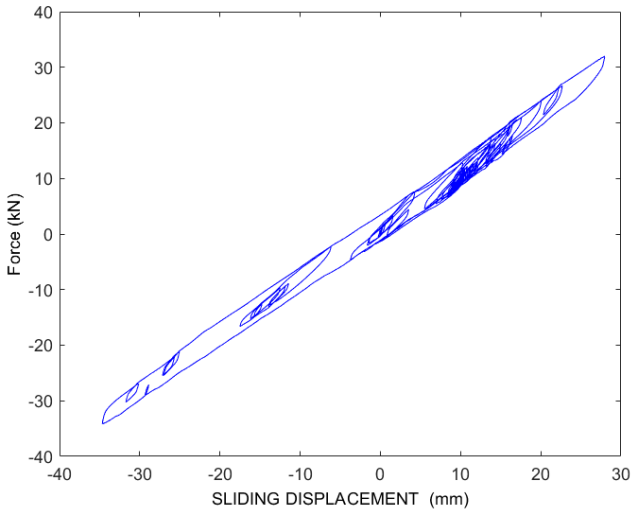

Fig. D.21: MTS force versus sliding displacement – SLS seismic signal

As it is possible to notice from both hysteresis loops and strains values, the system response for SLS signals mostly remain in linear regime while, for ULS ones, it exhibits a certain degree of nonlinearity.

Hereafter, outputs from experimental tests are adopted to better calibrate HF model with a special focus on strain level in the elbows. With respect to this output, a comparison showing a good accuracy of HF model is represented in Fig. D.22

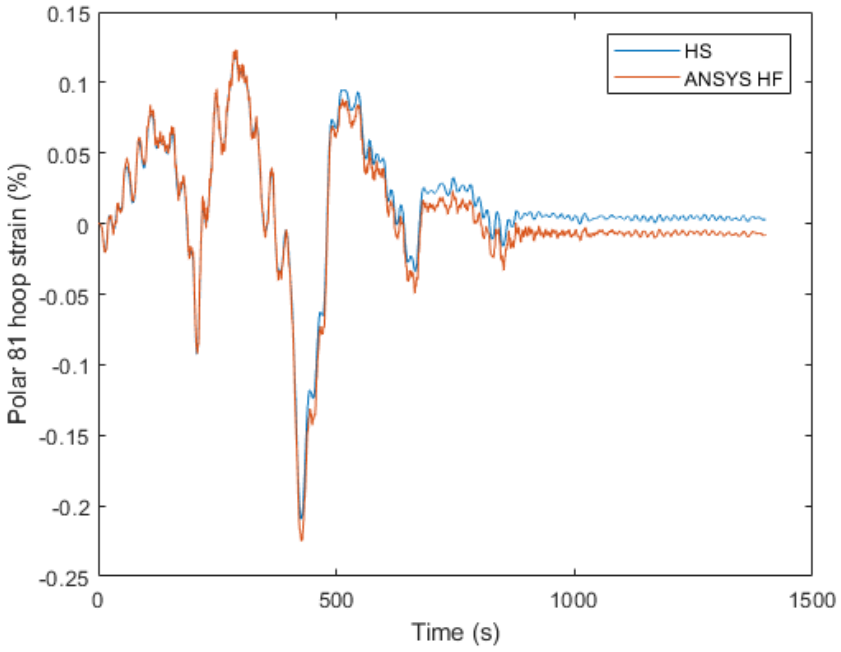

Fig. D.22: Comparison between HS and HF model elbow strain outputs for - ULS signal.

At this point, HF model is going to be used to produce a certain number of outputs from different artificial accelerograms properly selected from the same set of SLS and ULS signals. Hence, both experimental values and HF model outputs will be adopted to evaluate a Kriging hierarchical surrogate model as in Abbiati et al., 2018. In detail, this numerical model is going to be able to take as input the parameters of the stochastic ground motion model and gives as outputs the evaluation of the system seismic response, as for example, elbows maximum strains. Hence, it is possible to write inputs and outputs of the surrogate model as:

$$x \in X_{ED} = \{I_a, \omega_{mid}, \zeta\} \tag{D.28}$$

$$y \in Y_{ED} = \varepsilon_{elbow} \tag{D.29}$$

With this premise, the analytical formulation of the Kriging surrogate model is defined as follows:

$$\begin{bmatrix} Y^* \\ \boldsymbol{Y} \end{bmatrix} \sim \mathcal{N}_{N+1}\left(\begin{bmatrix} \mu^*(X^*) \\ \boldsymbol{\mu}(\boldsymbol{X}) \end{bmatrix}, \begin{bmatrix} \Sigma^{**}(X^*, X^*) & \boldsymbol{\Sigma}^*(X^*, \boldsymbol{X}) \\ \boldsymbol{\Sigma}^*(\boldsymbol{X}, X^*) & \boldsymbol{\Sigma}(\boldsymbol{X}, \boldsymbol{X}) \end{bmatrix}\right) \tag{D.30}$$

where $\boldsymbol{Y}$ is the observed response at $\boldsymbol{X}$, Y^* is the predicted response at X^*, $\boldsymbol{\mu}$ is the mean vector and $\boldsymbol{\Sigma}$ the covariance matrix. Furthermore, in order to proceed with fragility analysis, see for reference Baker, 2015, we will rely on statistical data from elbows resistance and relative leakage thresholds from Pedot et al., 2018, depicted in Fig. D.23.

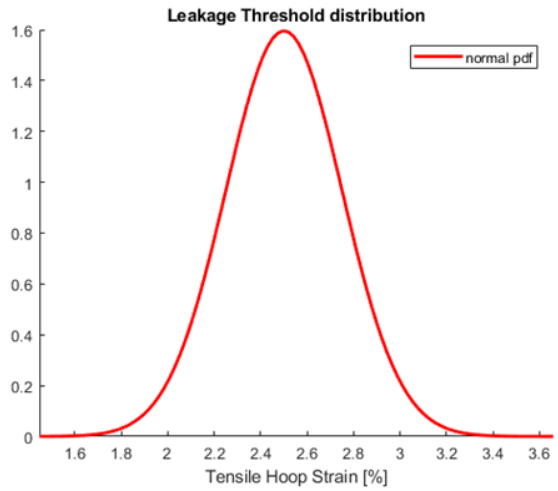

Fig. D.23: Leakage threshold distribution for elbow strain, according to Pedot et al., 2018

Finally, with artificial accelerograms, the relevant seismic responses of tank-piping system from surrogate model and LOC threshold, we will be able to evaluate fragility curves for piping elbows.

5 Uncertainty analysis on a stochastic finite-fault model for ground motion generation

5.1 Finite-fault rupture model

This section deals with the uncertainty analysis in the synthesis of ground motions due to seismic fault rupturing and accounting for wave propagation and site effects [50]. The characteristics of a fault rupture as a large finite source, including rupture propagation, directivity effects and source geometry can profoundly influence the amplitude, frequency content and duration of a ground motion. The stochastic approach estimates ground motions on the basis of physical properties of the energy release and the travel path of seismic waves.

The development of stochastic-based ground motion synthesis associated to a seismological finite-fault modelling is a worldwide used approach that can be used for representing future large magnitude earthquakes occurring in a given location. It allows for the reproduction of specific source effects, like directivity and distribution of asperities, as well as path and crustal effects.

For a realistic and feasible ground motion prediction, it is important to adopt a set of assumptions about the earthquake source spectrum, path effects and site conditions. In order to make allowance for these issues, the methodology applied for ground motion characterisation combines:

(i) The finite-earthquake-source modelling technique (Beresnev and Atkinson, 1998), which includes: a fault discretised into several elements (sub-faults); a nucleation point (initial rupture point); a heterogeneous slip distribution; a rupture velocity; and the sum, at the target site, of the contribution of each element lagged in time (Fig. E.1).

The ground motion at an observation point is thus obtained by summing the contributions from all sub-faults. An element triggers when the rupture reaches its centre. The contributions from all elements are lagged, and are then summed at the receiver, the time delay for an element being given by the time required for the rupture to reach the element, plus the time for shear wave propagation from the element to the receiver. The total duration of motion corresponds therefore to the source duration plus the path duration.

(ii) The source-point stochastic model: each element of the fault is modelled as a stochastic omega-square point source, i.e., the amplitude of the acceleration Fourier spectrum for each sub-fault is computed as a product of the spectrum produced by the source at a certain distance and of filtering functions representing the effects of path attenuation and site response (Figure E.2).

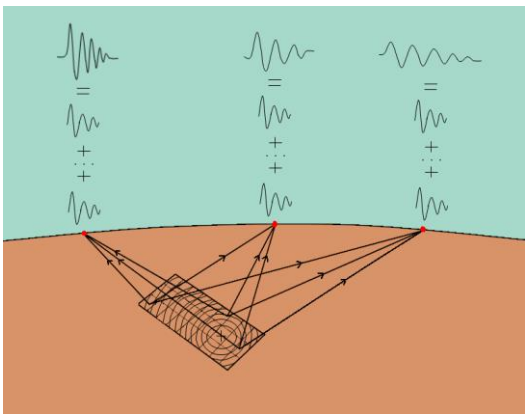

Figure E.1 – Summation process, with contributions from all sub-faults.

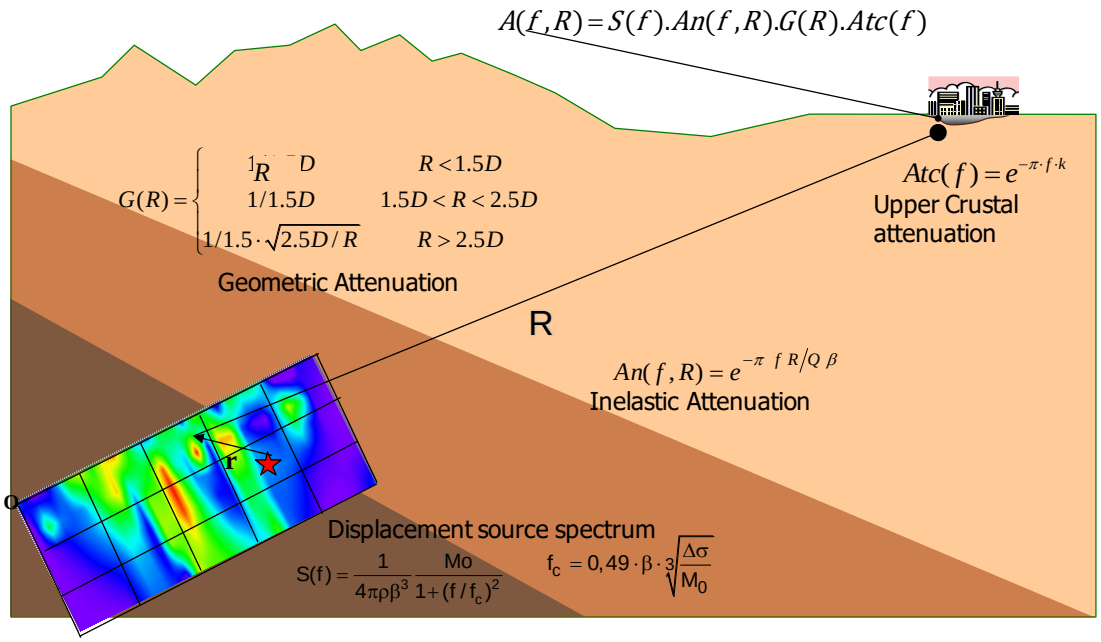

Figure E.2 – Schematic view of the stochastic simulation.

5.1.1 Model parameters

The total radiation at a specific site, defined by the Fourier Acceleration Amplitude spectrum is a result of contributions from earthquake source, path and site and is defined, with reference to Boore (1983), by:

$$A(f,M_0,R) = (2\pi f)^2 C\ S(f,M_0)\ G(R)\ An(f,R)\ Atc(f) \tag{E.1}$$

where:

- C is a scaling factor, defined by $C = \Re VF/4\pi\rho\beta^3$, in which $\Re$ is the wave radiation pattern factor (= 0.55 on average for shear waves), V is the partition of total shear-wave energy into horizontal components (= $1/\sqrt{2}$), F is the free-surface amplification factor (= 2), and ρ and β are the density (in g/cm^3) and the shear wave velocity (in km/s) of the rock, respectively, in the vicinity of the source;

- $S(f,M_0)$ is the displacement source spectrum represented by:

$$S(f,M_0) = \frac{M_0}{1+(f/f_c)^2} \tag{E.2}$$

where f is the frequency of the wave, M_0 is the seismic moment and f_c the source corner frequency related to the stress drop, $\Delta\sigma$ (in bar), through:

$$f_c = 4.9x10^6\,\beta\left(\Delta\sigma/M_0\right)^{1/3} \tag{E.3}$$

and the seismic moment related through $M_w = (2/3)\log_{10} M_0 - 10.7$ with the moment magnitude, M_w.

- $G(R)$ is a geometric attenuation factor, which reduces the entire spectrum with the distance from the source, R (in km), without altering its shape. The spectrum ordinates are proportional to R^b, according to:

$$G(R) = \begin{cases} R^{b_1} & R < 1.5D \\ (1.5D)^{b_1}\left(\frac{R}{1.5D}\right)^{b_2} & 1.5D < R < 2.5D \\ (1.5D)^{b_1}\left(\frac{2.5D}{1.5D}\right)^{b_2}\left(\frac{R}{2.5D}\right)^{b_3} & R > 2.5D \end{cases} \quad \text{(E.4)}$$

being D the crustal thickness (in km) and the exponents usually taken as b_1 = -1, b_2 = 0, and b_3 = -1/2;

- $An(f,R)$ is the path inelastic attenuation factor (Boore and Atkinson, 1987):

$$An(f,R) = e^{-\pi f R/Q\beta} \quad \text{(E.5)}$$

in which $Q(f)$ is the wave transmission quality factor, defined by the expression $Q(f) = Q_o f^{\nu}$, where Q_o is the quality factor at 1 Hz and ν is indicative of the degree of heterogeneity of the crust. This factor alters the spectral shape by reducing high frequencies more rapidly with distance than lower frequencies;

- $Atc(f)$ is the upper crust attenuation factor, corresponding to a low-pass filter which accounts for the observation that acceleration spectra often show a sharp decrease with increasing frequency above some cut-off frequency. It can be computed as:

$$Atc(f) = e^{-\pi f k} \quad \text{(E.6)}$$

with *kappa*, k, being a distance-independent parameter.

The rock ground motion representation by the Fourier Acceleration Amplitude spectrum may then be transformed into a spectral response by using the transfer function of a single-degree-of-freedom (SDoF) linear oscillator. This is accomplished by first estimating the one-sided spectral density function from the locally averaged Fourier Amplitudes:

$$S_a(\omega) = \left|\overline{A(\omega,R)}\right|^2 \Big/ \pi T \quad \text{(E.7)}$$

where T is the duration of strong motion and $\omega = 2\pi f$.

Secondly, to calculate a response spectrum at frequency f_n, the spectral density function of a linear oscillator response can be used, as follows:

$$S_x(\omega) = S_a(\omega)|h_x(\omega,\omega_n,\varepsilon)|^2 \quad and$$
$$h_x(\omega,\omega_n,\varepsilon) = \frac{1}{-{\omega_n}^2 + \omega^2 + 2i\varepsilon\omega_n\omega} \quad \text{(E.8)}$$

being $h_x(\omega,\omega_n,\varepsilon)$ the transfer function of a (SDoF) linear oscillator with natural frequency f_n and damping ratio ε. Afterwards, the root-mean-square (RMS) response of the oscillator can be determined, for which it is convenient to represent the moments of the spectral density function $S_x(\omega)$:

$$\lambda_k = 2\int_0^{\infty} \omega^k S_x(\omega)\, d\omega \quad \text{(E.9)}$$

and then the RMS response can be computed as:

$$\sigma_{rms} = (\lambda_0)^{1/2} \quad \text{(E.10)}$$

Finally, the peak response, the spectral acceleration SA, is estimated according to:

$$SA\ (f_n) = \sigma_{rms} p_f(f_n, T) \quad \text{(E.11)}$$

where p_f is a peak factor that depends on the natural frequency and duration, and can be estimated by $pf = \sqrt{2 \ln n} + 0.577/\sqrt{2 \ln n}$, being n the number of half-cycles of vibration ($n = 2 f_{cent} T$, with f_{cent} the central frequency, $f_{cent} = \frac{1}{2\pi}\left(\frac{\lambda_2}{\lambda_0}\right)^{1/2}$).

So, in concept, the application of the stochastic method is straightforward. One starts with a source spectrum modified for path and near-surface rock conditions (expression E.1), converts it to the power spectral density of an oscillator (E.7 and E.8), computes the RMS response of the oscillator (E.9 and E.10) and estimates the spectral acceleration with a peak factor (expression E.11).

In the case one is modelling the ground motion at a soil site with an equivalent linear soil model, simply transform the rock spectral density into a soil spectral density by using an expression similar to E.8.

Additionally, finite-fault simulations require the definition of: (i) the fault-plane geometry (length, width, strike, dip, number of sub-faults considered and depth to the upper edge of the fault); (ii) the source parameters (seismic moment, slip distribution, stress drop, nucleation point, rupture velocity); (iii) the crustal properties of the region (geometrical spreading coefficient and inelastic attenuation); and (iv) the site-specific soil response information.

These model parameters have been calibrated with a dataset of horizontal components of ground acceleration records (at rock sites) from the Portuguese digital accelerometer network and with independent studies. The dataset of digital acceleration records includes horizontal components of ground acceleration records on hard sites, for events with moment magnitudes ranging from 4.1 to 5.3 and epicentre distances ranging from 15 to 320 km. As two physical mechanisms of earthquake generations exists in Portugal, namely interplate events originated by the movement between the Eurasian and African plates and intraplate events originated in faults inside the Eurasian plate, calibration of model parameters was done separately with data corresponding to intraplate and interplate events.

5.1.2 Probability distributions of key parameters

Uncertainties in ground motion estimation can be distinguished in two categories: aleatory uncertainties associated to random effects and epistemic uncertainties related to the lack of knowledge.

To account for the uncertainty in the model parameters, and to estimate upper bound seismic inputs it is important to perform a large number of runs for the same fault. The effects of aleatory uncertainty were considered by expressing random variability in the parameters from one ground motion realisation to another. Each key parameter (length, width and strike of the fault, stress drop, upper crustal attenuation and geometric-spreading coefficient) were assigned a probability distribution (truncated normal, lognormal or uniform distributions, depending on the parameter which was being modelled). The mean values and standard deviations of the model's input parameters were considered to be well established previously (Carvalho *et al.*, 2009).

It is important to mention that it is not the intention of this section to express uncertainty in a mathematically consistent way but rather to model random fluctuations in the actual values of the parameters, in order to obtain estimates of the likely range of the upper bound of some parameters (Bommer, 2002). Details on aleatory uncertainty considerations can be found in Atkinson and Boore (2006).

Source parameters:

Fault dimensions were calculated using empirical relations, relating moment magnitude, length and width of the fault. These regression equations are considered as an upper bound of the fault dimensions, which are allowed to have some variability by multiplying their length and width by independent truncated normally distributed factors, with mean value of 0.8 and standard deviation of 0.2 (although limited to the range 0.4 to 1.0).

The slip model is a very important source of variability in ground motion simulations. However, the random slip distribution, for all ranges of frequencies, seems to be a correct assumption when the slip distribution of a past earthquake is not known or for predicting a strong ground motion. Therefore, the random slip distribution is considered inside the source code and is not an input parameter. The rupture velocity is assumed to be equal to 2.5 km/s.

The most important source parameter is the stress drop, which controls the spectral magnitude at high frequencies. Following Carvalho *et al*. (2009), a median stress parameter of 101 bar for intraplate scenarios (the ones that have the fault source inside Portugal mainland) and 66 bar for interplate scenarios (the ones that have the fault source offshore Portugal, in the Atlantic Ocean) are adopted. Its uncertainty is expressed by a normal distribution, in $\log_{10}$ stress, with mean 2.00 $\log_{10}$ units for intraplate scenarios and 1.82 $\log_{10}$ units for interplate scenarios, and a standard deviation of 0.2 $\log_{10}$ units.

The probability distributions, mean values, standard deviation and limit values for the source parameters assumed in the stochastic simulation are summarised in Table E.1.

Table E.1 – Uncertainty in source parameters.

Parameter	Distribution type	Mean	Standard deviation	Min.	Max.
Magnitude	–	To be defined	–	–	–
Fault strike (NθºE)	–	To be defined	–	–	–
Fault dip (º)	–	To be defined	–	–	–
Fault dimension factors (for length and width)	Truncated normal	0.8	0.2	0.4	1
Stress drop (in $\log_{10}$ units)	Lognormal	[1]2.02 [2]1.82	0.2	–	–

[1] intraplate earthquakes
[2] interplate earthquakes

Path and site parameters:

Regarding the crustal attenuation properties, for the inelastic attenuation, *An(f,R)* in Eq. E.5, the frequency-dependent quality factor $Q(f) = 250\, f^{0.7}$ of Pujades *et al.* (1990) is adopted. With respect to the geometric attenuation, *G(R)* in Eq. E.4, the tri-piecewise function described by Atkinson and Boore (1995) is used, assuming a crustal seismogenic thickness of 31 km for intraplate earthquakes and 20 km for interpolate earthquakes (Jiménez-Munt *et al*., 2001). The shear wave velocity is assumed to be 3.5 km/s while the crustal density is 2.8 g/cm^3.

The uncertainty of attenuation with distance, both geometric and inelastic, should, of course, also be taken into account. Atkinson (2004) showed that geometric spreading is significantly faster at near-source distances (1.5 times the crustal seismogenic thickness) than previous studies indicated. On the other hand, Atkinson and Boore (2006) modelled the aleatory uncertainty in the attenuation by normal

distributions of the geometric-spreading coefficients pointing out that the variability considered is sufficient to model the net effects of uncertainty in all attenuation parameters (including the *Q* factor in the inelastic attenuation) and that mapping all of the attenuation uncertainty into geometric is a simple way to approximate the expected overall behaviour.

To account for the near-surface attenuation factor, a low-pass filter is applied which describes the observed rapid spectral decay at high frequencies, $Atc(f) = \exp(-\pi f k)$. Carvalho *et al.* (2009) inferred a value of $k = 0.03$ s from the analysis of the dataset of acceleration records. This parameter is found to have a relevant impact on the predicted amplitudes of ground motions. Therefore, its aleatory uncertainty is modelled by a uniform distribution taking values between 0.015 and 0.04 s.

The probability distributions, mean values, standard deviations and limit values for the path and site parameters assumed in the stochastic simulation are summarised in Table E.2.

Table E.2 – Uncertainty in path and site parameters.

Parameter	Distribution type		Mean	Standard deviation	Min.	Max.
Crustal thickness D (km)	–		[1]31 [2]20	–	–	–
Geometric spreading R^b	Truncated normal	b_1	-1.0	0.2	-1.2	-0.8
		b_2	0.0	0.2	-0.1	0.1
		b_3	-0.5	0.2	-0.6	-0.4
Kappa (s)	Uniform		–	–	0.015	0.04

[1] intraplate earthquakes
[2] interplate earthquakes

5.1.3 Uncertainty propagation

Figure E.3 presents the results, in terms of response spectral amplitudes, of 15 random realisations of the model, according to the probability distributions of its parameters. A random distribution of the slip and a random nucleation point were also considered, in order to capture directivity effects.

In terms of seismic scenarios, due to the seismotectonic characteristics of Portugal, two scenarios were considered: (i) an interplate scenario, characterising long distance and large magnitude earthquakes, with their epicentres mainly offshore; and (ii) an intraplate scenario, characterising short distance and moderate magnitude earthquakes. Figure E.4 depicts schematically some important fault sources which may originate earthquakes affecting Portugal mainland.

The fault geometric parameters and the magnitudes considered are summarised in Table E.3. All simulations were carried out for downtown Lisbon (coordinates 38.709, -9.137).

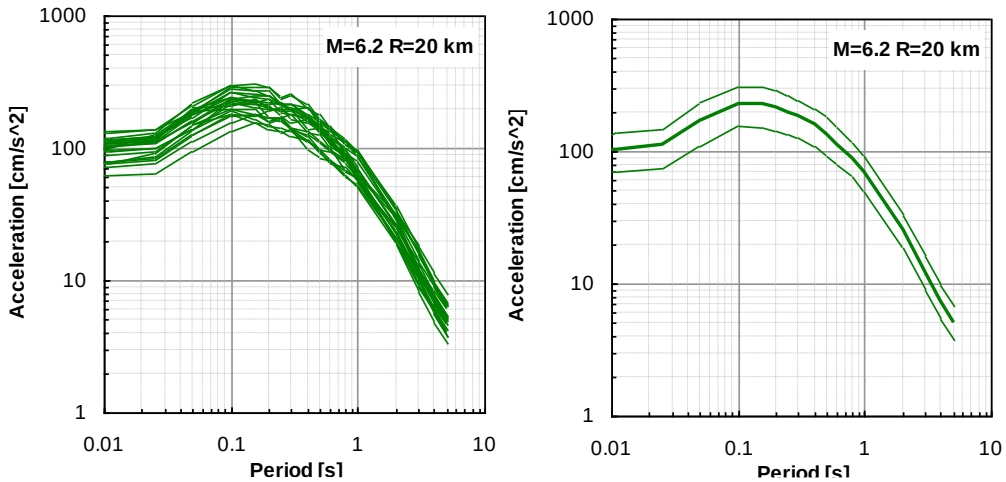

Figure E.3 – Left: 15 response spectra, corresponding to the random trials simulated; Right: mean and the mean plus and minus one standard deviation spectra.

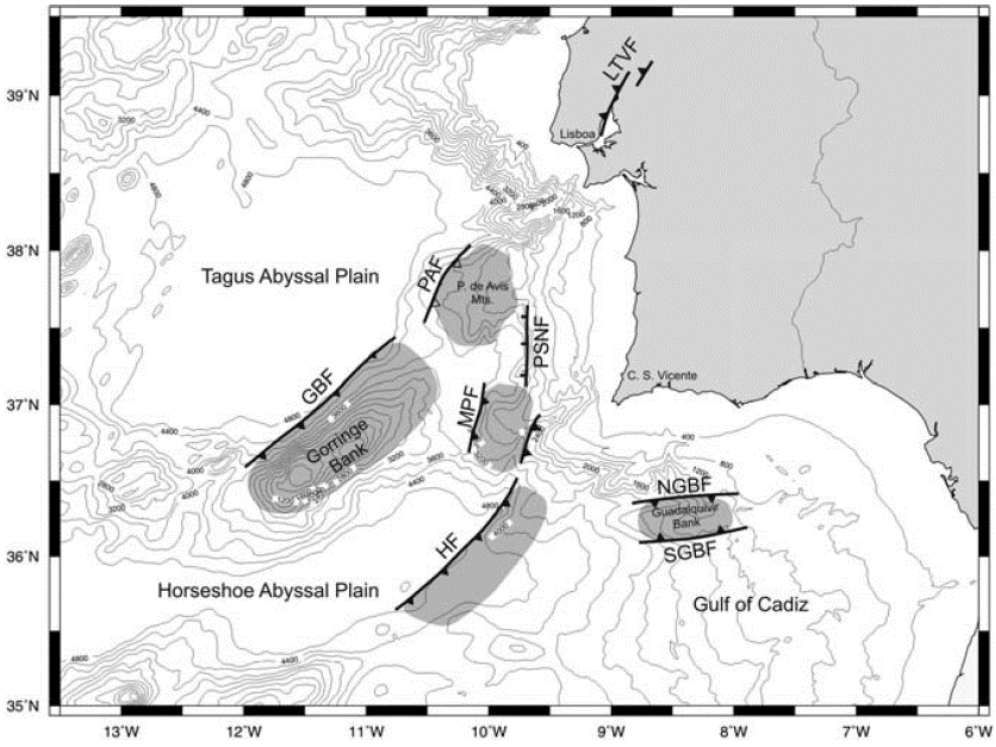

Major seismogenic zones in the SW Iberia Margin. GBF – Gorringe Bank Fault; PAF – Príncipes de Avis Fault; MPF – Marquês de Pombal Fault; HF – Horseshoe Fault; NGBF – Northern Guadalquivir Bank Fault; Southern Guadalquivir Bank Fault; PSNF – Pereira de Sousa Normal Fault; LTVF – Lower Tagus Valley Fault. Modified after Zitellini et al. (2004)

Figure E.4 – Important fault sources for Portugal mainland.

Table E.3 – Fault geometric parameters and magnitudes.

Fault	Strike	Dip	Origin coordinates	Magnitudes
MPF	N20ºE	24º	36.40, -10.20	7; 7.5; 8
GBF	N60ºE	40º	36.25, -12.20	7; 7.5; 8
LTVF	N220ºE	55º	39.00, -8.90	5.5; 6.5; 7.1
HF	N60ºE	45º	35.70, -10.75	7; 7.5; 8; 8.5

The objective was thus to perform a propagation and uncertainty analysis of a model for stochastic generation of ground motions using the First Order Second Moment Method (FOSM), Monte Carlo Simulation (MCS) Method and the Response Surface Method (RSM). A local and a global sensitivity analysis were also performed in order to identify the sources of uncertainty which contribute more to the uncertainty in the model output.

Each simulation was performed for 200 frequencies between 0.1 Hz and 50 H. However, the ordinates of the response spectra to be analysed focused on just two frequencies (periods): 1 Hz (1 s) and 5 Hz (0.2 s). The final goal of this section was to describe probabilistically the spectral acceleration at those periods, based on Monte Carlo simulations for uncertainty propagation, with enough samples to achieve a confidence interval with an error on the mean value of less than 5% of its value.

Due to lack of space, in the following it is only analysed the uncertainty propagation related with the interplate scenarios of the **Horseshoe Fault (Magnitude 8.5) and Gorringe Bank Fault (Magnitude 7.5)**.

5.1.3.1 First order second moment

The First Order Second Moment method (FOSM) is based on the first order Taylor series expansion of the model output around the mean value or the random input variables.

The conditions imposed for using the method are that:

- The uncertainties are relatively small, the standard deviation divided by the mean value being less than 0.3;
- The uncertainties have Gaussian (normal) distributions;

The formulation of FOSM is given by:

$$g \approx g(\mu_{X_1},...,\mu_{X_n}) + \sum_{i=1}^{n}(X_i - \mu_{X_i})\left(\frac{\partial g}{\partial X_i}\right)_{\mu_{X_i}}$$

$$\begin{cases} E[g] \approx g(\mu_{X_1},...,\mu_{X_n}) \\ Var[g] \approx \sum_{i=1}^{n}\left(\frac{\partial g}{\partial X_i}\right)^2 Var[X_i] + \sum_{\substack{i=1 \\ i\neq j}}^{n}\sum_{j=1}^{n}\left(\frac{\partial g}{\partial X_i}\right)\left(\frac{\partial g}{\partial X_j}\right)\rho_{ij}\sigma_{X_i}\sigma_{X_j} \end{cases}$$

For statistically independent variables it can be assumed that:

$$Var[g] \approx \sum_{i=1}^{n}\left(\frac{\partial g}{\partial X_i}\right)^2_{\mu_{X_i}} Var[X_i]$$

The probability distributions of the input parameters were considered and the partial derivatives required for determining the standard deviation of the response and the sensitivity ranking of the input parameters were computed using the finite differences method and a 5% perturbation.

Horseshoe Fault (HS) – Magnitude 8.5

FOSM moments				
f= 1Hz		f= 5Hz		
mean	62,24	mean	66,94	cm/s^2
stdev	57,89	stdev	47,23	
variance	3351,20	variance	2230,84	

	FOSM Sensitivity analysis							
	f= 1Hz				f= 5Hz			
	ai	|αi|	ai^2	Rank	ai	|αi|	ai^2	Rank
Stress Drop	0,3455	0,3455	0,1194	4	0,4616	0,4616	0,2130	3
Kappa	-0,0242	0,0242	0,0006	7	-0,1440	0,1440	0,0207	4
F. length	0,6046	0,6046	0,3655	1	-0,0339	0,0339	0,0011	7
F. width	0,5873	0,5873	0,3450	2	-0,6817	0,6817	0,4648	1
b1	0,3973	0,3973	0,1579	3	0,5293	0,5293	0,2802	2
b2	0,0311	0,0311	0,0010	6	0,0423	0,0423	0,0018	6
b3	0,1036	0,1036	0,0107	5	0,1355	0,1355	0,0184	5
		Sum	1,00			Sum	1,00	

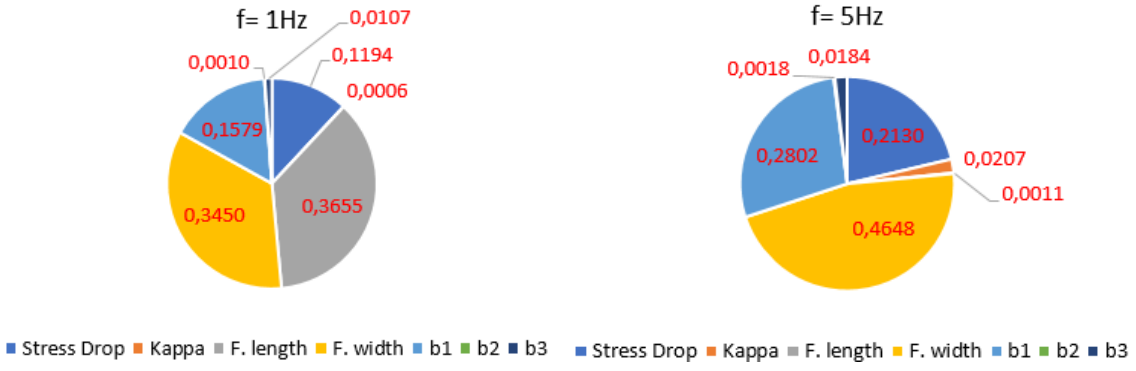

Gorringe Bank Fault (GBF) – Magnitude 7.5

FOSM moments				
f= 1Hz		f= 5Hz		
mean	21,50	mean	27,57	cm/s^2
stdev	103,38	stdev	27,45	
variance	10688,08	variance	753,60	

	FOSM Sensitivity analysis							
	f= 1Hz				f= 5Hz			
	ai	|αi|	ai^2	Rank	ai	|αi|	ai^2	Rank
Stress Drop	0,0619	0,0619	0,0038	4	0,3060	0,3060	0,0936	3
Kappa	-0,0039	0,0039	0,0000	7	-0,0947	0,0947	0,0090	6
F. length	0,5900	0,5900	0,3481	2	-0,8160	0,8160	0,6658	1
F. width	0,8009	0,8009	0,6414	1	-0,2841	0,2841	0,0807	4
b1	0,0774	0,0774	0,0060	3	0,3716	0,3716	0,1381	2
b2	0,0058	0,0058	0,0000	6	0,0291	0,0291	0,0008	7
b3	0,0232	0,0232	0,0005	5	0,1093	0,1093	0,0119	5
		Sum	1,00			Sum	1,00	

5.1.3.2 Monte Carlo simulation

The Monte Carlo simulation method is defined as the art of approximating an expectation by the sample mean of a function of simulated random variables. The method is adequate for uncertainty propagation when:

- The uncertainties on the input parameters are not large;
- The values of the input parameters follow non-normal pdfs;
- The models are complex and non-linear.

The inverse transformation method was used, with the following steps:

1. Generate a random number u_i from a uniform distribution between 0 e 1;
2. Calculate de random number x_i from the inverse cumulative density function;
3. Calculate the output (spectral acceleration);
4. Statistical analysis of the n output samples.

The crude Monte Carlo was adopted for uncertainty propagation with, respectively: 50, 500 and 1000 realizations (n) to achieve a confidence interval with an error on the mean value of less than 5%. The error calculated is given by:

$Error=(K_{CL}\times\sigma)/(\mu\times\sqrt{n})$

For a 95% confidence interval $K_{CL}=1.96$.

It was verified that an error lower than 5% could be obtained for a minimum of 500 realizations.

The descriptive statistics and histograms of the output (1000 realizations) were computed as shown below:

Descriptive statistics - MCS

	HF (M=8.5)		GBF (M=7.5)	
	1Hz	**5Hz**	***1Hz***	**5Hz**
Mean	**68,84**	**82,10**	**23,78**	**28,18**
Median	58,40	69,28	20,41	23,93
Mode	44,51	143,60	14,14	14,45
Stdev	**40,29**	**47,52**	**13,91**	**16,65**
Variance	**1623,64**	**2258,55**	**193,48**	**277,29**
kurtosis	5,96	4,25	8,29	5,71
Skewness	1,83	1,64	1,97	1,78
Range	340,68	378,01	143,90	152,71
Minimum	13,22	15,29	5,00	4,89
Maximum	353,90	393,30	148,90	157,60
Realizations	1000	1000	1000	1000

HF (M=8.5)					
1 Hz			5 Hz		
Bin	Frequency	% acumulate	Bin	Frequency	% acumulate
0	0	0,00%	0	0	0,00%
10	0	0,00%	10	0	0,00%
20	18	1,80%	20	5	0,50%
30	81	9,90%	30	50	5,50%
40	145	24,40%	40	100	15,50%
50	141	38,50%	50	116	27,10%
60	132	51,70%	60	119	39,00%
70	94	61,10%	70	118	50,80%
80	91	70,20%	80	82	59,00%
90	68	77,00%	90	78	66,80%
100	58	82,80%	100	68	73,60%
110	40	86,80%	110	46	78,20%
120	27	89,50%	120	42	82,40%
130	30	92,50%	130	33	85,70%
140	16	94,10%	140	26	88,30%
150	16	95,70%	150	25	90,80%
160	8	96,50%	160	18	92,60%
170	8	97,30%	170	16	94,20%
180	8	98,10%	180	14	95,60%
190	5	98,60%	190	9	96,50%
200	3	98,90%	200	7	97,20%
210	2	99,10%	210	4	97,60%
220	3	99,40%	220	9	98,50%
230	1	99,50%	230	2	98,70%
240	1	99,60%	240	2	98,90%
250	1	99,70%	250	1	99,00%
More	3	100,00%	More	10	100,00%

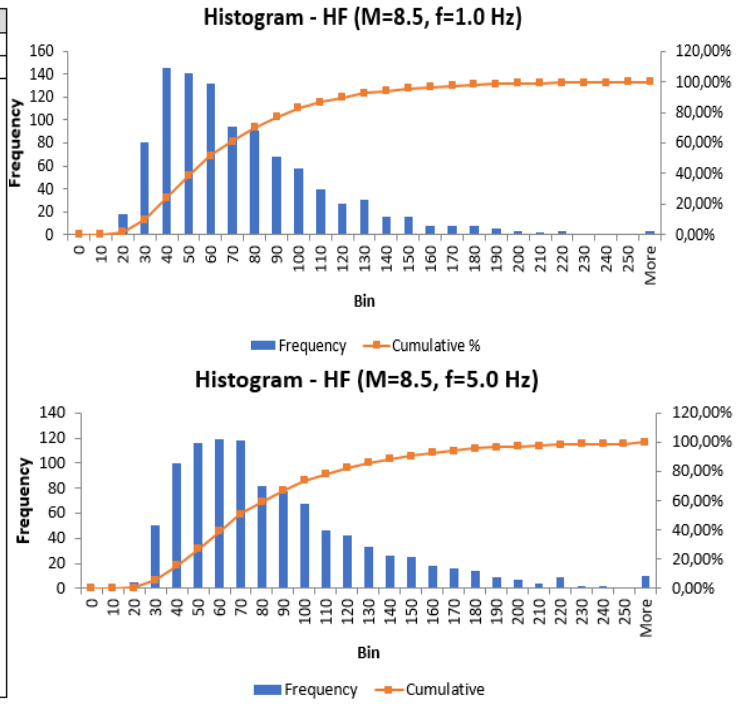

GBF (M=7.5)					
1 Hz			5 Hz		
Bin	Frequency	% acumulate	Bin	Frequency	% acumulate
0	0	0,00%	0	0	0,00%
5	1	0,10%	5	1	0,10%
10	96	9,70%	10	52	5,30%
15	200	29,70%	15	160	21,30%
20	191	48,80%	20	158	37,10%
25	147	63,50%	25	155	52,60%
30	108	74,30%	30	116	64,20%
35	88	83,10%	35	96	73,80%
40	56	88,70%	40	78	81,60%
45	40	92,70%	45	53	86,90%
50	23	95,00%	50	37	90,60%
55	18	96,80%	55	24	93,00%
60	9	97,70%	60	17	94,70%
65	6	98,30%	65	18	96,50%
70	6	98,90%	70	9	97,40%
75	4	99,30%	75	7	98,10%
80	2	99,50%	80	4	98,50%
85	3	99,80%	85	4	98,90%
90	1	99,90%	90	3	99,20%
95	0	99,90%	95	2	99,40%
100	0	99,90%	100	3	99,70%
105	0	99,90%	105	1	99,80%
110	0	99,90%	110	1	99,90%
More	1	100,00%	More	1	100,00%

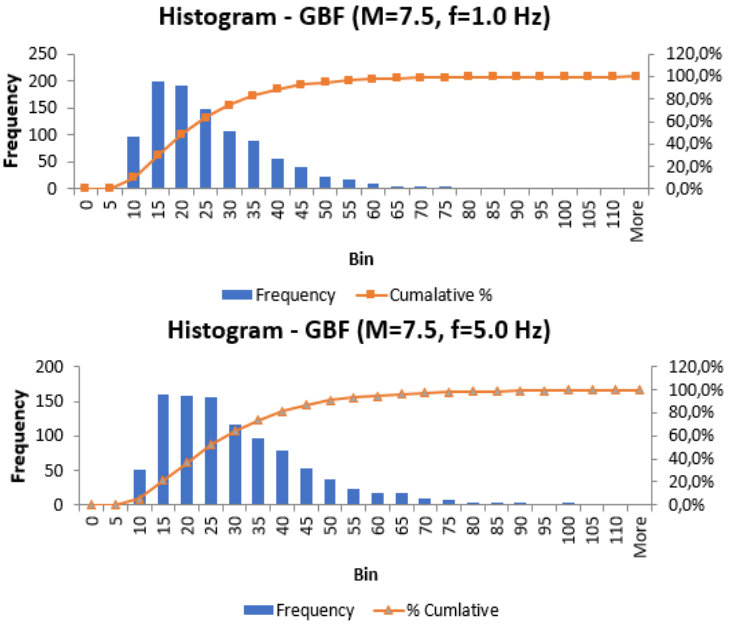

The model output was fitted to the LogNormal probability distribution, using the Probability Plot Method and the Maximum Likelihood Method (MLM) to estimate the parameters distribution and the 1st and 2nd moments of output. The principle of the method is that the parameters of the distribution function are fitted such that the probability (likelihood) of the observed random sample is maximised. The maximum likelihood point estimates of the parameters can be obtained by solving:

$$\min_{\theta}(-L(\boldsymbol{\theta}|\hat{\mathbf{x}})) \qquad L(\boldsymbol{\theta}|\hat{\mathbf{x}}) = \prod_{i=1}^{n} f_X(\hat{x}_i|\boldsymbol{\theta})$$

Instead of the likelihood function it is advantageous to consider the log-likelihood instead:

$$l(\boldsymbol{\theta}|\hat{\mathbf{x}}) = \sum_{i=1}^{n} \log(f_X(\hat{x}_i|\boldsymbol{\theta}))$$

Parameters Lognormal distribution fit

	HF (M=8.5)		GBF (M=7.5)	
	1Hz	5Hz	1Hz	5Hz
a	1,840	1,843	1,834	1,799
b	-7,514	-7,855	-5,543	-5,732
μ,Ln	4,084	4,261	3,022	3,186
σ,Ln	0,544	0,543	0,545	0,556
mean	68,870	82,156	23,826	28,233
Variance	1630,651	2310,021	196,549	288,581
Stdev	40,381	48,063	14,020	16,988

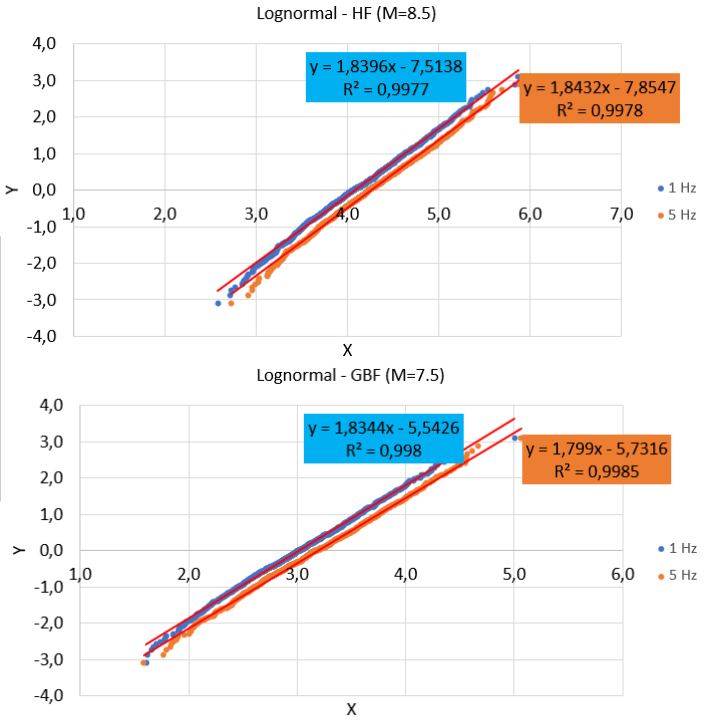

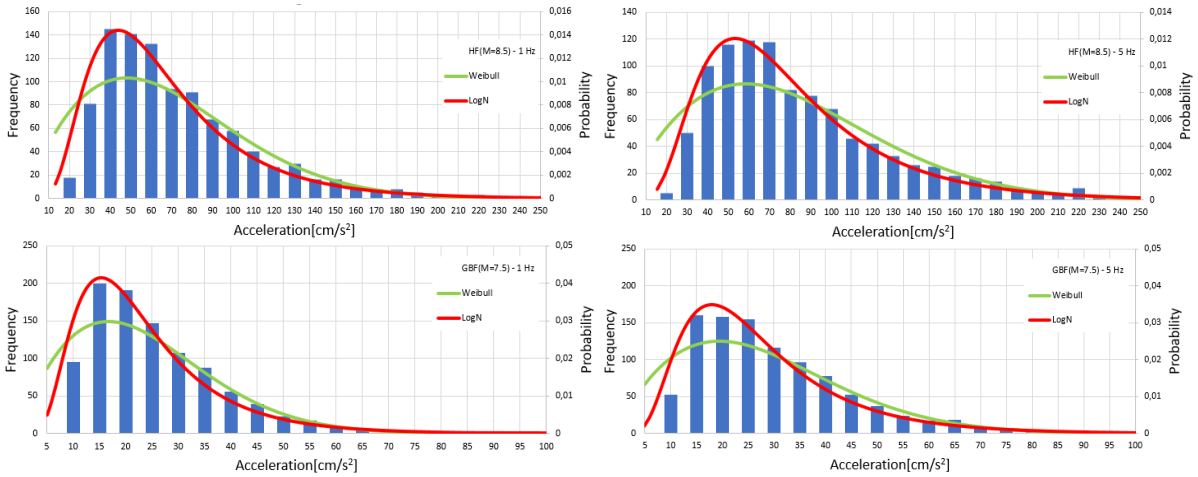

5.1.3.3 Global sensitivity analysis

Based on samples obtained from the Monte Carlo simulation a sensitivity analysis was performed using the linear first order regression (global sensitivity method). The standardised regression coefficient method (SRC) is implemented to evaluate the sensitivity of the random variables involved and to compare it with sensitivity analysis carried out before using FOSM and later using the Response Surface by multiple linear regression.

The first-order polynomial coefficients can be obtained by the least square estimate of the regression coefficients:

$$\hat{\beta} = (X'X)^{-1} X'y$$

where ***X*** is the matrix of sample values of the input variables and ***y*** the vector of observations (output).

The coefficients obtained for the first order regression are:

	HF (M=8.5)		GBF (M=7.5)	
	Frequency		Frequency	
	f= 1Hz	f= 5 Hz	f= 1Hz	f= 5 Hz
β0	150,049	194,725	66,441	81,828
β1	121,637	142,189	36,829	44,718
β2	-184,921	-1039,919	-123,851	-351,593
β3	-1,341	8,962	0,118	3,008
β4	-11,336	-17,270	-2,923	-5,089
β5	233,368	274,501	80,914	96,270
β6	51,051	57,610	21,616	23,168
β7	105,288	119,292	45,237	53,458

The sensitivity factors are given by: $\hat{\beta}_{X_i} = \hat{b}_{X_i} \frac{\sigma_{X_i}}{\sigma_Y} \left(i = 1, 2, \cdots, n\right)$

Horseshoe Fault (HS) – Magnitude 8.5

HF (M=8.5) - 1Hz

Variable	bi	σi	βi	βi^2	βi^2(normalized)	βi(normalized)	|βi|(normalized)	Rank
Stress Drop	121,637	0,2000	**0,604**	0,365	0,464	**0,681**	0,681	**2**
Kappa	-184,921	0,0072	**-0,033**	0,001	0,001	**-0,037**	0,037	**6**
F. length	-1,341	0,1442	**-0,005**	0,000	0,000	**-0,005**	0,005	**7**
F. width	-11,336	0,1442	**-0,041**	0,002	0,002	**-0,046**	0,046	**5**
b1	233,368	0,1079	**0,625**	0,391	0,498	**0,705**	0,705	**1**
b2	51,051	0,0568	**0,072**	0,005	0,007	**0,081**	0,081	**4**
b3	105,288	0,0568	**0,148**	0,022	0,028	**0,167**	0,167	**3**
			Sum	0,79	1,00			

HF (M=8.5) - 5Hz

Variable	bi	σi	βi	βi^2	βi^2(normalized)	βi(normalized)	|βi|(normalized)	Rank
Stress Drop	142,189	0,2000	**0,598**	0,358	0,448	**0,669**	0,669	**2**
Kappa	-1039,919	0,0072	**-0,158**	0,025	0,031	**-0,177**	0,177	**3**
F. length	8,962	0,1442	**0,027**	0,001	0,001	**0,030**	0,030	**7**
F. width	-17,270	0,1442	**-0,052**	0,003	0,003	**-0,059**	0,059	**6**
b1	274,501	0,1079	**0,623**	0,389	0,486	**0,697**	0,697	**1**
b2	57,610	0,0568	**0,069**	0,005	0,006	**0,077**	0,077	**5**
b3	119,292	0,0568	**0,143**	0,020	0,025	**0,159**	0,159	**4**
			Sum	0,80	1,00			

Gorringe Bank Fault (GBF) – Magnitude 7.5

GBF (M=7.5) - 1Hz

Variable	bi	σi	βi	βi^2	βi^2(normalized)	βi(normalized)	|βi|(normalized)	Rank
Stress Drop	36,829	0,2000	**0,530**	0,280	0,389	**0,623**	0,623	**2**
Kappa	-123,851	0,0072	**-0,064**	0,004	0,006	**-0,076**	0,076	**5**
F. length	0,118	0,1442	**0,001**	0,000	0,000	**0,001**	0,001	**7**
F. width	-2,923	0,1442	**-0,030**	0,001	0,001	**-0,036**	0,036	**6**
b1	80,914	0,1079	**0,628**	0,394	0,546	**0,739**	0,739	**1**
b2	21,616	0,0568	**0,088**	0,008	0,011	**0,104**	0,104	**4**
b3	45,237	0,0568	**0,185**	0,034	0,047	**0,217**	0,217	**3**
			Sum	0,72	1,00			

GBF (M=7.5) - 5Hz

Variable	bi	σi	βi	βi^2	βi^2(normalized)	βi(normalized)	|βi|(normalized)	Rank
Stress Drop	44,718	0,2000	**0,537**	0,288	0,388	**0,623**	0,623	**2**
Kappa	-351,593	0,0072	**-0,152**	0,023	0,031	**-0,177**	0,177	**4**
F. length	3,008	0,1442	**0,026**	0,001	0,001	**0,030**	0,030	**7**
F. width	-5,089	0,1442	**-0,044**	0,002	0,003	**-0,051**	0,051	**6**
b1	96,270	0,1079	**0,624**	0,389	0,524	**0,724**	0,724	**1**
b2	23,168	0,0568	**0,079**	0,006	0,008	**0,092**	0,092	**5**
b3	53,458	0,0568	**0,182**	0,033	0,045	**0,211**	0,211	**3**
			Sum	0,74	1,00			

Sensitivity factors by SRC:

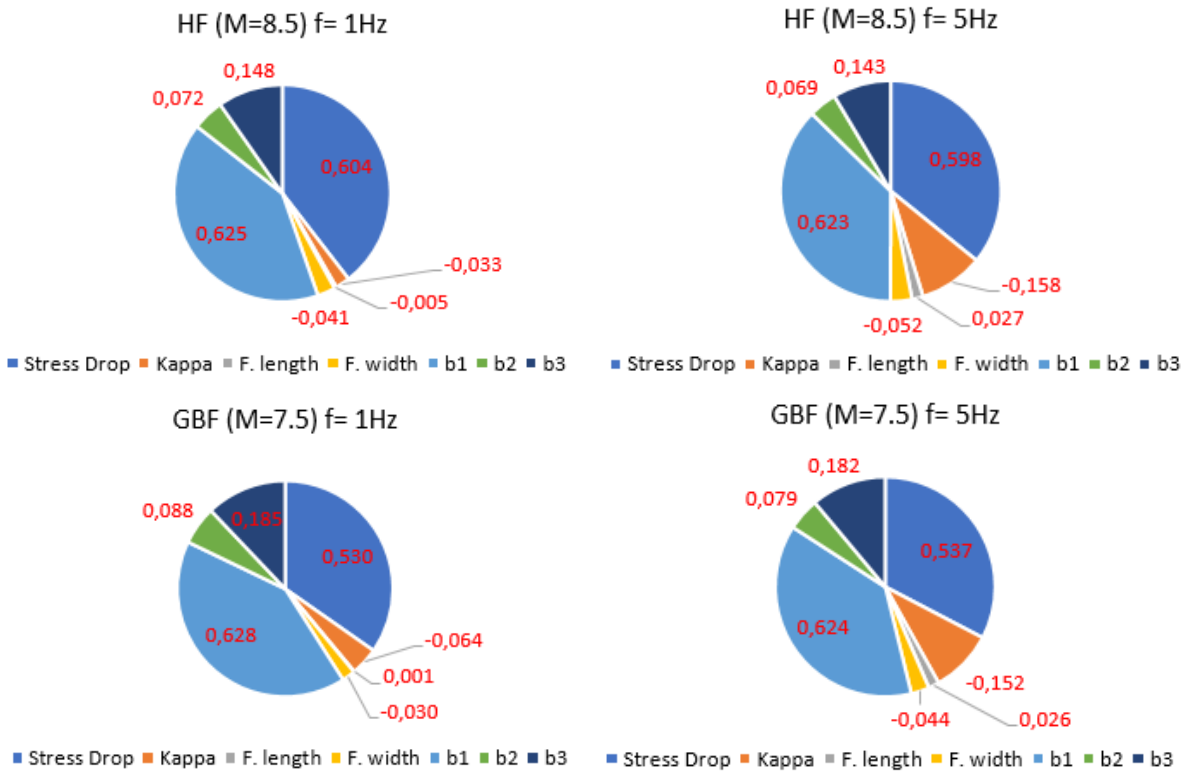

The sensitivity factors from FOSM(α_i) and by SRC(β_i) are compared for both scenarios:

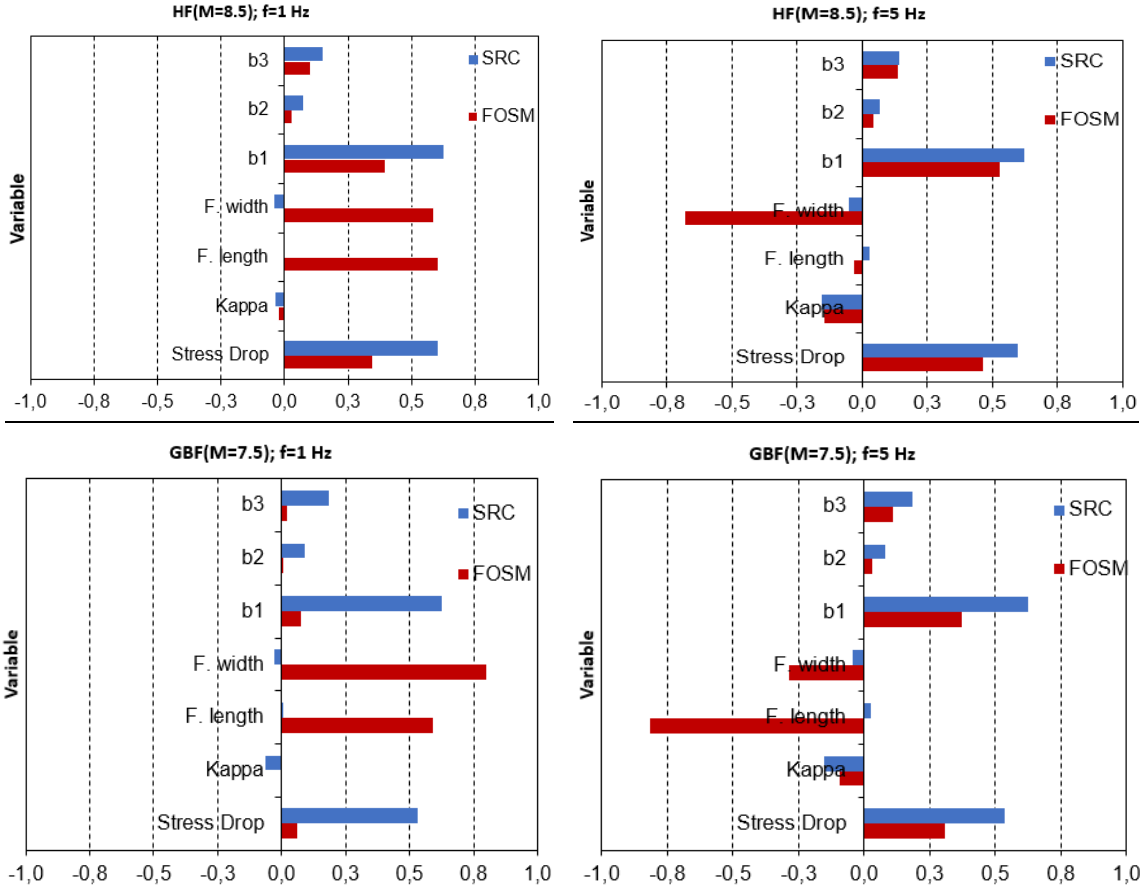

It can be seen that the outcomes from SRC tend to agree, in general, with the ones from FOSM on the importance of the variables, with the exception of the fault dimensions. It is recalled, however, that FOSM assumes that the variables have Gaussian distributions and is inherently a linear method, thus having difficulties in capturing the sensitivity of the variables in this case.

5.1.3.4 Response Surface method

Based on a model output of reduced size (100 samples), obtained through Monte Carlo simulation, a second order polynomial approximation with and without interaction terms was determined. The regression coefficients were computed and the adequacy of the regression model (surface response) was assessed by the coefficients of determination R^2 and R_{adj}^2.

The coefficients of determination obtained were:

	Without interaction				With interaction			
	HF (M=8.5)		GBF (M=7.5)		HF (M=8.5)		GBF (M=7.5)	
	Frequency		Frequency		Frequency		Frequency	
	f= 1Hz	f= 5 Hz	f= 1Hz	f= 5 Hz	f= 1Hz	f= 5 Hz	f= 1Hz	f= 5 Hz
SS_T	193820,69	257868,88	17664,21	27610,89	207403,79	273111,07	18762,41	29250,27
SS_E	22229,37	21936,15	2306,08	3558,84	8646,27	6693,96	1207,88	1919,46
R^2	**0,89**	**0,91**	**0,87**	**0,87**	**0,96**	**0,98**	**0,94**	**0,93**
R_{adj}^2	**0,75**	**0,81**	**0,72**	**0,72**	**0,87**	**0,93**	**0,81**	**0,80**
	n=100 and p=15				n=100 and p=36			

Based on these results it can be concluded that the response surface obtained for the second-order polynomial with interaction produces the best results. The sensitivity factors for this response surface are:

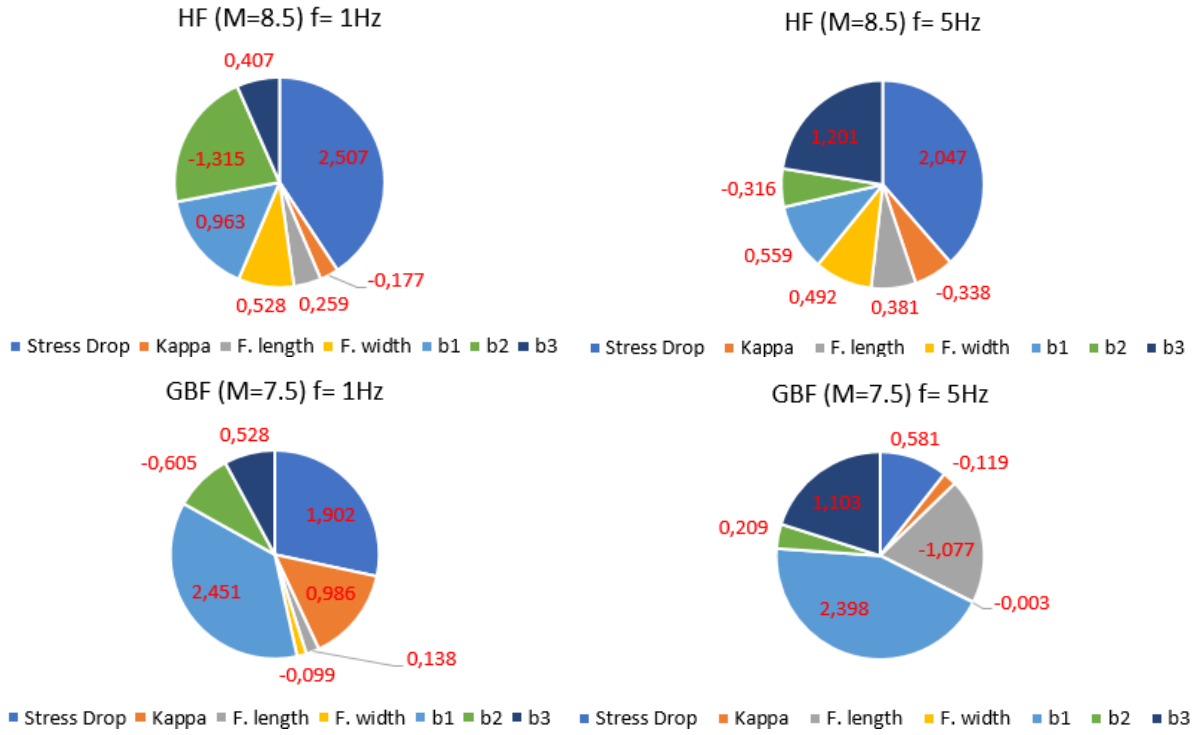

5.1.3.5 Discussion

For both scenarios, the Horseshoe Fault (HF) and the Gorringe Bank Fault (GBF), the mean value of spectral acceleration obtained by the First Order Second Moment method (FOSM) and by the Crude Monte Carlo simulation (MCS), with a 95% confidence interval, is, in general, similar. There are, however, larger discrepancies on what concerns the standard deviation and variance, given the limitations of FOSM. The coefficients of variation obtained through the MCS reveal a significant variability of the results, especially for HF at 1Hz.

The comparison of all the sensitivity analyses performed is presented in the bar chart below, where all values are normalized. As it can be seen, the propagation of uncertainty in this model is more affected, in general, by the stress drop and by the geometric spreading factor b_1. As mentioned above, the fault dimensions (for length and width) have a much higher sensivity in FOSM when compared to other methods, given the assumptions behind FOSM which render this method innacurate for nonlinear models and when the model parameter distributions are not Gaussian.

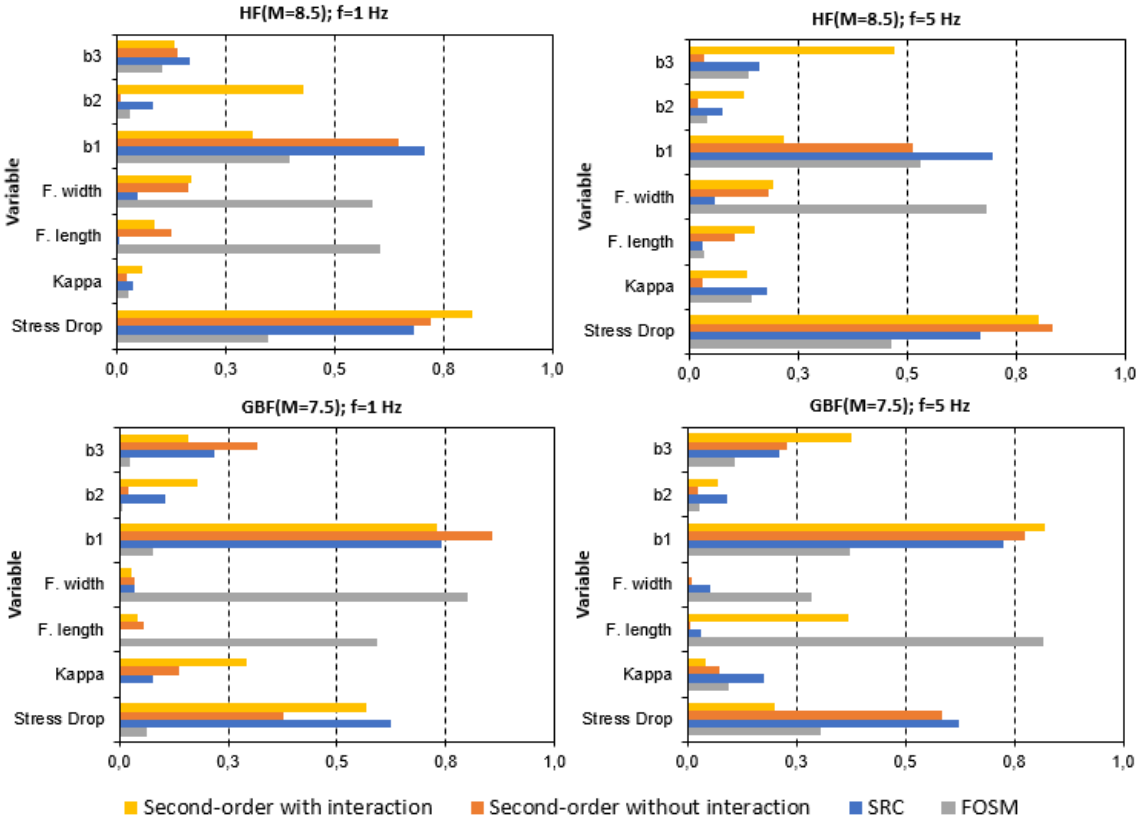

6 Summary, Conclusions and Future Developments

6.1 Summary

With regard to mixed control techniques for accuracy improvements, setups with stiff modes are typical when redundant actuators are used for practical reasons, such as improving the stability and test performance. However, classical displacement or force control based on the measurements at the level of the actuators is not adequate in these cases. The SLA4F4E shear setup at ELSA with two aligned actuators is an example with such characteristics. The control strategy successfully adopted for this SLA4F4E setup can be framed within an available general coordinate transformation methodology for the formulation of the control based on mixed modes.

Due to ever faster and more accurate testing equipment, dynamic substructure coupling has been developed in mechanical engineering for fast industry prototyping of components/substructures through a number of different offline experimental substructuring methods operating both in time, e.g. IBS, and frequency domains, e.g. LM-FBS. In this respect, an analysis of online/offline experimental substructuring methods has performed including the coupling algorithm of subdomains based on advanced parallel finite element tearing interconnecting (FETI) algorithms developed at JRC and UTRE. Moreover, a complex case study where all these methods were applied in a complementary way was presented.

As far as thermomechanical coupled analysis for hybrid dynamic simulations (HDS) is concerned, fires following earthquake can be ignited due to, for instance, failure of gas lines and of power lines. They can be a serious problem, especially if the water lines that feed the fire hydrants are broken too and the infrastructural network has undergone significant disruptions. Large-scale tests of an entire structure are generally prohibitively expensive, both in terms of finances and time, so generally it's convenient to adopt a HDS, that combines physical testing and computer modelling, offering a more efficient and affordable way to examine how large civil structures respond. Therefore, a MATLAB™ framework (D2LAB) for partitioned analyses and the RT-HFT-FETI algorithm is presented. Then, the effectiveness of the proposed method is demonstrated on a virtual experimental campaign. In detail, HFT of a realistic moment resisting frame subjected to fire is simulated numerically and validated against reference FE solutions.

With regard to reduction of epistemic uncertainties in HDS, an innovative procedure to perform fragility analyses on a realistic tank-piping system is presented. In detail, in order to cope with seismic ergodic uncertainty, a stochastic ground motion model is adopted to generate a large set of artificial accelerograms. This set is generated to be compatible with a probabilistic seismic hazard analysis of the geographical site of the tank-piping system. Furthermore, a simplified FE model is used to perform a global sensitivity analysis, based on polynomial chaos expansion and Sobol's indices, to reduce the space of the parameters of the stochastic ground motion model. Hence, from a large set of artificial seismic signals, a smaller set is selected to be experimentally tested as input for a hybrid simulator composed by a numerical substructure, i.e. a tank, and a physical substructure, i.e. a piping network. This procedure relies both on experimental data from HDS and a properly calibrated refined FE model to evaluate a numerical surrogate model able to predict the systems seismic response. Finally, the surrogate model is adopted to evaluate fragility curves for loss of containment in piping elbows part of the system.

An uncertainty propagation and sensitivity analysis study was performed on a stochastic finite-fault model for ground motion generation. Different methods were adopted and the differences between them pointed out.

6.2 Conclusions

With regard to mixed control techniques for accuracy improvements, a high-quality control strategy has been found for a testing setup for shear load of embedded plates using two actuators. The use of two aligned actuator offers the advantage of improving the stability if a pre-tension is maintained between both actuators. The control strategy has been equivalently formulated also by following the rational approach proposed by Plummer, which is based on coordinate transformation between control modes and actuator modes.

As far as an analysis of online/offline experimental substructuring methods is concerned, a comparison and the generalized use of online and offline methods for Experimental Dynamic Substructuring (EDS) has been carried out. With this perspective, a comprehensive uncertainty propagation analysis of experimentally-based online/offline dynamic substructuring methods was investigated. In particular, the performance comparison included the following methods: the online Hybrid (numerical/physical) Dynamic Substructuring (HDS) method and two offline methods, i.e. the Impulse-Based Substructuring method (IBS) and the Receptance-Based Substructuring (RBS) method. This investigation also explored the possibility of a combined exploitation of the three techniques, the novel composite (C-EDS) method, both to improve and accelerate the execution of the experiment/simulation. In this respect, we described the main characteristics of three EDS methods, which include the coupling algorithms based on dual assembly of Physical and Numerical Subdomains (PS and NS, respectively) performed with a localized version of the Lagrange multiplier method. Furthermore, capitalizing from the results of a more complex case study composed of a virtual petrochemical prototype plant, we provided a feasible approach to employ the C-EDS method along with a comprehensive verification. In particular, a linear PS -a piping- and a non-linear PS -four isolating devices- were coupled to a linear NS – a slender tank-. The comparison between substructuring and reference results, obtained from a monolithic model of the system, were satisfactory. Encouraged by these results presented in Section 2, the C-EDS method is currently being applied to an actual prototype plant in the laboratory.

With regard to thermomechanical coupled analysis for hybrid dynamic simulations (HDS) is concerned, the results presented in Section 3 testify the effectiveness of the proposed framework and RT-HFT. It was found that to obtain compatibility and equilibrium at the interface DoFs, the partitioned algorithm LLM-GC based on the FETI algorithm class was suitable to couple the PS with the NS The partition of the domains was conceived with the idea to be actually replicated in the laboratory by retaining the most significant DoFs at the interface between NS and PS.

The time-history response of the frame obtained via real time simulations showed good agreement between the monolithic and the partitioned solutions. The validation carried out in a fully numerical framework shows promising outcomes for future experimental implementations and it will be soon applied on a real experiment planned within the Transnational Access EQUFIRE within the European Unions Horizon 2020 SERA Project.

With regard to reduction of epistemic uncertainties in HDS, a stochastic ground motion model is calibrated according the seismic hazard of a specific site. Moreover, this model's parameters are evaluated by means of a global sensitivity analysis (GSA) upon the seismic response of realistic tank-piping system. As a result of the GSA, the seismic response is found to be truly dependent on only 3 of the 6 parameters of the stochastic ground motion model. Hence, after the reduction of parameters space, we generate a large set of artificial accelerograms. With this seismic input some hybrid simulations are carried out and a relevant FEM was tuned with a good level of accuracy. Furthermore, in the next step, both experimental data and FEM results will be used to evaluate a Kriging surrogate model. Finally, with a special focus on vulnerable piping elbows, a seismic fragility analysis of these components will be performed.

On what concerns the finite-fault stochastic ground motion model the main variables identified were the stress drop and the geometric spreading parameters.

6.3 Future developments

With regard to mixed control techniques for accuracy improvements, the existing control hardware currently at ELSA would allow for implementing full MIMO control strategies. However, the currently available software is originally defined as a system of SISO loops for the computation of the servo-valve commands. A partial application of coordinate transformation between control and actuator modes is possible with the currently available software by using the user-defined mixed feedback capability, even though this does not allow for a completely independent definition of the parameters of the control loop for every mode. A future version of ELSA's control software would be desirable. It should allow for a completely independent definition of the control loop for every control mode as defined in different coordinates from the actuator ones.

As far as an analysis of online/offline experimental substructuring methods is concerned, the C-EDS method is currently being applied to an actual prototype plant in the laboratory for Materials and Structures (LPMS) of the University of Trento.

The proposed framework and real time-hybrid fire testing (RT-HFT) method, will be soon applied on a real experiment within the access SERA Project: EQUFIRE. A concentrically braced frame (CBF) with pinned connections will be selected as a case study. The ground floor of the concentrically braced frame illustrated in Fig. E.1a will be substructured at the JRC-ELSA (Joint Research Centre - European Laboratory for Structural Assessment) and at the BAM (Bundesanstalt für Materialforschung und -prüfung) facilities. The remainder of the structure will be simulated numerically according to the FEM and it will be kept at ambient temperature through the test. The seismic damage will be mainly concentrated in bracing elements.

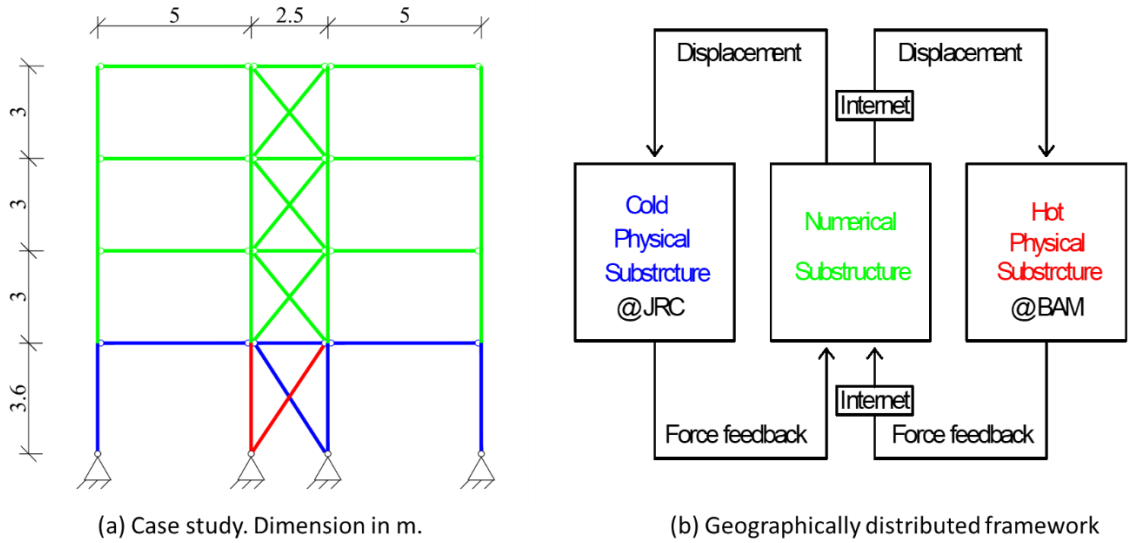

(a) Case study. Dimension in m.

(b) Geographically distributed framework

Figure E.1 case study and geographically distributed framework

Four geographically distributed fire following an earthquake hybrid tests will be carried out.

A partitioned time integration algorithm will solve the hybrid model response online. Inertia forces will be accounted for during the seismic response simulation whilst a static balance equation will be considered for the fire response simulation up to the collapse. All tests will be performed according to the distributed geographically framework shown in Fig. E.1b. The test setup (TEST #1 and TEST #2), which is intended to test the post-earthquake fire effects on a protected/unprotected column is depicted in Fig. E.2 and Fig. E.3. A set of horizontal actuators will serve to impose the cyclic lateral

loading, simulating the earthquake load. The vertical actuators at the position of column C1, C3 and C4 will impose the axial loading in the terms of displacement at the interface between the physical substructure and the numerical substructure. During the hybrid seismic test, also C2 will be seismically loaded in the furnace at BAM by means of geographically distributed technique. Then, once the seismic test is finished the furnace will be turned on to start the fire test. Similarly, the setup for TEST #3 and TEST #4 is shown in Fig. E.4 and Figure Fig. E.5 with the bracing element substructured at BAM.

Particular attention will be given to the box fire protection systems because they are likely to be damaged due to an earthquake.

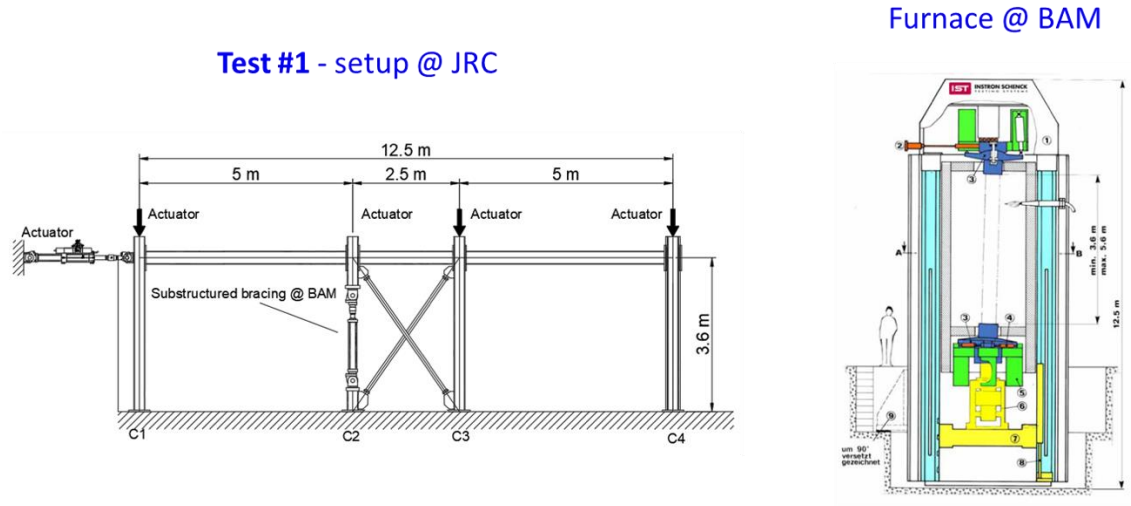

Figure E.2 TEST #1: test on post-earthquake fire effects on an unprotected column.

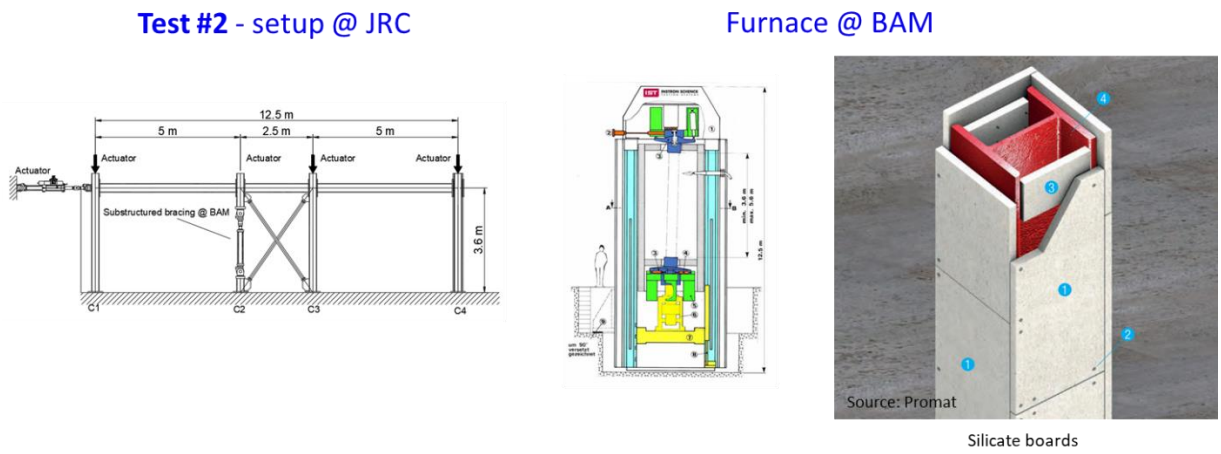

Figure E.3 TEST #2: test on post-earthquake fire effects on a protected column.

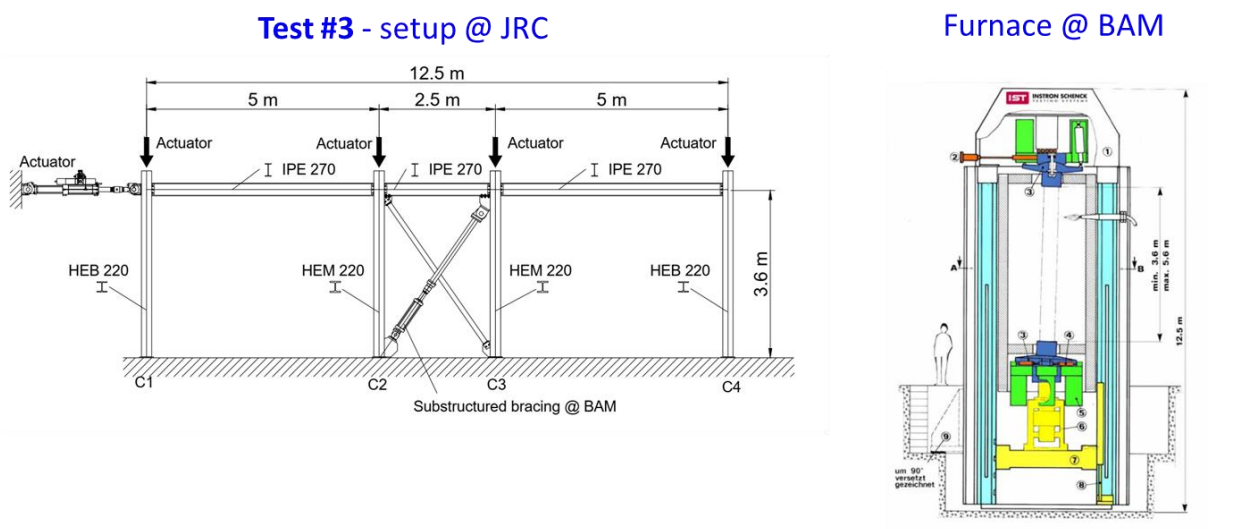

Figure E.4 TEST #3: test on post-earthquake fire effects on an unprotected bracing element.

Non-structural components will also be tested, including box passive fire protections and fire barrier walls. The fire barrier wall will be made of concrete bricks with assigned fire ratings, e.g. EI60 designated for an office building.

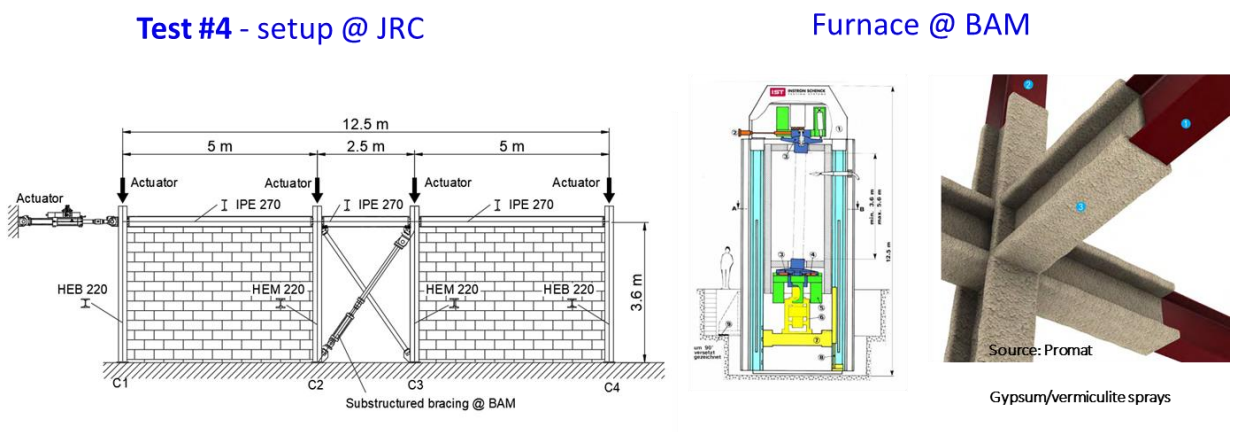

Figure E.4 TEST #4: test on post-earthquake fire effects on a protected bracing element.

With regard to reduction of epistemic uncertainties in HDS, the actual evaluation of the surrogate model presented in Section 4 will be achieved in the next steps of this research project. However, the proposed model is going to be tested against a classic fragility assessment approach in future activities and different geographical locations will be taken into account. Finally, the possibility of an extension of the stochastic ground motion model discussed in Subsection 4.1.1 is going to be explored.

7 References

[1] Bosi, A., Magonette, G. and Pegon, P. (2012), Advancement In Servo-Hydraulic Modelling At ELSA For Pseudo-Dynamic Testing, EACS 2012 – 5th European Conference on Structural Control Genoa, Paper No. 166.

[2] Bousias, S.N., (2014) "Seismic Hybrid Simulation of Stiff Structures: Overview and Current Advances," Journal of Structures, Article ID 825692, 8 pages. doi:10.1155/2014/825692

[3] Molina Ruiz, F. J. (2016), Pegon, P., Peroni, M., Viaccoz, V., Mixed variable control for enhanced testing quality. Formulation of the model. JRC Scientific and Technical Reports, JRC105052. Publications Office of the European Union.

[4] Plummer, A. R., (2010) A general co-ordinate transformation framework for multi-axis motion control with applications in the testing industry. Control Engineering Practice, 18, 598–607.

[5] Plummer, A. R., (2013), Practical multivariable control for multiaxis hydraulic servosystems. International Conference on Fluid Power Transmission and Control, Hangzhou.

[6] SERIES project, Deliverable D12.2 (2012), Report on evaluation of novel actuation systems for shaking table, pseudo-dynamic or field testing.

[7] SERIES project, Deliverable D12.3 (2013), Prototype Design Study.

[8] Abbiati G., La Salandra V., Bursi O.S, Caracoglia L., "A Composite Experimental Dynamic Substructuring Method Based on Partitioned Algorithms and Localized Lagrange Multipliers"

[9] D. de Klerk, D. Rixen, S. Voormeeren, General framework for dynamic substructuring: history, review and classification of techniques, AIAA Journal 46 (5), 1169–1181, 2008.

[10] O.S. Bursi and D. J. Wagg, Eds. - Modern Testing Techniques for Structural Systems Dynamics and Control , CISM-Springer Wien NewYork 2008

[11] Bursi, O.S., Abbiati, G., Cazzador, E., Pegon, P., Molina, F.J. "Nonlinear heterogeneous dynamic substructuring and partitioned FETI time integration for the development of low-discrepancy simulation models", Int. J. for Numerical Methods in Eng., 2017, DOI: 10.1002/nme.5556.

[12] Bursi, O.S., Abbiati, G., Reza M.S., A Novel Hybrid Testing Approach for Piping Systems of Industrial Plants. Smart Structures and Systems", Vol. 14, N. 6, 1-26, 2014.

[13] D.J. Rixen, P.L.C. Van Der Valk, An Impulse Based Substructuring Approach for Impact Analysis and Load Case Simulations, Journal of Sound and Vibration 332 (26), 2013, 7174-7190.

[14] P.L.C. Van der Valk, D.J. Rixen, An Impulse Based Substructuring Method for Coupling Impulse Response Functions and Finite Element Models, Computer Methods in Applied Mechanics and Engineering 275, 2014, 113-137.

[15] S.N. Voormeeren, D. de Klerk, D.J. Rixen, Uncertainty Quantification in Experimental Frequency Based Substructuring, Mechanical Systems and Signal Processing 24 (1), 2010, 106-118.

[16] A. Gravouil, A. Combescure . Multi-time-step explicit – implicit method for non-linear structural dynamics, International Journal for Numerical Methods in Engineering, 2001, pp 199–225.

[17] K.C. Park, C. A. Felippa, U. A. Gumaste, A localized version of the method of Lagrange multipliers and its application, Computational Mechanics 24, 2000, 476-490.

[18] NM. Newmark, A method of computation for structural dynamics. Journal of Engineering Mechanics, ASCE, 1959, 85, pp 67–94.

[19] M. Wallace, Stability analysis of real-time dynamic substructuring using delay differential equation models, Earthquake Engineering & Structural Dynamics, Volume 34, Issue 15, December 2005, 1817-1832

[20] C.P. Lamarche, A. Bonelli, OS Bursi, A Rosenbrock-W method for real-time dynamic substructuring and pseudo-dynamic testing, Earthquake Engineering & Structural Dynamics, 2009, 38 (9), 1071-1092.

[21] Bernal, D. (1994). Viscous Damping in Inelastic Structural Response. Journal of Structural Engineering, 120(4), 1240–1254.

[22] Molina, F. J., Magonette, G., Pegon, P., & Zapico, B. (2011). Monitoring Damping in Pseudo-Dynamic Tests. Journal of Earthquake Engineering, 15(6), 877–900.

[23] Voormeeren, S. N., & Rixen, D. J., A family of substructure decoupling techniques based on a dual assembly approach. Mechanical Systems and Signal Processing, 2012, 27, 379–396.

[24] D'Ambrogio, W., & Fregolent, A., Direct hybrid formulation for substructure decoupling. In Topics in Experimental Dynamics Substructuring and Wind Turbine Dynamics, Volume 2, 2012 (pp. 89-107). Springer New York.

[25] Lomiento, G., Bonessio, N., & Benzoni, G. (2013). Friction Model for Sliding Bearings under Seismic Excitation. Journal of Earthquake Engineering, 17(8), 1162–1191. http://doi.org/10.1080/13632469.2013.814611

[26] R. J. Guyan, Reduction of Stiffness and Mass Matrices, AIAA Journal, Vol. 3, February, 1965.

[27] Mostaghel, N. (1999). "Analytical description of pinching, degrading hysteretic systems." J. Eng. Mech., 125(2), 216,224

[28] P. K. Malhotra, T. Wenk, M. Wieland, Simple Procedure for Seismic Analysis of Liquid-Storage Tanks, Structural Engineering International 3/2000.

[29] MATLAB and Statistics Toolbox Release 2012b, The MathWorks, Inc., Natick, Massachusetts, United States.

[30] Abbiati G, Marelli S., Bursi O.S., Sudret B., Stojadinovic B., 2015 Uncertainty propagation and global sensitivity analysis in hybrid simulation using polynomial chaos expansion. The 15th International Conference on Civil, Structural and Environmental Engineering Computing CIVIL-SOFT-COMP (CSC2015) Prague, Czech Republic 1-4 September (2015), ISSN: 17593433, 2-s2.0-84966359045.

[31] Abbiati G., Abdallah I., Marelli S., Sudret B. and Stojadinovic B., Hierarchical Kriging Surrogate of the Seismic Response of a Steel Piping Network Based on Multi-Fidelity Hybrid and Computational Simulators, Proceedings of the 7th International Conference on Advances in Experimental Structural Engineering (7AESE), September 6-8, EUCENTRE, Pavia, Italy (2018).

[32] ANSYS Mechanical Software by ANSYS, Inc. 2015, Southpointe 2600 ANSYS Drive Canonsburg, PA 15317 USA

[33] Baker J.W. (2008). "An Introduction to Probabilistic Seismic Hazard Analysis (PSHA)", Version 1.3.

[34] Baker JW, 2015. Efficient Analytical Fragility Function Fitting Using Dynamic Structural Analysis. Earthquake Spectra. Vol. 31, No. 1, pp. 579-599.

[35] Cornell, C. A. (1968). "Engineering seismic risk analysis." Bulletin of the Seismological Society of America, 58(5), 1583-1606

[36] Malhotra P.K., Wenk T., Wieland M., "Simple Procedure for Seismic Analysis of Liquid-Storage Tanks", Structurale Engineering International 3/2000, 197-201.

[37] Marelli, S. & Sudret, B. UQLab: A Framework for Uncertainty Quantification in Matlab 257 Vulnerability, Uncertainty, and Risk (Proc. 2nd Int. Conf. on Vulnerability, Risk Analysis and Management (ICVRAM2014), Liverpool, United Kingdom), 2014, 2554-2563.

[38] Mostaghel, N. (1999). "Analytical description of pinching, degrading hysteretic systems." J. Eng. Mech., 125(2), 216,224.

[39] Oreste S. Bursi, Rocco di Filippo, Vincenzo La Salandra, Massimiliano Pedot, Md S. Reza, 2018, Probabilistic seismic analysis of an LNG subplant. Pages 45-60, Risk Analysis in Process Industries: State-of-the-art and the Future, Edited by Genserik Reniers, Ankur Pariyani, Volume 53, Pages 1-148 (May 2018)

[40] Pedot M., di Filippo R., Bursi O.S., A Seismic Vulnerability Analysis of a Liquefied Natural Gas Subplant, (2018), Proceedings of the ASME 2018 Pressure Vessels and Piping Conference, PVP2018, July 15-20, 2018, Prague, Czech Republic

[41] Rezaeian S., Der Kiureghian A. (2010). Simulation of synthetic ground motions for specified earthquake and site characteristics, Earthquake Engng Struct. Dyn. 2010; 39:1155–1180

[42] Sobol' IM. Sensitivity estimates for nonlinear mathematical models. Math Modeling Comput Exp;1:407–14. 1993.

[43] Abbiati G., Covi P., Tondini N., Bursi O.S., Stojadinovic B. (2019). "A Real-Time Hybrid Fire Testing Method Based on Dynamic Relaxation and Component-Mode Synthesis", Computers and Structures, 2019, in preparation.

[44] Park K. C., Felippa C. A., Gumaste U. A. (2000). A localized version of the method of Lagrange multipliers and its applications, Computational Mechanics 24 (6) (2000) 476-490

[45] Underwood P. G. (1983). Computational Methods for Transient Analysis, North-Holland, Amsterdam, 1983, Ch. Dynamic relaxation techniques: a review.

[46] European Union (2005). Eurocode 3: Design of steel structures - Part 1-2: General rules - Structural fire design, European standard, European Union (May 2005).

[47] Franssen. J-M. (2005). SAFIR: A thermal/structural program for modeling structures under fire, Engineering Journal (New York) 42 (3) (2005) 143-150.

[48] ABAQUS, ABAQUS Inc., Dassault Systemes, France.

[49] Boissonnade, N. (2006). Rules for member stability in EN 1993-1-1 : background documentation and design guidelines, Brussels, ECCS.

[50] Carvalho, A. (2007). Stochastic modelling of the seismic action in Portugal (in Portuguese). PhD Thesis, Instituto Superior Técnico (IST), Lisbon, Portugal.

[51] Atkinson, G. (2004). Empirical attenuation of ground-motion spectra amplitudes in southeastern Canada and the northeastern United States. Bull. Seism. Soc. Am. 94, 1079-1095.

[52] Atkinson, G. and Boore, D. (1995). New ground motion relations for eastern North America. Bull. Seism. Soc. Am. 85, 17–30.

[53] Atkinson, G. and Boore, D. (2006). Earthquake ground-motion prediction equations for Eastern North America. Bull. Seism. Soc. Am. 96:6, 2181-2205.

[54] Carvalho, A., Campos Costa, A. and Oliveira, C.S. (2009). A finite-fault modeling of the 1755 Lisbon earthquake sources. The 1755 Lisbon earthquake: revisited, series GGEE 7, Springer. pp 433-454.

[55] Morbioli, A., Tondini, N., Battini J.-M. (2018). A branch-switching procedure for analysing instability of steel structures subjected to fire, Structural Engineering and Mechanics 67 (6) (2018) 629–641.

[56] Battini J.M. (2002). Co-rotational beam elements in instability problems, PhD thesis (2002), Department of Structural Engineering KTH, Stockholm, Sweden

[57] Craig R. R., Kurdila A. J. (2006). Fundamentals of structural dynamics, John Wiley & Sons, 2006